ELLIPSOMETRIC STUDY OF SIMPLE AND COMPLEX OXIDES FROM THE MID INFRARED TO THE NEAR ULTRAVIOLET

BY

TIMOTHY NATHANIEL NUNLEY, B.S.

A dissertation submitted to the Graduate School

in partial fulfillment of the requirements

for the degree

Master of Science

Major Subject: Physics

New Mexico State University

Las Cruces New Mexico

August 2016

"Ellipsometric Study of Simple and Complex Oxides from the Mid Infrared to the Near Ultraviolet," a thesis prepared by Timothy Nathaniel Nunley in partial fulfillment of the requirements for the degree, Master of Science, has been approved and accepted by the following:

Loui Reyes
Associate Dean of the Graduate School

Stefan Zollner
Chair of the Examining Committee

Date

Committee in charge:

Dr. Stefan Zollner, Chair

Dr. Jacob Urquidi

Dr. Michael Engelhardt

Dr. William Quintana

DEDICATION

I would like to dedicate this thesis to my lovely wife, Lindsay, who has supported and encouraged me in my work.

ACKNOWLEDGMENTS

First, I would like to thank all of my family for everything they have done for Lindsay and I and always being there to cheer us on.

I would like to give special thanks my advisor, Stefan Zollner, for all the guidance I have received, scientific and otherwise over the course of the last several years. I would also like to thank everyone that is currently or was in my research group for their help and being a joy to work with, especially Nalin Fernando, Travis Willett-Gies, Lina Abdallah, Nuwanjula Samarasingha, Dennis Trujillo, Laura Pineda, Jaime Moya, Jackie Cooke, Cayla Nelson, and Amber Medina. I would also like to thank our collaborators for their part in my research, Felicia Manciu from UTEP, and Premysl Marsik and Christian Bernhard from the University of Fribourg.

I would also like to give a special thanks to all of the staff and faculty in the physics department for being so much help in my growth as a professional and a scientist.

And of course I would like to thank all of the agencies that funded our work, with out whom ths would not be possible. This work was supported by the Air Force Office of Scientific Research (FA9550-13-1-0022), the Army Research Office (W911NF-14-1-0072), the National Science Foundation (DMR-1104934 and DMR-1505172). The infrared ellipsometry measurements were carried out at the Center

for Integrated Nanotechnologies, an Office of Science User Facility operated for the U.S. Department of Energy (DOE) Office of Science by Los Alamos National Laboratory (Contract DE-AC52-06NA25396) and Sandia National Laboratories (Contract DE-AC04-94AL85000). The work at the University of Fribourg was supported by the Schweizerische Nationalfonds (SNF) through grant No. 200020-153660.

VITA

June 25, 1993	Born at Las Cruces, New Mexico, United States of America
2011-2015	B.S., New Mexico State University
2013-2014	Chemistry Supplemental Instruction Facilitator
2014-2015	Arts and Sciences Peer Learning Assistant
2012-2015	Undergraduate Research Assistant
2015-2016	M.S., New Mexico State University
2015-2016	Graduate Teaching Assistant
2015-2016	Graduate Research Assistant

PROFESSIONAL AND HONORARY SOCIETIES

American Physical Society

American Association of Physics Teachers

Sigma Pi Sigma

PUBLICATIONS

T. N. Nunley, T. I. Willett-Gies, J. A. Cooke, F. S. Manciu, P. Marsik, C. Bernhard, S. Zollner *In Review, Journal of Vacuum Science and Technology A* (2016)

T. N. Nunley, N. S. Fernando, N. Samarasingha, J. M. Moya, C. M. Nelson, A. A. Medina, S. Zollner *In Review, Journal of Vacuum Science and Technology B* (2016)

S. Zollner, T. N. Nunley, D. P. Trujillo, L. G. Pineda, L. S. Abdallah *In Review, Applied Surface Science* (2016)

A. O'Hara, T.N. Nunley, A.B. Posadas, S. Zollner, and A.A. Demkov, J. Appl. Phys. **116**, 213705 (2014).

PRESENTATIONS AND POSTERS

J.M. Moya, T.N. Nunley, D.P. Adams, and S. Zollner, Optical properties of Ni and Ni:V alloys, AVS 2016 New Mexico Symposium, Albuquerque, NM, May 24th, 2016

J. Cooke, T.N. Nunley, T. Willett-Gies, and S. Zollner, Infrared and visible dielectric properties of $(LaAlO_3)_{0.3}(Sr_2AlTaO_6)_{0.35}$, AVS 2016 New Mexico Symposium, Albuquerque, NM, May 24th, 2016 (Poster)

T.N. Nunley, N. Fernando, J. Moya, and S. Zollner, Optical constants of Ge and GeO_2 from ellipsometry, 80. Jahrestagung der DPG und DPG-Fruhjahrstagung, 6-11 March 2016, Regensburg, Germany

N. Fernando, and T.N. Nunley, S. Zollner, D. Zhang, R. Hickey, J. Kolodzey, AVS 62nd, Band Structure and Critical Points of Pseudomorphic $Ge_{1y}Sn_y$ Alloys on Ge, The International Symposium and Exhibition, San Jose, CA, 19 October 2015

T. N. Nunley, N. Fernando, J. Moya, and S. Zollner, Growth and Properties of Ge Thermal Oxides, APS Four Corners Section Meeting 2015

T. N. Nunley, S. Zollner, A. B. Posadas, A. O'Hara, and A. A. Demkov, Ellipsometric Study of NbO_2 Grown by MBE on LSAT from 77 to 800 K, APS March Meeting 2015

N. Fernando, and T. Nunley, S. Zollner, D. Zhang, R. Hickey, J. Kolodzey, Compositional and strain dependence of the band gaps of pseudomorphic $Ge_{1-y}Sn_y$ alloys on Ge, AVS 2015 New Mexico Symposium, Albuquerque, NM, May 19th, 2015

N. Fernando, T.N. Nunley, S. Zollner, S. Xu, J. Menendez, and J. Kouvetakis, Temperature Dependent band gaps of GeSiSn alloys grown on Ge buffered Si substrates, The American Physical Society March meeting, San Antonio, TX, March 2-6, 2015

M. Sholte, C. Lin, K. Kormondy, T.N. Nunley, A. Posadas, S. Zollner, A.A. Demkov, Investigation of the Band Gap in Co_3O_4, The American Physical Society March meeting, San Antonio, TX, March 2-6, 2015

T. N. Nunley, S. Zollner, A. B. Posadas, A. O'Hara, and A. A. Demkov, Op-

tical Constants of NbO_2 on LSAT grown by MBE from 0.2 to 6.5 eV, Rio Grande Symposium on Advanced Materials 2014 (Poster)

T. N. Nunley, T. Willet-Gies, and S. Zollner, The Infrared and Visible Dielectric Properties of $(LaAlO_3)_{0.3}$ $(Sr_2AlTaO_6)_{0.35}$, APS Four Corners Section Meeting 2013 (Poster)

T. N. Nunley, T. Willet-Gies, and S. Zollner, The Infrared and Visible Dielectric Properties of $LaAlO_3)_{0.3}$ $(Sr_2AlTaO_6)_{0.35}$, Rio Grande Symposium on Advanced Materials 2013 (Poster)

FIELD OF STUDY

Major Field: Physics

ABSTRACT

ELLIPSOMETRIC STUDY OF SIMPLE AND COMPLEX OXIDES FROM
THE MID INFRARED TO THE NEAR ULTRAVIOLET

BY

TIMOTHY NATHANIEL NUNLEY, B.S.

Master of Science

New Mexico State University

Las Cruces, New Mexico, 2016

Dr. Stefan Zollner, Chair

The work presented in this thesis describes three different material systems: the perovskite complex oxide, LSAT, the classic semiconductor system, thermal oxide on Ge, and the ferromagnetic metal, Ni. Although several measurement techniques were used, the main purpose of these studies was to obtain the optical constants through the use of spectroscopic ellipsometry.

$LaAlO_3)_{0.3}$ $(Sr_2AlTaO_6)_{0.35}$, or LSAT, is a cubic perovskite insulator. It has been designed to be a very stable substrate material for other oxides and novel materials. Spectroscopic ellipsometry was used from 0.5 to 6.5 eV to study the electronic properties of the material. The material is transparent in the visible range and begins to absorb light at 4.8 eV in the form of an Urbach tail. The lowest direct band gap was determined to be 5.8 eV and higher energy electronic transitions were outside of our spectral range. Using FTIR ellipsometry, we analyzed the phonon dispersion. We used a Lyddane-Sachs-Teller dispersion model with nine terms giving the energies, broadenings, and amplitudes of the phonon pairs. The phonons were also assigned to modes of the lattice vibrations.

Thermal Ge oxide films were also created and then analyzed using ellipsometry. Through the use of multi-sample analysis we were able to decouple the oxide and substrate optical constants. This allows us to improve the precision of the optical constants of bulk Ge, especially at the E_2 transition. This is important for the metrology of Ge based devices because interest is growing in them again because of certain intrinsic properties of Ge such as high hole mobility.

Finally, the dielectric function of magnetized Ni was studied at 1.96 eV (632.6 nm) as a function of temperature from 80 to 760 K. We saw that there was a transition at the Curie temperature in the complex dielectric function while heating. After the sample is demagnetized, this anomaly is not seen again when cooling below the Curie temperature and is repeatable upon remagnetizaton. It

was determined that this is not attributable to the magneto-optical Kerr effect due to the magnitude of the transition in dielectric function, but to the on-diagonal elements of the dielectric tensor.

CONTENTS

LIST OF TABLES **xvii**

LIST OF FIGURES **xxiii**

1 INTRODUCTION **1**

2 GENERAL THEORY AND METHOD **4**

2.1 Electronic Band Structure 4

2.2 Phonons 8

2.3 Diffusion and Oxidation 9

2.4 Spectroscopic Ellipsometry 14

2.4.1 Theory 15

2.4.2 Instrumentation 21

2.4.3 Data Analysis 27

2.5 X-Ray Reflectance 28

3 OPTICAL CONSTANTS, BAND GAP, AND INFRARED-ACTIVE PHONONS OF $(LaAlO_3)_{0.3}(Sr_2AlTaO_6)_{0.35}$ (LSAT) FROM SPECTROSCOPIC ELLIPSOMETRY **29**

3.1 Introduction 30

3.2 Experiment and Models 32

3.3 Results from near-IR to UV at 300 K 36

3.4 Far-IR, Mid-IR, and Raman Results 45

3.5 Summary 54

4 OPTICAL CONSTANTS OF GERMANIUM AND THERMALLY GROWN GERMANIUM DIOXIDE FROM 0.5 TO 6.6 eV VIA A MULTI-SAMPLE ELLIPSOMETRY INVESTIGATION 56

4.1 Introduction 57

4.2 Thermal oxidation of Ge 61

4.3 Ellipsometry measurements and data analysis 65

4.4 Results for uniform GeO_2 on Ge 73

4.5 Results for GeO_2 on Ge with non-uniform layer fits 81

4.6 Discussion 83

4.7 Summary 86

5 TEMPERATURE-DEPENDENT DIELECTRIC FUNCTION OF NICKEL 90

5.1 Introduction 91

5.2 Experiment 92

5.3 Results 97

5.4 Discussion 100

5.5 Summary and Outlook 104

6 OUTLOOK AND SUMMARY **106**

REFERENCES **108**

LIST OF TABLES

1 Tauc-Lorentz (TL) parameters energy E, broadening Γ, amplitude A, and Tauc gap E_g for describing the dielectric function of LSAT at 300 K from 0.8 to 6.5 eV with one or two TL oscillators, obtained by fitting the parameters to the data in Fig. 10. The IR and UV pole energies and amplitudes are also listed. Probable errors are given in parentheses. (f) indicates that the parameter was fixed. . 41

2 Parameters for TO and LO phonons from FTIR ellipsometry: Energy E, amplitude A, and broadening Γ. The top portion shows the parameters for nine Lorentz oscillators. The bottom portion describes ϵ with a product of nine LST factors for TO/LO phonon pairs. The LST amplitudes were calculated from Eq. (19). 53

3 List of GeO_2 oxides produced by thermal oxidation of Ge substrates at 2.7 atm oxygen pressure at 550°C. d is the oxide thickness from ellipsometry, t the oxidation time, Δd the relative thickness non-uniformity determined from the ellipsometry depolarization spectra, d_{XRR} the thickness as determined by x-ray reflectance (XRR) (samples 4 and 5 were fit with a fixed thickness), and $<\rho>_{\mathrm{XRR}}$ the electron density determined by XRR. 66

4 Deal-Grove parameters A, B, and τ from Eq. (20) for thermal oxidation of Ge in pure O_2 at temperature T and pressure p. 66

LIST OF FIGURES

1 Calculation of the band structure of Ge at 0 K, taken from figure 4 of reference [1] 6

2 Figure 3 from reference [68] depicting the boundaries taken while solving the diffusion equation and the respective solutions of the flux for each stage of the model. 12

3 A geometric depiction of the physical meaning of the ellipsometric angles. 16

4 A cartoon of our rotating analyzer V-VASE. 23

5 A picture of our rotating analyzer V-VASE. Present in the photo (from left to right) is the end of the fiber-optics cable; the housing for the focusing lens, polarizer, and Autoretarder; the sample stage; and the housing for the analyzer and detector. The two goniometers used for rotating the sample stage and detector arm are also seen below the sample stage. 24

6 A picture of our monochromator, controller, and sample stage vacuum (left to right). 25

7 A picture of a Woollam IR-VASE instrument. 27

8 (a) Symmetric $2\theta/\omega$ x-ray diffraction scan for an LSAT wafer with (100) orientation. Miller indices are indicated in the simple cubic perovskite notation. (b) Rocking curve for the (200) Bragg reflection with a FWHM of 0.05°. (c) ϕ-scan of the (115) Bragg reflection of the ordered FCC LSAT structure. 34

9 Transmission (dashed) and absorption coefficient (solid) for a two-side polished LSAT wafer with 0.5 mm thickness obtained at 300 K from a normal-incidence transmission measurement. 37

10 Ellipsometric angles ψ and Δ versus photon energy for incidence angles from 60° to 80° (symbols) for LSAT at 300 K. The lines show a fit with two poles and two Tauc-Lorentz oscillators, assuming a surface roughness of 19.1 Å. 39

11 Same data as in Fig. 10, but displayed as a pseudo-dielectric function. 40

12 Real and imaginary part of the dielectric function ϵ of LSAT at 300 K described with two Tauc-Lorentz oscillators and two poles (solid), calculated using the parameters in Table 1. Data calculated from the Sellmeier parameters listed in Ref. [14] (dashed) and Ref. [28] (dot-dashed) are shown for comparison. 43

13 The square of the absorption coefficient of LSAT versus photon energy at 300 K can be extrapolated to yield a direct band gap of 5.8±0.1 eV, as shown by the dashed line. Symbols were determined by direct inversion of the ellipsometric angles (wavelength-by-wavelength fit), while the solid line shows the result of the Tauc-Lorentz model. The inset shows α on a logarithmic scale. 44

14 Raman spectra for LSAT (100) at 300 K show four strong peaks, similar to Sr_2AlTaO_6. Symmetry assignments for the vibrations were taken from the literature.[23, 37] 46

15 Ellipsometric angles ψ and Δ for LSAT at 300 K in the region of lattice absorption (symbols) for three angles of incidence (65° to 75°) in comparison with a fit to a factorized model with nine TO/LO phonon pairs (solid). 47

16 Same data as in Fig. 15, but shown as a pseudodielectric function. 48

17 Same data as in Fig. 15, but shown as a pseudo-loss function $-1/\langle\epsilon\rangle$. 49

18 Thermal oxide thickness versus oxidation time at atmospheric pressure (Ref. [70]) and at 2.7 atm (this work). The solid line shows the best fit to Eq. (20), while the dashed lines assume a quadratic dependence of the thickness on oxidation time (A=0). 64

19 Grazing-incidence x-ray reflectance spectrum (red: model; blue: data) and electron density versus depth for sample 2 (33 nm thickness). 67

20 Ellipsometric angles ψ and Δ (symbols) at four angles of incidence (60°, 65°, 70°, 75°) for a Ge wafer with native oxide, after the standard clean described in Sec. 4.2. Two data sets from 0.5 to 3.0 eV and from 0.76 to 6.6 eV were merged. Lines: Data calculated from our model. 74

21 Same data as in Fig. 20, but displayed as a complex pseudodielectric function with real part $\hat{\epsilon}_1$ (green) and imaginary part $\hat{\epsilon}_2$ (blue). Data from our model are shown in red. 75

22 Ellipsometric angles (ψ, Δ) and depolarization (symbols) for 34 nm GeO_2 on Ge. Data from our model (lines). 77

23 As Fig. 22, but for a Ge wafer with 89 nm GeO_2. 78

24 As Fig. 22, but for a Ge wafer with 136 nm GeO_2. The model matches the maxima of ψ, but not the minima. This is a clear indication for a gradient in the refractive index of the film. 79

25 Complex dielectric function for Ge from a fit to our ellipsometry results in comparison with literature data.[63, 61, 76, 58, 107] . . 84

26 Complex dielectric function for GeO_2 from fit to our ellipsometry results in comparison with literature data.[70, 86] 87

27 To estimate the accuracy of the optical constants for GeO_2, we plot the dielectric function obtained from various methods: From a Tauc-Lorentz fit to all data assuming uniform oxide density, from fits of single samples (89 nm and 136 nm thickness) with uniform density, and a two-oscillator fit (Tauc-Lorentz and Gaussian) to all data allowing a density gradient for the thicker oxides. 88

28 Reflectance of Ni at 1.91 eV as a function of temperature [99]. . . 92

29 Real and imaginary parts of the pseudodielectric function of bulk polycrystalline Ni at 1.96 eV as a function of temperature. The arrows indicate the direction of the temperature ramp with increasing (right) or decreasing (left) temperature versus time. The dashed lines show the Curie temperature of Ni at 627 K. 98

30 Real and imaginary parts of the dielectric function of Ni at 300 K versus photon energy, taken from three different literature sources [104, 106, 107]. A vertical line was drawn at 1.96 eV, were our temperature dependent measurements were performed. 99

31 Normal-incidence pseudo-reflectance at 1.96 eV for bulk Ni as a function of temperature, calculated from the pseudo-dielectric function shown in Fig. 29. The dashed vertical line indicates the Curie temperature T_C for the first run. The inset shows the range near T_C. The arrows show the direction of the temperature ramp with increasing (right) or decreasing (left) temperature versus time. . . 103

1 INTRODUCTION

It is becoming increasingly important to understand the optical constants of materials such as complex oxides, thermal oxides and semiconductors, and metals in order to more effectively use and process them in electronic and photonic technologies.

Oxides are compounds that are now of much interest scientifically and industrially, some of the most famous being materials such as silica and strontium titanate. These oxygen-based materials have a wide range of interesting properties and applications. It is because of this usefulness that it is important to continue the study of the properties of oxides and the engineering of the structures containing them. It is the optical characterization of these materials for the purpose of scientific knowledge and metrology that is the focus of this work, and the purpose of this chapter is to introduce and explain the methods that were used.

The optical constants of metals are much less well known than those of semiconducting and insulating compounds, therefore we are continuing work on the optical constants of nickel as a function of temperature and magnetization.

The results presented in this thesis are the record of work done exemplifying several types of research that can be accomplished using spectroscopic ellipsometry in concert with a few other experimental techniques. These techniques included x-ray reflectivity, x-ray diffraction, Raman spectroscopy, and thermal

oxidation. The work presented here is original in that it extended the spectral region, improved the accuracy of already well-known materials, or is a confirmation of previous results.

The third chapter is concerned with the characterization of a bulk material, LSAT, which was accomplished using a combination of structural analysis using x-ray diffraction, vibrational analysis using Fourier transform infrared ellipsometry and Raman spectroscopy, and analysis of the electronic structure up to 6.5 eV using spectroscopic ellipsometry. This is an example of using spectral data to study the properties of a wide band gap bulk oxide. This is important when trying to understand the dynamics of a material when it is used in an applied setting so that the characteristics of a material are well known allowing the minimization of the uncertainties in performance.

The fourth chapter is a multi sample analysis of thermal GeO_2 on Ge allowing for an improvement of both the accuracy and spectral range of the germanium optical constants. This is important for metrology purposes in the semiconductor industry for use in germanium-based devices. XRR was also utilized as an aid in analysis of our samples and to compare to our optical model.

The final chapter is concerned with the change in the optical constants of nickel with magnetization and temperature. It is important, as mentioned before, to understand the conditions, which affect the optical response of materials. This also provides more information for discussion needed to ascertain the physics

causing the changes.

2 GENERAL THEORY AND METHOD

This chapter will describe some of the fundamental theory that I employed in the work presented in later chapters. This will include the basics of electronic band structure because this is the source of dispersion in the dielectric function in the near infrared, optical, and ultraviolet regions; phonons because these are the source of dielectric dispersion in the infrared region; and oxidation by diffusion of oxygen because that was used to prepare the samples in chapter 4.

The measurement theory and instrumentation, especially of spectroscopic ellipsometry and also of X-ray reflectivity, is also present for completeness.

2.1 Electronic Band Structure

As we have known now for over a century, the energetic states of atomic orbitals are quantized. When two atoms interact there may be electrons that are affected by states from both atoms simultaneously. As this happens, if we described our one atom system with a diagonalized Hamiltonian, we now find that, because of the overlap of states, the off-diagonal elements are non-zero. This occurs because the corresponding valence states between the two atoms that described the single atom system well are not orthogonal. Upon rediagonalizing the Hamiltonian of our system, we will find that the two overlapping states have become two non-

degenerate states called bonding and anti-bonding. This splitting occurs every time we bring another atom into our system.

At the molecular level, some of these split states become what is known as highest occupied molecular orbitals (HOMO) and lowest unoccupied molecular orbitals (LUMO). The HOMO states are where the valence electrons reside unless they become excited. The minimum excitation energy needed to send them to the LUMO is known as the HOMO-LUMO gap energy. As the splitting continues, we accumulate these quantized states into a group of states with energies that overlap at certain positions or very similar energies and this group is what we call a band, and specifically for the unexcited states this is called the valence band. The virtual excited states also split and they form what is known as the conduction band. Analogously to the HOMO-LUMO gap, we have a band gap, the energy needed to raise an electron up into the conduction band.

We can use group theory to assist us in constructing a model for a band structure if we are working with a crystal structure. If we are working with an amorphous material, we will see large broadenings and decreases in the gap energies as compared to the material's in crystalline form.

We usually discuss the band structure in terms of the Brillouin zone and its high symmetry points. An illustration of a band structure calculation is given in figure 1 from reference [1]. The high symmetry positions and crystal orientations are marked along the horizontal axis. The band structure shown at 0 K is an

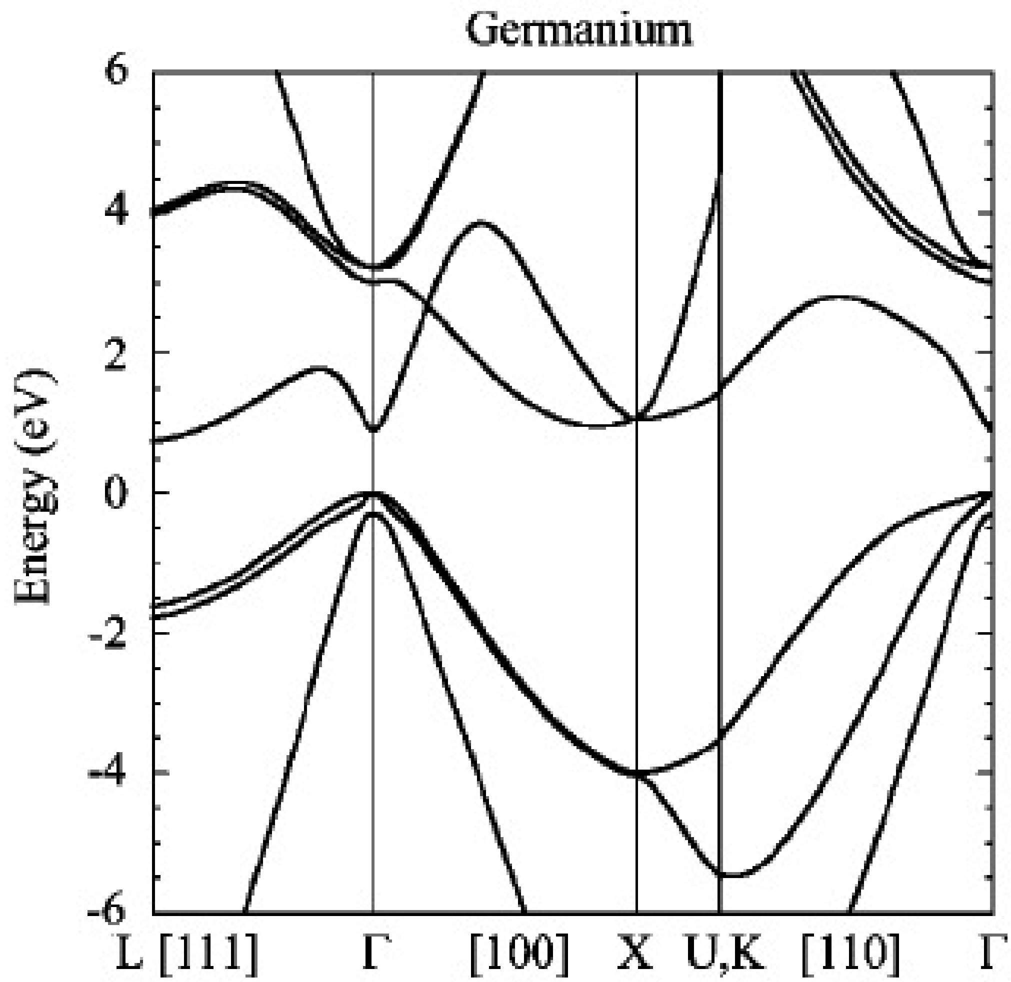

FIG. 4. Band diagram of Ge at $T=0$ K.

Figure 1: Calculation of the band structure of Ge at 0 K, taken from figure 4 of reference [1]

idealization of what the Ge band structure would look like without entropy or other thermal effects.

We are able to use ellipsometry to measure band structure critical points through modeling the second derivative of the dielectric dispersion if we have good accompanying theoretical calculations to check against. These transitions can either be indirect, where the transition requires a change of the direction of momentum of the electron through the means of phonon interaction, or direct, where the transition conserves the momentum. Indirect gaps are much less efficient than direct gaps and so are much harder to analyze with an optical technique such as ellipsometry.

A material is called either direct or indirect based on whether the lowest energy transition possible, the fundamental gap, is either a direct or indirect transition. Ge is an example of an indirect gap material, where the transition begins at the Γ point at the top of the valence band and moves towards the L point. Conductors are those materials for which a negligible amount of energy is needed to move an electron from the valence band to the conduction band.

These matters are discussed in much more depth in the texts of Kittel [2], Fox [3], and Harrison [4], [5].

2.2 Phonons

Phonons are an important area of research in materials. They are vibrations of the atoms in the material, whether that material be crystalline or amorphous. We can treat them quantum mechanically as a bosonic quasiparticle. There are two families of phonons, optical and acoustic. In this work, I am interested mostly in IR-active optical phonons, which are present when the oscillations assume the correct symmetry in the Brillouin zone and the bonds are polar. Knowledge of the phonons is important for understanding the structure of a material and transport properties such as heat and sound.

Knowledge of the phononic structure is also important when describing the redshift of interband transitions through phonon-electron interaction. Similar to interband transitions, we see phonons as dispersions in our dielectric spectra, although at lower energies than those of interband transitions.

Both families of optical and acoustic phonons can be split into two types of oscillations, transverse and longitudinal. We can write these as TO and LO, and TA and LA, for optical and acoustic.

We see IR active TO modes as peaks of absorption in our infrared dielectric spectra and LO modes as zeros, which can be more clearly seen as peaks in the inverse of the dielectric function. For every transverse mode, there is a correspond-

ing longitudinal mode at a higher energy in an isotropic system. In anisotropic systems, it is possible to see inverted peaks in the imaginary part of the dielectric spectra corresponding to the switching of TO and LO modes, although the materials discussed in the later chapters are isotropic in nature.

Again, the works of Fox [3], Kittel [2], and Harrison [5] are helpful resources on this subject.

2.3 Diffusion and Oxidation

Anything that can, will develop an oxide layer. Any oxide layer that has a thickness that exceeds 1-2 monolayers was formed by a diffusion-aided mechanism.

For many years, practioners of ellipsometry tried to create samples with pristine surfaces through cleaning methods, both chemical and mechanical, or through cleaving a sample in vacuum. This led to measurements of pseudo-dielectric functions that closely approached the material's true dielectric function. In order to increase the accuracy of optical constants beyond those achieved through surface optimization, it is necessary to do a numerical correction through fitting, which will be described later in this chapter.

In order to do our correction for GeO_2 on Ge, it was necessary to have a series of samples with varying oxide thicknesses. The reasoning and experimental methods behind this are described in chapter 4, and the purpose of this section

is to further discuss the theory behind the diffusion facilitated oxidation process and the information discussed here can be referenced primarily from the classic paper on oxidation of Si by Deal and Groves [68] and the text, *Diffusion in Solids*, by Mehrer [8].

Diffusion is essentially the mixing of some fluid with another medium, whether that be solid or fluid, through a random walk process. On the scale of moles of atoms and molecules, diffusion is most generally described by Fick's first law,

$$\vec{J}(\vec{r},t) = D\vec{\nabla}C(\vec{r},t), \tag{1}$$

and the continuity equation,

$$\vec{\nabla} \cdot \vec{J} + \frac{\partial C(\vec{r},t)}{\partial t} = 0, \tag{2}$$

where $\vec{J}$ is the flux, D is the diffusivity, and $C(\vec{r},t)$ is a scalar field representing concentration. Diffusivity is a material constant that describes how easily certain particles can move through it, it is given in units of the flux of particles per unit time. It is dependent upon the interaction between the materials that are mixing.

If we combine equations 1 and 2, we will have Fick's 2nd Law, the diffusion equation. If we then assume that the system in which the diffusion is occurring is homogeneous, then we can say that the diffusivity is not dependent upon the concentration and we can write the result as a linear second order differential equation,

$$\frac{\partial C(\vec{r},t)}{\partial t} = D\Delta C(\vec{r},t). \tag{3}$$

In the case of our systems of interest, we can reduce this equation from three dimensions to one because we consider our sample to be a film on a semi-infinite substrate, extending to infinity in both directions parallel to the surface.

In the paper by Deal and Grove[68], they argue that if the oxidation process has reached a steady state then the rate-limiting step is the diffusion through the already formed oxide layer. We can then say that compared to the time it takes for the oxidant to diffuse from the oxide, the reaction with the substrate occurs immediately upon reaching the interface. Figure 2 from reference [68] shows the model used to describe the thermal oxidation of Si and the solution for the fluxes in each medium; F_1, F_2, and F_3; which are the fluxes through the surface, the oxide layer, and interface respectively. This diffusion is driven by concentration differences at the boundaries.

The Deal-Grove model[68] for the oxidation of Si is given by the above discussion and gives rise to the mathematical description

$$x_0^2 + Ax_0 = B(t + \tau), \tag{4}$$

for

$$A \equiv 2D_{eff}(\frac{1}{k} + \frac{1}{h}), \tag{5}$$

$$B \equiv 2D_{eff}\frac{C^*}{N_1}, \tag{6}$$

$$\tau \equiv \frac{x_i^2 + Ax_i}{B}. \tag{7}$$

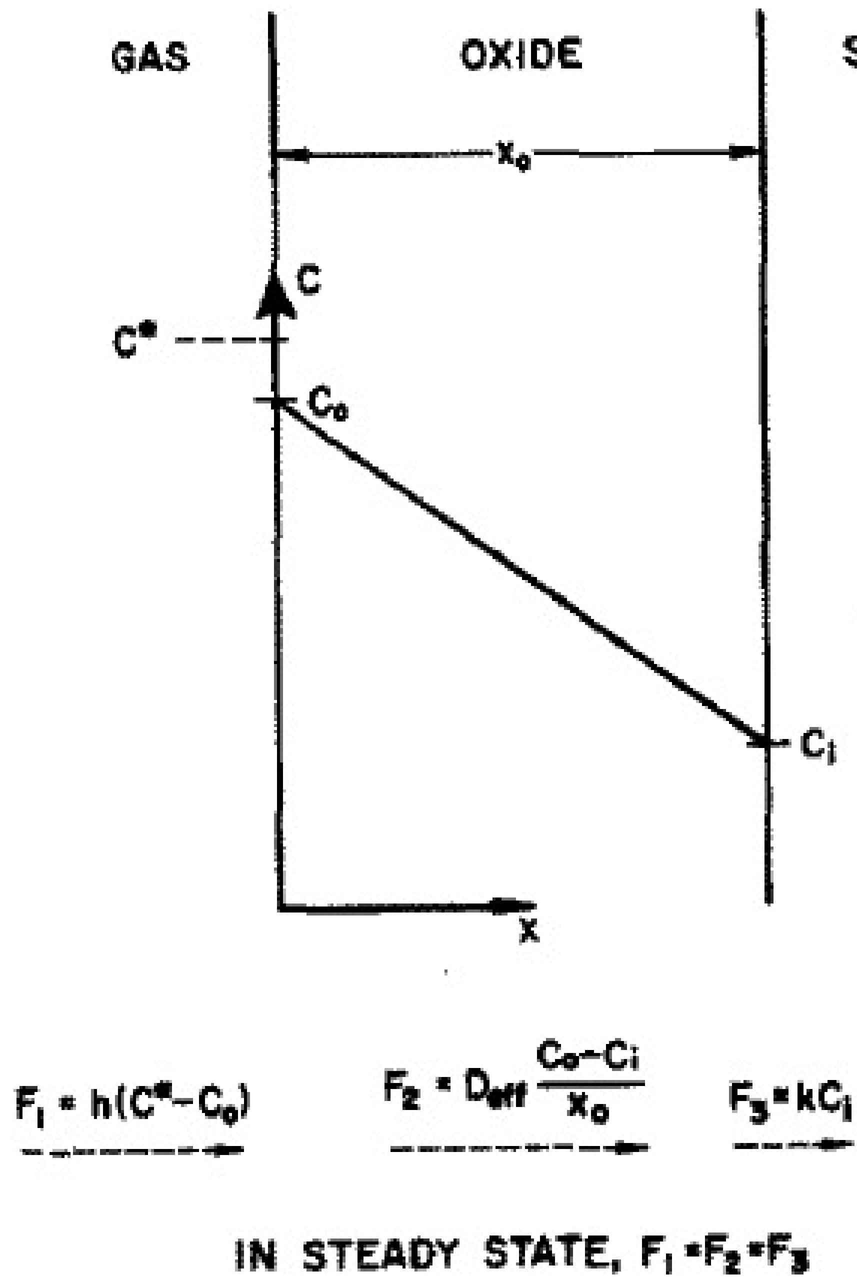

Figure 2: Figure 3 from reference [68] depicting the boundaries taken while solving the diffusion equation and the respective solutions of the flux for each stage of the model.

These equations give a relation between oxide thickness, x_0, and time, t, based upon the concentration of the oxidant and its interaction with the solid materials. A, B, and τ are composites of the physical constants x_i, the initial oxide thickness; D_{eff}, the effective diffusivity; k, the constant associated with oxidant flux and reaction at the interface; h, the gas phase transport coefficient; C^*, the equilibrium concentration of the oxidant in the oxide layer; and N_1, the number of oxidant molecules incorporated into a unit volume of the oxide layer.

I would like to briefly discuss the mechanisms of diffusion to the germanium surface that allow the Ge $+O_2 \longrightarrow GeO_2$ reaction to occur.

There are several classes of atomic level diffusion mechanisms discussed in reference [8]. These processes at the very simplest can be considered in terms of an atomic jump process in which the diffusant moves from one interstitial site (empty spaces between atoms in the crystal structure) to the next. This is essentially a random walk problem, which was solved by both Einstein and Smoluchowski[8], and the frequency of movement is usually an Arrhenius relation,

$$\Gamma = \nu^0 e^{-\frac{\Delta G}{kT}}, \tag{8}$$

where Γ is the jump rate, ν^0 is the attempt frequency, ΔG is the Gibbs free energy of activation, k is the Boltzmann constant, and T is the temperature. This is important because it relates to us that the fundamental mechanisms of simple diffusion increase rapidly with temperature.

This simple form of diffusion is known as the interstitial mechanism. While there are more complex mechanisms, we can assume, because of the low packing density of the Ge crystal structure and the small size of oxygen with respect to Ge, that our oxygen moves through our sample this way. It could be argued that the oxygen moves through the GeO_2 by more complex mechanisms as well, such as the vacancy or interstitialcy mechanisms. The Deal-Groves model that was discussed above assumes that the oxygen does not dissociate as it moves through the oxide however, and because of the success we show later in the modeling of our data we will content ourselves with theorizing the interstitial mechanism.

2.4 Spectroscopic Ellipsometry

The main focus of this work was to acquire and improve the knowledge of the optical constants of various materials through characterization by way of inverse problem solving. The way that the data was acquired was by the use of the measurement technique, spectroscopic ellipsometry, which has been used for well over a century and has enjoyed a large increase in use since the onset of computer controlled systems that are able to take large amounts of data, thereby decreasing the temporal cost and increasing the rate of data analysis. It is currently used widely in the optical characterization of many different types of materials, especially those useful to the semiconductor and related industries. Its uses are

continually growing and being developed for applications that were not foreseen or possible several decades ago. This section attempts to overview the theory and instrumentation of ellipsometry in reference to the flavors used in the presented work.

2.4.1 Theory

General Theory General ellipsometric theory can be summed up in the two equations,

$$\rho = \frac{R_p}{R_s} = \frac{E_p}{E_s} = \tan \Psi e^{i\Delta}, \tag{9}$$

and

$$< \tilde{\epsilon} >= \sin^2\phi \; [1 + \tan^2\phi \; (\frac{1-\rho}{1+\rho})^2], \tag{10}$$

where R_p and R_s are the total coefficients of reflection from a system of material layers (s, polarized perpendicular to the surface; and p, polarized parallel to the surface), Ψ is the angle of which the tangent is the ratio of the moduli of the reflection coefficients is of, and Δ is the relative difference in phase shift between the two polarization directions, ρ is the ratio of complex reflection coefficients, ϕ is the angle of incidence, and $<\tilde{\epsilon}>$ is the complex pseudo-dielectric function. For the sake of easy conceptualization, the two quantities, Ψ and Δ, are depicted in Figure 3.

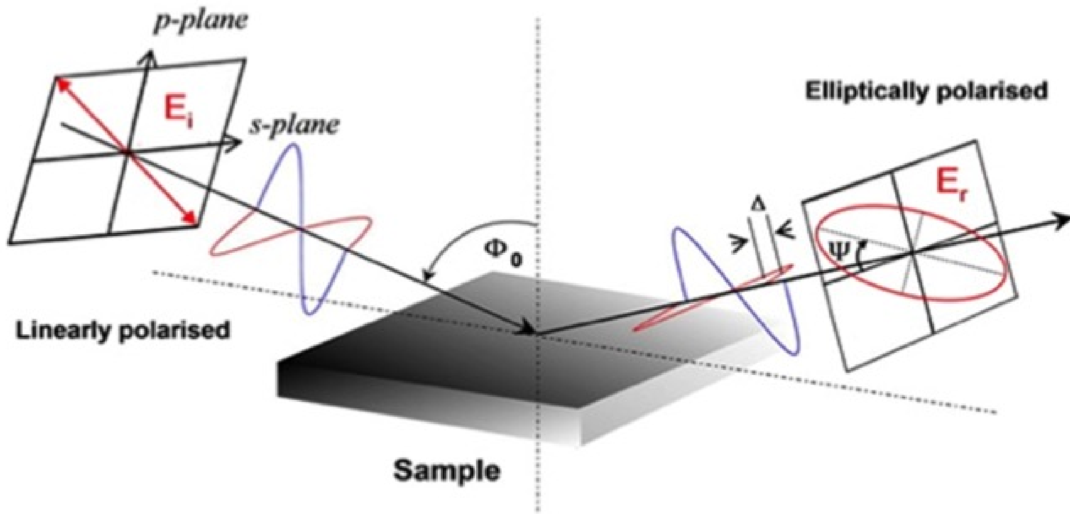

Figure 3: A geometric depiction of the physical meaning of the ellipsometric angles.

The above equations specify the relationship between the measured quantities of ellipsometry and the pseudo-dielectric function, which is the square of the pseudo-complex index of refraction. When the term *pseudo*-dielectric function is used, it means that all dielectric functions, interfaces, defects, and instrumental effects are coupled together to create the spectra calculated from the measured ellipsometric angles.

The pseudo-dielectric function is analyzed by way of inverse problem solving, which has already been mentioned, in the form of a model specifying the number of different layered materials and surface and interface conditions. Given the correct number of degrees of freedom, the thickness, complex dielectric function (index of

refraction), composition of the materials present in the structure may be obtained if there is a sufficient amount of information from the characteristic in the change in polarization state of the light, formally known as the ellipsometric angles Ψ and Δ as defined above in Equation 9.

Model Theory There are several ways to construct models for the analysis of materials, including oscillator sums, parametric, and factorized models, which are used in the work, presented later. The Lorentz oscillator, Tauc-Lorentz oscillator, semi-conductor parametric oscillator model, and the Lyddane-Sachs-Teller factorized dispersion model are all used in order to describe the dispersion present in the dielectric functions. We will discuss the form and possible physical meaning of these models, however going forward we need to keep in mind that for much ellipsometric modeling we never claim that the numerical parameters that give the models their form, in general, lend themselves to strenuous quantitative interpretation. The particulars of data analysis will be discussed in a later section.

Lorentz Oscillator The Lorentz oscillator was originally developed by Hendrik Lorentz as a solution to the problem of two charged particles in a bound state. His assumptions, given as an electron bound electrically to a nucleus, led him to describe the system as a three dimensional classical oscillator model, driven by a time varying electric field and damped by energy loss through the radiation

created through charge acceleration. We can write this equation as

$$\ddot{\vec{r}} + \gamma\dot{\vec{r}} + m\omega^2\vec{r} = \frac{e}{m}\vec{E}(\vec{r},t), \tag{11}$$

which, for isotropic systems, we can treat one dimensionally (otherwise we have dimensional correlations);

$$\ddot{x} + \gamma\dot{x} + m\omega^2 x = \frac{e}{m}E(x,t). \tag{12}$$

We can find any answer as a superposition of the homogeneous and non-homogenous solutions to the equation. The complex dielectric function is given as

$$\epsilon_1(h\nu) = 1 + \frac{A(E^2-(h\nu)^2)}{(E^2-(h\nu)^2)^2 + C^2E^2},\ \textit{and} \tag{13}$$

$$\epsilon_2(h\nu) = \frac{ACE}{(E^2-(h\nu)^2)^2 + C^2E^2}, \tag{14}$$

which are completely described by the three parameters amplitude, A, broadening, C, and peak position, E[9].

This simple relation gives results which are surprisingly similar to more complete theory and experiment when applied to hydrogenic systems. This oscillator also very nicely describes the line shapes of many dielectric dispersion phenomena and has been in fact one of the most useful of such modeling tools.

Tauc-Lorentz Oscillator We have previously discussed the Lorentz oscillator, which as aforementioned, has been very useful. The problem with this

description is clearly seen when we consider materials in possession of a band gap. This requires that the value of the imaginary part of the dielectric function be nil below the onset of absorption, however the Lorentz oscillator only goes to zero as the distance from the peak tends toward infinity. A solution to this problem was presented by Jellison *et. al.*[6] by using a density of states solution of an amorphous semiconductor above the fundamental gap given by Jan Tauc *et. al.*[7] written as

$$\epsilon_2(h\nu) = \Theta(h\nu - E_g)\frac{A_T\ (h\nu - E_g)^2}{h^2\nu^2}, \tag{15}$$

where Θ is the Heaviside function, A_T is the amplitude, and E_g is known as the Tauc gap, taken to be the band gap energy or onset of absorption.

As is explained in Jellison *et. al.*'s paper[6], equations 15 and 14 are multiplied together to give the imaginary part of the Tauc-Lorentz oscillator,

$$\epsilon_2(h\nu) = \Theta(h\nu - E_g)\left[\frac{AE_0C(h\nu - E_g)^2}{h\nu(h^2\nu^2 - E_0^2 + Ch\nu)(h^2\nu^2 - E_0^2 - Ch\nu)}\right], \tag{16}$$

where as before, Θ is the Heaviside function, E_g is the onset of absorption, A is the amplitude, E_0 is the peak position, and C is the broadening, and all variables are in units of energy. The real part, achieved through the Kramers-Kronig relation, will not be written down, however it can be found in the previously mentioned paper[6].

The advantage of this model is that it includes only one extra parameter with respect to the Lorentz oscillator and gives the physical result of there being no

absorption below the onset of absorption.

Semiconductor Parametric Oscillator The previous two models honor our sense of the necessity of simplicity, however we must leave that behind in some instances when the accuracy of the model is greatly improved by increasing complexity. This model was developed at and patented by the J. A. Woollam Company [85].

It claims to have a low correlation of parameters and provides oscillator sums with the ability for oscillator linking and anisotropy. It is a very effective model for the description of complex semiconductor spectra such as Ge, GaAs, etcetera.

Lyddane-Sachs-Teller Factorized Dispersion Model We can write any well-behaved complex function as a multiplication of zeros and poles. In the case of dielectric dispersion, Lyddane, Sachs, and Teller developed a model [10] in which they related the frequencies of TO and LO phonons to the static imaginary part of the index of refraction and the value of the imaginary part of the index of refraction about the phonon energies. This was modified to include broadening and multiple phonons by Lowndes[11].

It is given as

$$\epsilon\left(\omega\right)=\epsilon_{\infty}\prod_{i}\frac{\omega_{i,\mathrm{LO}}^{2}-\omega^{2}-i\gamma_{i,\mathrm{LO}}\omega}{\omega_{i,\mathrm{TO}}^{2}-\omega^{2}-i\gamma_{i,\mathrm{TO}}\omega}. \tag{17}$$

This model allows us to describe any phonon dispersion in terms of the LO and

TO phonon energies and broadenings. We can clearly see that if we invert this, the poles and zeros will be switched and give a dispersion based on the LO phonons as was mentioned in the previous discussion on phonons.

Depolarization Theory While most of ellipsometric theory is focused on the *change* in polarization state of light, there is quite a bit to be said of the *depolarization* of light upon reflection. It occurs when the light, which is initially polarized, is frustrated. This frustration can occur for several reasons such as inhomogeneities within a material, surface defects, and interface non-idealities such as being non-planar.

Physically this is caused by parts of the beam taking slightly different paths on the order of the coherence length. Because the measurement is taken on the basis of relative reflection intensities of the polarization angles, the field is treated as E^2. Although this is a troublesome scenario, we can use several algorithms to use the depolarization to glean information on the structure and quality of our samples.

For a discussion of depolarization, see the text by Fujiwara [9].

2.4.2 Instrumentation

We discussed above the theory of ellipsometric measurement and in this sec-

tion we will now discuss the actual instrumentation needed to do the work that is described later. This of course is in no way exhaustive as a description of ellipsometric instrumentation as there are many variations and optimizations available as well as new configurations being developed currently for very specific usage. That being said, every ellipsometer needs to have the components necessary to produce and polarize light, a stage for the sample, which the light is reflected from, and a way to detect the light and its polarization. There were three different instruments used for this work, two that I personally used at NMSU and the CINT facility at the Sandia National Laboratories in Albuquerque, and one at the University of Fribourg in Switzerland that produced data in an energy range below that which was achievable in our present setup.

Near Infrared to Near Ultraviolet

The machine used to take measurements in the range of 6.6-0.5 eV (190-2500 nm) is an automated, rotating analyzer vertical variable angle of incidence spectroscopic ellipsometer (V-VASE) acquired from the J. A. Woollam Company. This machine is housed in Gardiner Hall and maintained by our research group.

Our ellipsometer consists of several different modules including a VB-400 unit, which communicates with the computer and controls the various motors, an HS-190 monochromator, an optical fiber, a focusing lens, a polarizer, an Autoretarder (Berek waveplate compensator), a sample stage, an analyzer and a solid-state

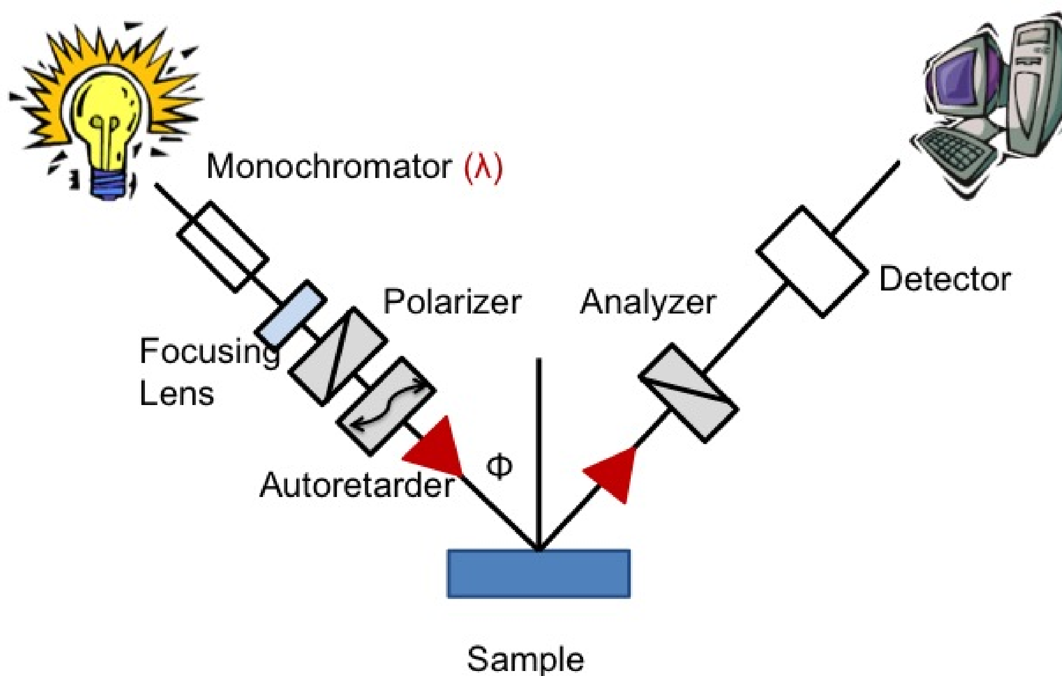

Figure 4: A cartoon of our rotating analyzer V-VASE.

detector.

Figure 4 is a cartoon of the instrument setup and figures 5 and 6 are photos of our instrumental setup.

I will now give brief descriptions of the components of our system that were mentioned earlier.

The HS-190 monochromator houses the light source, which can either be a Xe short-arc lamp or W-halogen lamp depending upon the wavelength range we want to utilize. It also houses three gratings. The gratings are optimized for different spectral regions and allow us to select the wavelength we want to measure with at a given time. The light is then selected by passing it through an opening of

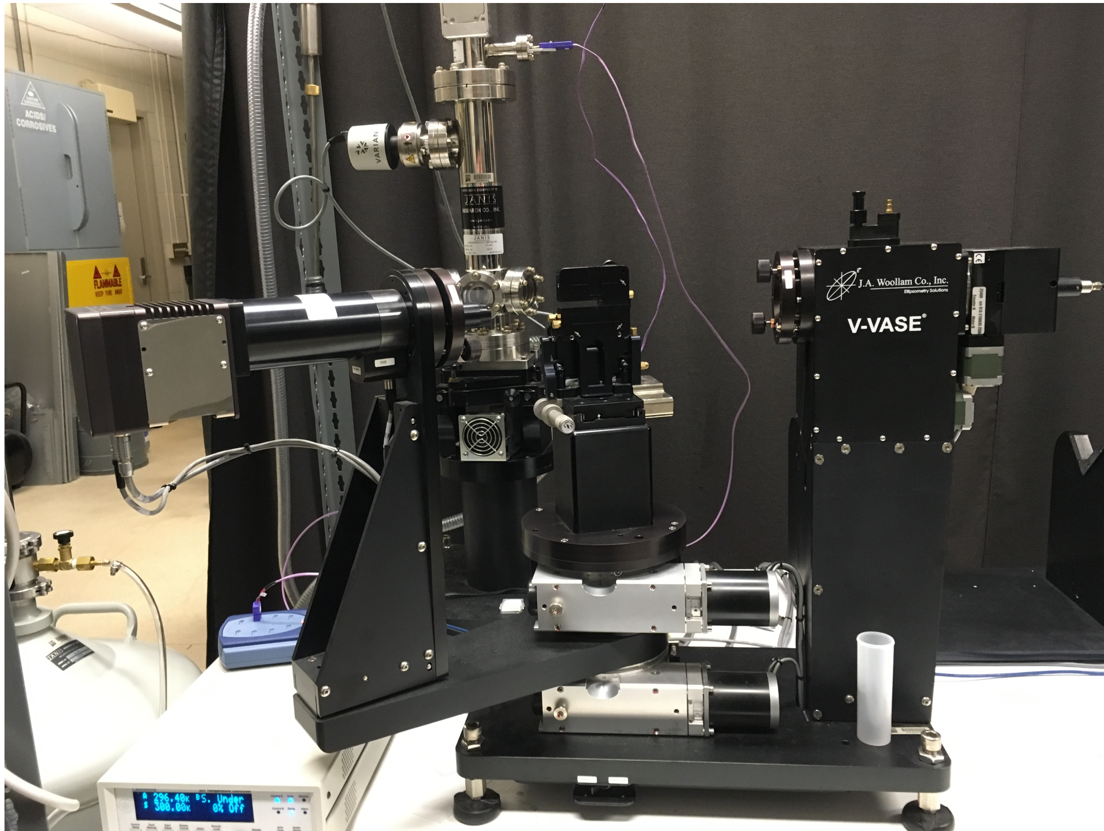

Figure 5: A picture of our rotating analyzer V-VASE. Present in the photo (from left to right) is the end of the fiber-optics cable; the housing for the focusing lens, polarizer, and Autoretarder; the sample stage; and the housing for the analyzer and detector. The two goniometers used for rotating the sample stage and detector arm are also seen below the sample stage.

Figure 6: A picture of our monochromator, controller, and sample stage vacuum (left to right).

variable width and then is given a modulation frequency by a chopper in order to distinguish the signal from ambient light.

At the back of the monochromator is the fiber-optic cable attachment, which is also attached at the other end to the ellipsometer. The light goes through a focusing lens that can be adjusted to achieve the desired spot size and aligned for the proper beam path. The light is then linearly polarized before being sent out where it reflects off of a vertically mounted sample.

The samples are held on by rough vacuum facilitated by the machine seen at the far left in figure 6. The sample stage is seated on a goniometer that allows for variable angle of incidence. The detector arm also is controlled by a goniometer that is set below the sample stage goniometer.

In the case of temperature dependent measurements we use a Janis special order cryostat from the J. A. Woollam Company with fused quartz windows set to 70 degrees incidence. This system allows us to take measurements of samples between temperatures of 80 and nearly 800 K. We have modified the apparatus of this system slightly by adding a second thermocouple that goes to the sample surface. We have also added a second roughing pump that is attached to the cryogen space when we take measurements at temperatures above ambient.

Far Infrared to Near Infrared

For our far infrared measurements, used to study the phonon dispersion,

Figure 7: A picture of a Woollam IR-VASE instrument.

we use the J.A. Woollam IR-VASE housed at the Center for Integrated Nano-Technologies at Sandia National Labs. Figure 7 is a picture of an IR-VASE.

The IR-VASE is designed to take in air measurements in a broad range, from 200-8000 cm^{-1}. The main difference between the IR-VASE and the previously described V-VASE is that the measurement method is FTIR and the light source is a glo-bar.

2.4.3 Data Analysis

We analyze our spectroscopic data with WVASE32 software from the J. A. Woollam Company. This is a very powerful software package allowing for multi-layer and sample analysis. The program models spectra based on input functions, oscillator models, and previously compiled optical constants. Analysis of the spectra gives information such as thickness, dielectric functions of the materials present and so on. We can also model the depolarization in our spectra with

various non-idealities.

Once we have created our models, we can fit them to the data in order to obtain more accurate information. The measure of the quality of the function we use is called the mean-squared-error (MSE), which is given as,

$$MSE = \sqrt{\frac{1}{2N - M}\chi^2}, \tag{18}$$

where N is the number of data points (Ψ/Δ pairs) and M is the number of parameters varying in our model. We want to minimize the MSE when fitting our data.

2.5 X-Ray Reflectance

X-ray reflectivity is a very useful technique for corroborating and refining our ellipsometric models. The system we used is a Panalytical X-ray diffractometer.

The information gained by this technique includes roughness at the surface and interfaces seen as the decay of the reflectivity signal, the electron density of the materials seen by the critical angles (where there is total external reflection prior to this), and the film thickness seen in the oscillations in the spectra. The information about the system is extracted by modeling the spectra.

3 OPTICAL CONSTANTS, BAND GAP, AND INFRARED-ACTIVE PHONONS OF $(LaAlO_3)_{0.3}(Sr_2AlTaO_6)_{0.35}$ (LSAT) FROM SPECTROSCOPIC ELLIPSOMETRY

This chapter is the original submission to JVST A prior to editing after review. It will be possible to find the final paper under the same name.

T. Nathan Nunley[1], Travis I. Willett-Gies[1], Jacqueline A. Cooke[1], Felicia S. Manciu[2], P. Marsik[3], C. Bernhard[3], Stefan Zollner[1]

[1] Department of Physics, New Mexico State University, MSC 3D, P.O. Box 30001, Las Cruces, NM 88003-8001, USA

[2] Department of Physics, University of Texas at El Paso, El Paso, TX, 79968, USA

[3] Department of Physics and Fribourg Center for Nanomaterials, University of Fribourg, Chemin du Musee 3, CH-1700 Fribourg, Switzerland

Abstract

Using spectroscopic ellipsometry, the authors determined the optical constants (complex dielectric function) for $(LaAlO_3)_{0.3}(Sr_2AlTaO_6)_{0.35}$ (LSAT) from 0.01 to 6.5 eV. Above 0.5 eV, the data were described with a sum of two Tauc-Lorentz oscillators and two poles. A direct gap of 5.8±0.1 eV was found. An Urbach tail extends to even lower photon energies and makes the crystal opaque above 4.8 eV. Using FTIR ellipsometry, the lattice dynamics was studied. Nine pairs of transverse/longitudinal phonons were found and attributed to disorder in the La/Sr sublattice, ordering in the Al/Ta sublattice, and two-phonon absorption.

3.1 Introduction

Perovskite oxides like $SrTiO_3$ and related compounds with a generic formula ABO_3 have interesting properties, such as ferroelectricity, superconductivity, high dielectric constants, combined with a large band gap, which may lead to interesting electronic, optoelectronic, or energy-conversion applications.[12] These properties can often be tuned by strain engineering,[13] which requires epitaxial growth on a variety of substrates with different lattice constants.[14]

One common perovskite substrate material has the chemical formula $(LaAlO_3)_{0.3}$ $(Sr_2AlTaO_6)_{0.35}$, equivalent to $(La_{0.3}Sr_{0.7})(Al_{0.65}Ta_{0.35})O_3$, which is usually abbreviated as LSAT. It has been used as a substrate for epitaxial growth[15, 16, 17, 18] of $PbVO_3$, $EuTiO_3$, NbO_2, $NaNbO_3$, and many other materials. Unlike $LaAlO_3$ (another common substrate, which has a rhombohedral crystal structure[19]), LSAT is cubic. LSAT substrates therefore are untwinned and allow higher quality epitaxial growth than commercial twinned (pseudocubic) $LaAlO_3$ substrates. The cubic structure leads to an isotropic dielectric function.

LSAT is usually treated as a simple cubic (SC) perovskite at room temperature[20] with space group $Pm\bar{3}m$ (221) and a lattice constant a=3.868 Å, consistent with random occupation of the A (La/Sr) and B (Al/Ta) sites. On the other hand, ordering at the Al/Ta sites,[21, 22] similar to Sr_2AlTaO_6 (SAT), leads to a face-centered cubic (FCC) crystal structure with a lattice constant of a=7.73 Å and

an $F\bar{4}3m$ (216) space group. Sublattice disorder or ordering will affect the phonon symmetries in the crystal.[23] Some crystals have both ordered and disordered domains.[21]

Spectroscopic ellipsometry[24, 9, 25, 26] is an important technique to characterize epitaxial films on a substrate and allows conclusions about the electronic and vibrational structure of epitaxial materials. Therefore, the detailed and precise knowledge of the dielectric function of LSAT is crucial. In this article, we present new information about the optical constants of LSAT and about its electronic and vibrational properties.

Previous studies of the dielectric function ϵ of LSAT and its electronic and vibrational properties have been limited. Transmission measurements[27, 28] established the absorption edge (near 260 nm) and a broad defect absorption band near 450 nm, responsible for the color of the crystal, which depended on annealing conditions. The refractive index $n=\sqrt{\epsilon}$ in the transparent region was determined using the minimum-deviation prism method[28] and by spectroscopic ellipsometry[14] and fitted with the Sellmeier equation.

The zone-center phonons were studied using infrared reflectance,[23, 29] far-infrared ellipsometry,[30] and Raman spectroscopy.[23] The symmetries of these phonons for the two possible (ordered and disordered) space groups were also identified.[23]

3.2 Experiment and Models

Czochralski-grown LSAT wafers with colorless to light brown appearance and (100) surface orientation (less than 0.5° miscut) were obtained commercially (MTI Corporation, Richmond, CA). Single-side polished wafers were used for spectroscopic ellipsometry and infrared ellipsometry from 0.8 to 6.5 eV and 0.03 to 0.7 eV, respectively, while transmission measurements were performed on two-side polished wafers with 0.5 mm thickness. The surface roughness was specified by the supplier to be below 8 Å.

Figure 8 (a) shows a symmetric $\omega/2\theta$ x-ray diffraction (XRD) scan for the LSAT (100) substrate obtained with Cu $K_{\alpha1,2}$ radiation on a PANalytical Empyrean diffractometer. Miller indices are marked in the SC notation, where all (*hkl*) reflections are allowed. The lattice constant was determined to be 3.870±0.002 Å. The FWHM of the (200) rocking curve (ω scan at fixed 2θ value), obtained with a hybrid monochromator, was 0.05°. This is larger than for a Si (100) substrate (FWHM=0.01°), but significantly smaller than for a twinned $LaAlO_3$ substrate, allowing better alignment of epitaxial films on LSAT than on $LaAlO_3$.

In the double perovskite (ordered) FCC structure of Sr_2AlTaO_6, the Miller indices are doubled relative to the SC perovskite structure, but the FCC (hkl) indices must all be either even or odd for allowed reflections. Therefore, all (h00) SC reflections in a symmetric $\omega/2\theta$ scan as shown in Fig. 8 (a) are also allowed

in the FCC structure, where we would denote them as (2h00). To show evidence of ordering, we must look for FCC (hkl) reflections with odd indices, since these are equivalent to (forbidden) half-integral Miller indices in the SC structure.[21] This requires asymmetric reflections for an LSAT (100) surface.

We indeed find strong FCC (115), (117), and (555) Bragg reflections as clear evidence of ordering in our sample. Figure 8 (c) shows a ϕ scan of the FCC (115) Bragg reflection, where the sample is rotated about its surface normal for fixed incidence and diffraction angles satisfying the (115) Bragg condition. The four-fold symmetry of the (100) surface is apparent in the ϕ-scan. The (115) Bragg peak has a rather large 2θ half-width of 0.6°, which corresponds to an approximate size of 15 nm for the ordered domains, if the Scherrer formula is applied. This domain size is consistent with previous XRD and transmission electron microscopy of LSAT.[21]

Raman measurements were performed at 300 K in a backscattering geometry with an alpha 300R WITec system, using the 532 nm excitation of a Nd:YAG laser and a 20X objective lens with a numerical aperture (NA) of 0.4. The complete Raman spectrum was acquired from an accumulation of 10 scans, with each scan at an integration time of 50 ms. The Raman signal was detected by a 1024×127 pixel Peltier cooled CCD camera with a spectral resolution of 4 cm^{-1}.

Prior to the ellipsometry measurements, wafers were cleaned in a Novascan PSD Pro series digital UV ozone system utilizing a Hg vapor lamp. This clean

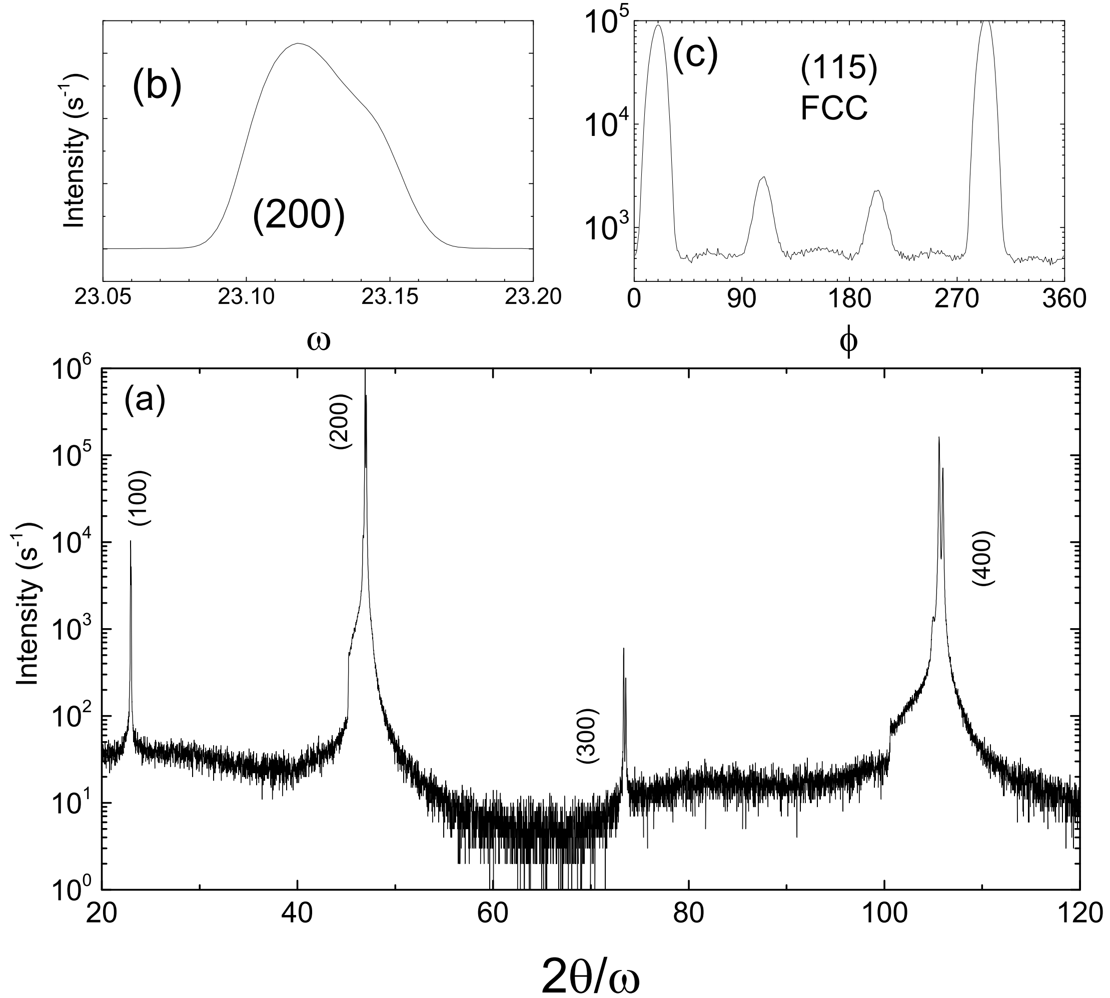

Figure 8: (a) Symmetric $2\theta/\omega$ x-ray diffraction scan for an LSAT wafer with (100) orientation. Miller indices are indicated in the simple cubic perovskite notation. (b) Rocking curve for the (200) Bragg reflection with a FWHM of 0.05°. (c) ϕ-scan of the (115) Bragg reflection of the ordered FCC LSAT structure.

had the purpose to remove organic contamination from the surface. It was performed in an oxygen-enriched environment for 30 minutes with the Hg lamp on and the sample on a heating stage held at 150°C, followed by a 30-minute period of incubation with the lamp off and the sample cooling to room temperature.

The ellipsometric angles ψ and Δ from 0.8 to 6.5 eV were determined at 300 K in air on a J.A. Woollam vertical variable-angle spectroscopic ellipsometer with computer controlled Berek waveplate compensator (J.A. Woollam Co, Lincoln, NE). We selected angles of incidence ϕ between 60° and 80°. The same instrument was also used to perform transmission measurements at normal incidence, using a measurement without sample as the reference. In the mid-infrared spectral region from 250 to 8000 cm^{-1}, ψ and Δ were acquired at 300 K on a J.A. Woollam Fourier-transform infrared ellipsometer as described elsewhere.[19, 31, 97] We also merged our data with far-infrared ellipsometry[33] results taken for a different sample (obtained from Crystec GmbH, Berlin, Germany) at ϕ=75° from 80 to 650 cm^{-1} presented previously.[30] There is excellent agreement between the far-infrared and mid-infrared data in the region of overlap.

The ellipsometric angles are influenced by the surface conditions of the sample, which include surface roughness and overlayers, especially organic contaminants. Therefore, it is desirable to reduce the surface layer thickness as much as possible. A roughness correction using the Bruggeman effective medium approximation with a 50/50 mixture of LSAT and voids allows to consider the remaining surface

effects numerically. To describe the large ellipsometry data set, it is convenient to represent the dispersion of LSAT with parametric models. The Sellmeier equation and the Tauc-Lorentz model have been particularly useful. The parameters governing the dispersion and the surface roughness layer thickness are adjusted to minimize the deviation between the data and the fit, weighted by the experimental errors in the data. These technical details are well described in ellipsometry textbooks[24, 9, 25, 26] and our prior research[19, 31, 97] on NiO and $LaAlO_3$.

3.3 Results from near-IR to UV at 300 K

The transmission through a two-side polished LSAT substrate with 0.5 mm thickness is shown in Fig. 9 (dashed). Since the refractive index n=1.99 at 1 eV (see below), the reflection loss at each surface is 11%, leading to a transmission of 79% in the absence of absorption, consistent with the measured transmission in Fig. 9.

The absorption coefficient α can be calculated from the transmission, if the thickness of the sample (0.5 mm) and the dispersion of the refractive index (see below) are known.[34] Results are shown in Fig. 9 (solid). The absorption coefficient is very small at low energies (not measurable) and rises sharply between 4.6 and 4.8 eV (260 nm), near the fundamental absorption gap of LSAT, as reported previously.[27] The position of this absorption edge depends on the thickness of the sample and details of the instrumentation. Our transmission measurements are unable to determine if this band gap is direct or indirect.

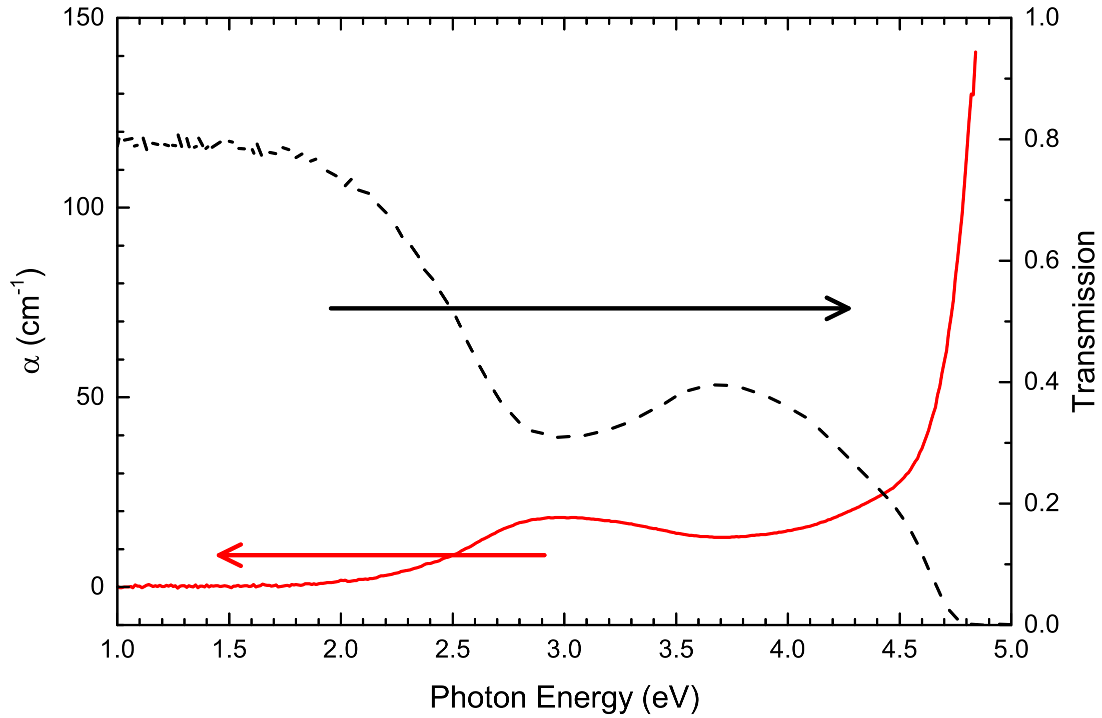

Figure 9: Transmission (dashed) and absorption coefficient (solid) for a two-side polished LSAT wafer with 0.5 mm thickness obtained at 300 K from a normal-incidence transmission measurement.

There is also a minimum in the transmission and a peak in the absorption coefficient near 410 nm (3.0 eV). This absorption band has been seen previously[27] and can be reduced by annealing at 1650°C in Ar with a trace of hydrogen. Presumably, it is due to defects, not related to the bulk electronic band structure. A similar absorption band within the gap was found in SiC, where it was explained by inter-conduction band transitions.[35]

The ellipsometric angles ψ and Δ taken at angles of incidence between 60°

and 80° are shown in Fig. 10 (symbols). The depolarization was small (below 1% throughout the spectral range) and not related to the sample. Since LSAT is transparent throughout the visible, a Cauchy fit gives an excellent description of the data, if a surface roughness layer (described using the Bruggeman effective medium theory as a 50/50 mixture of LSAT and voids) of 19.1 Å thickness is considered. The S-like transition of Δ from 0 to 180° near the Brewster angle (between 64° and 70°, depending on the photon energy) is most sensitive to surface roughness. Therefore, measuring at many incidence angles is helpful to accurately determine the surface roughness layer thickness.

A good description of the data between 0.8 and 6 eV can be achieved using a single Tauc-Lorentz oscillator, with poles at 0.08 eV (fixed) and 11.556 eV (variable) to take into account dispersion from absorption peaks outside of our spectral range. The agreement can be improved slightly, especially above 6 eV, if a second Tauc-Lorentz oscillator is added. The best fit to the data with two Tauc-Lorentz oscillators is shown by solid lines in Fig. 10. The Tauc-Lorentz and pole parameters obtained from the fit are shown in Table 1. In both cases, the rms deviation between fit and data is about 50% larger than the experimental errors.

The experimental data and fit are also displayed as a pseudo-dielectric function $\langle\epsilon\rangle$ in Fig. 11. The pseudo-absorption below the band gap due to surface roughness is clearly visible.

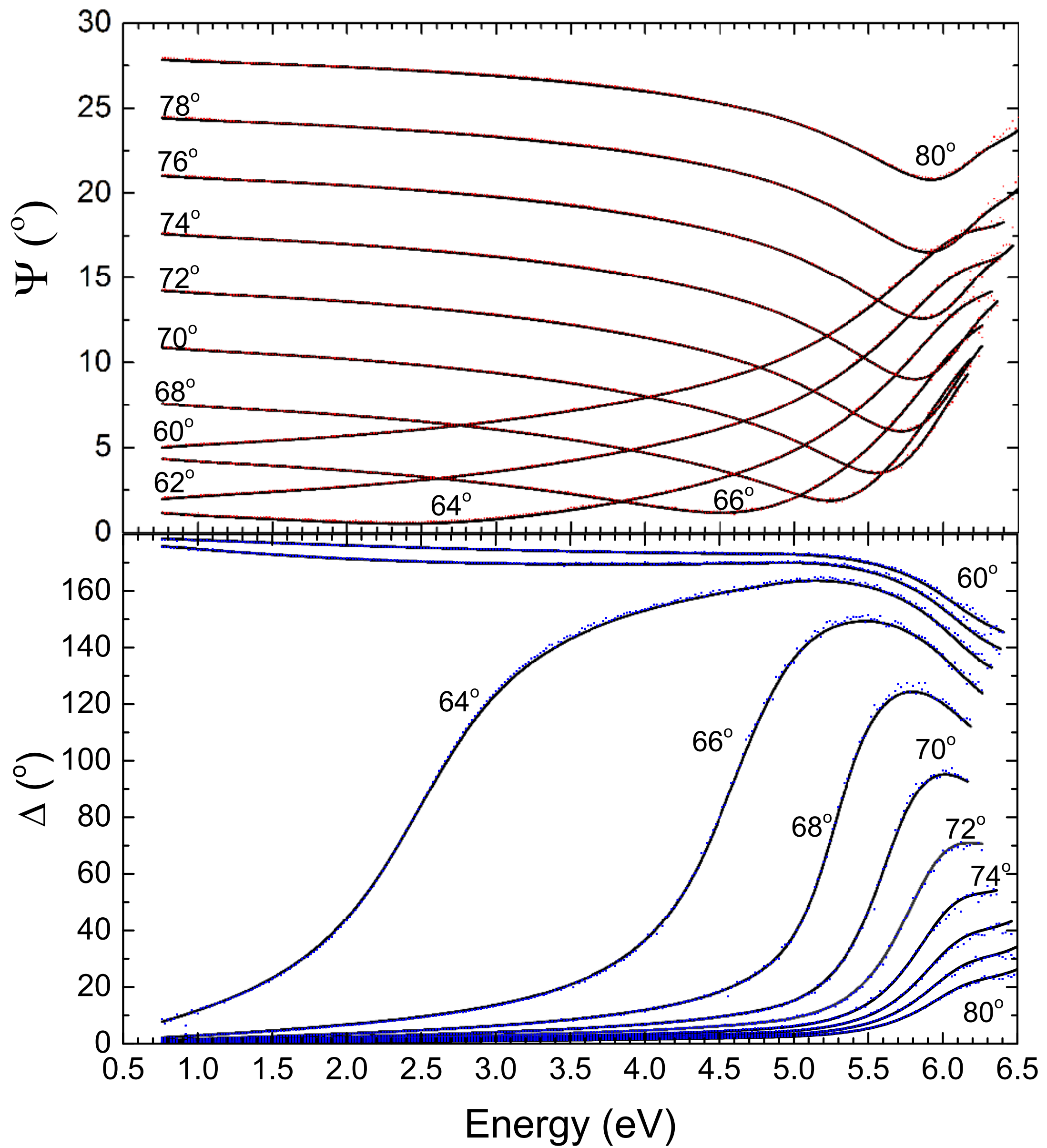

Figure 10: Ellipsometric angles ψ and Δ versus photon energy for incidence angles from 60° to 80° (symbols) for LSAT at 300 K. The lines show a fit with two poles and two Tauc-Lorentz oscillators, assuming a surface roughness of 19.1 Å.

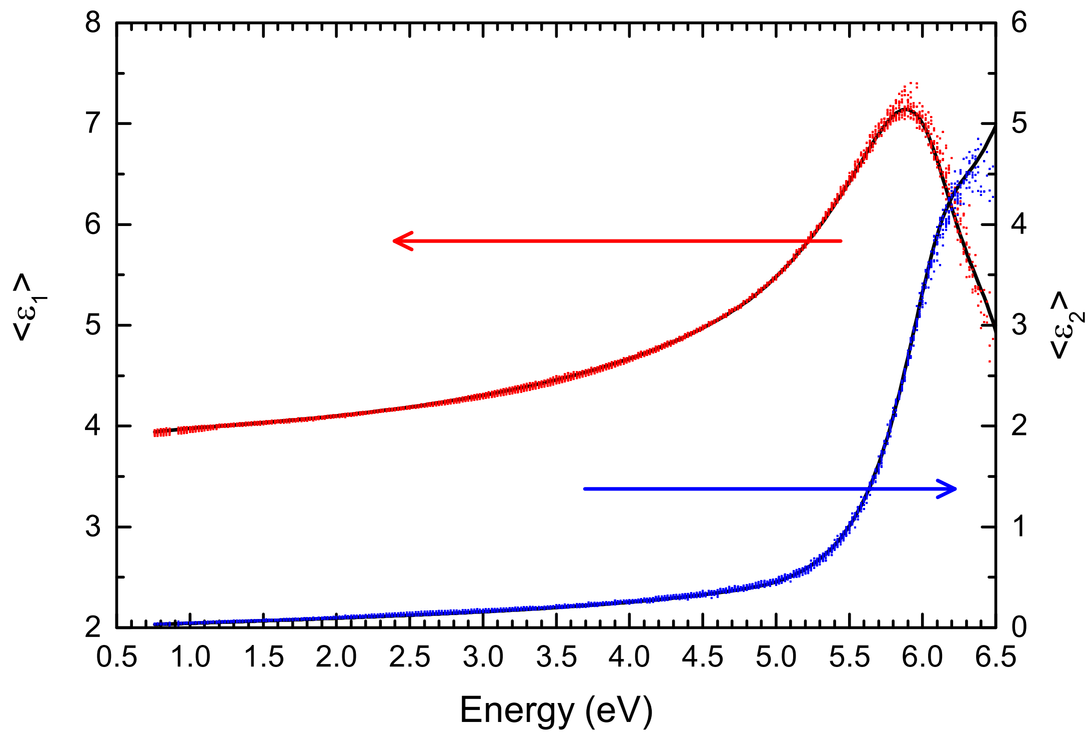

Figure 11: Same data as in Fig. 10, but displayed as a pseudo-dielectric function.

Table 1: Tauc-Lorentz (TL) parameters energy E, broadening Γ, amplitude A, and Tauc gap E_g for describing the dielectric function of LSAT at 300 K from 0.8 to 6.5 eV with one or two TL oscillators, obtained by fitting the parameters to the data in Fig. 10. The IR and UV pole energies and amplitudes are also listed. Probable errors are given in parentheses. (f) indicates that the parameter was fixed.

No.	E (eV)	A	Γ (eV)	E_g (eV)
TL1	6.292(7)	126(2) eV	1.21(2)	5.007(9)
UV pole	11.56(4)	272(2) eV^2		
IR pole	0.08(f)	0.026(1) eV^2		
TL1	6.14(2)	53(6) eV	0.84(3)	4.87(1)
TL2	6.67(4)	38(7) eV	0.7(1)	same
UV pole	11.56(4)	289(2) eV^2		
IR pole	0.08(f)	0.027(1) eV^2		

Finally, we show the dielectric function of LSAT from our model with two Tauc-Lorentz oscillators in Fig. 12 (solid). Agreement with previous data (dashed, dash-dotted) is good,[14, 28] but our data cover a much broader spectral range. By extrapolating the dielectric constant towards zero energy (but subtracting the IR pole due to lattice absorption), we find the electronic contribution to the dielectric constant to be ϵ_∞=4.0. (This is also known as the high-frequency dielectric constant, for frequencies much higher than those of lattice vibrations.)

To estimate the lowest direct band gap, we plot α^2 (determined from the ellipsometry data) versus photon energy in Fig. 13. An extrapolation to zero yields a direct band gap of 5.8$\pm$0.1 eV, as shown by the dashed line. This direct band gap is significantly larger than the onset of absorption (between 4.6 and 4.8 eV, see Fig. 9) and the Tauc gap (4.9 to 5.0 eV, see Table 1).

The onset of absorption is more clearly seen by plotting α on a semi-logarithmic scale, shown by the inset in Fig. 13. The symbols show α determined from a wavelength-by-wavelength fit using a fixed surface layer thickness of 19.1 Å. We note that transmission measurements show α=60 cm^{-1} at 4.7 eV (see Fig. 9), while our ellipsometry measurements find $\alpha\sim$500 cm^{-1}. We add our usual warning that our ellipsometry setup is unable to determine α below 10^3 cm^{-1}. Smaller values of α are better measured in transmission.

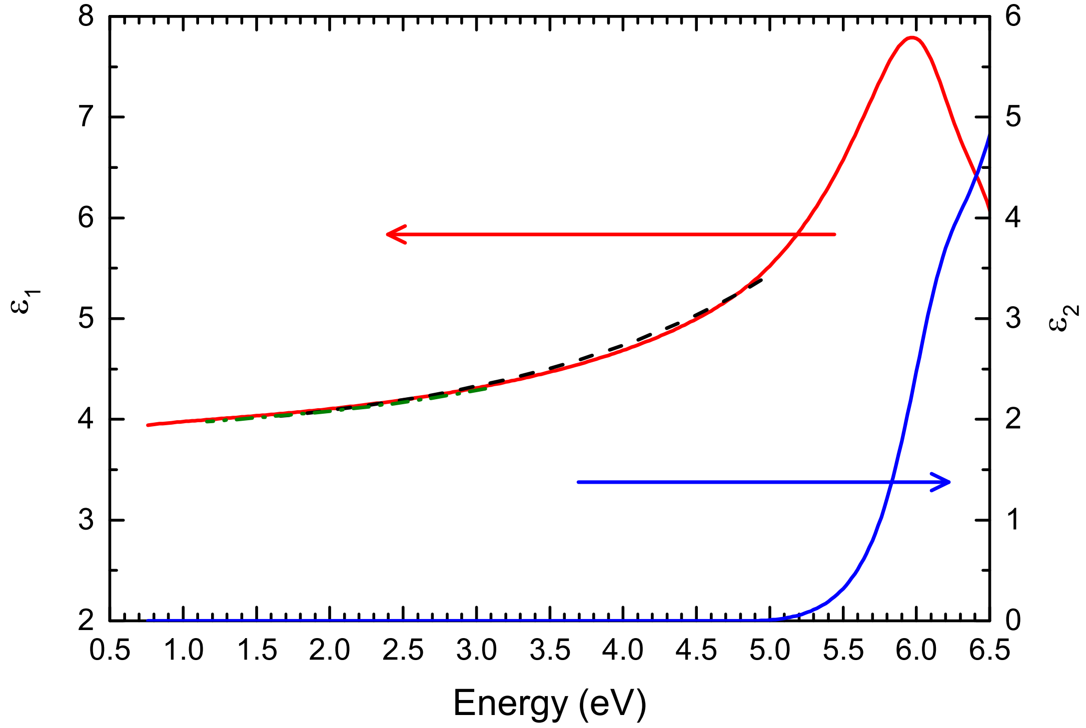

Figure 12: Real and imaginary part of the dielectric function ϵ of LSAT at 300 K described with two Tauc-Lorentz oscillators and two poles (solid), calculated using the parameters in Table 1. Data calculated from the Sellmeier parameters listed in Ref. [14] (dashed) and Ref. [28] (dot-dashed) are shown for comparison.

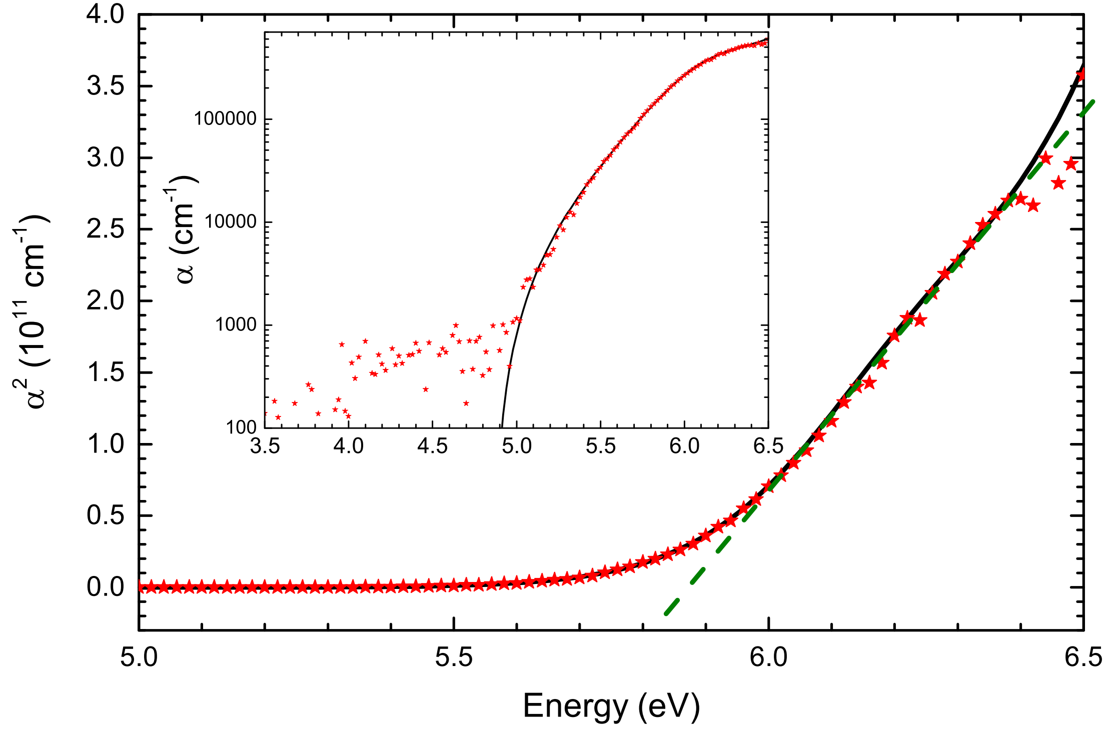

Figure 13: The square of the absorption coefficient of LSAT versus photon energy at 300 K can be extrapolated to yield a direct band gap of 5.8±0.1 eV, as shown by the dashed line. Symbols were determined by direct inversion of the ellipsometric angles (wavelength-by-wavelength fit), while the solid line shows the result of the Tauc-Lorentz model. The inset shows α on a logarithmic scale.

3.4 Far-IR, Mid-IR, and Raman Results

Our two-side polished LSAT wafer with 0.5 mm thickness is completely opaque in far-infrared FTIR transmission measurements from 70 to 1090 cm^{-1}, indicating strong lattice absorption. Raman spectra for LSAT (100) at 300 K are shown in Fig. 14. These LSAT spectra are similar to those reported in Ref. [23]. As in the ordered double perovskite[36, 37] compound Sr_2AlTaO_3, four strong peaks are seen at 152 cm^{-1} (T_{2g}), 471 cm^{-1} (T_{2g}), 599 cm^{-1} (E_g), and 883 cm^{-1} (A_{1g}). Weaker peaks appear at 195, 425, and 735 cm^{-1}.

Fourier-transform infrared (FTIR) ellipsometry was used to investigate the lattice vibrations of LSAT at 300 K. The ellipsometric angles from 250 to 1400 cm^{-1} for incidence angles ϕ from 65° to 75° are shown in Fig. 15. We also include far-infrared ellipsometry data from 80 to 650 cm^{-1} at ϕ=75° published previously.[30] Only normal dispersion is found at larger energies. At 0.8 eV, the data merge seamlessly with those shown in Fig. 10. The same data are also shown as a pseudo-dielectric function in Fig. 16 and as a loss function in Fig. 17. Since surface roughness contributes negligibly in the far- and mid-IR, we do not distinguish between ϵ and $\langle\epsilon\rangle$ in this spectral range.

Infrared-active transverse optical (TO) phonons at the center of the Brillouin zone cause peaks in ϵ_2 due to infrared lattice absorption. For an ideal perovskite ABO_3, there are three IR active modes with T_{1u} symmetry. A fourth IR-active

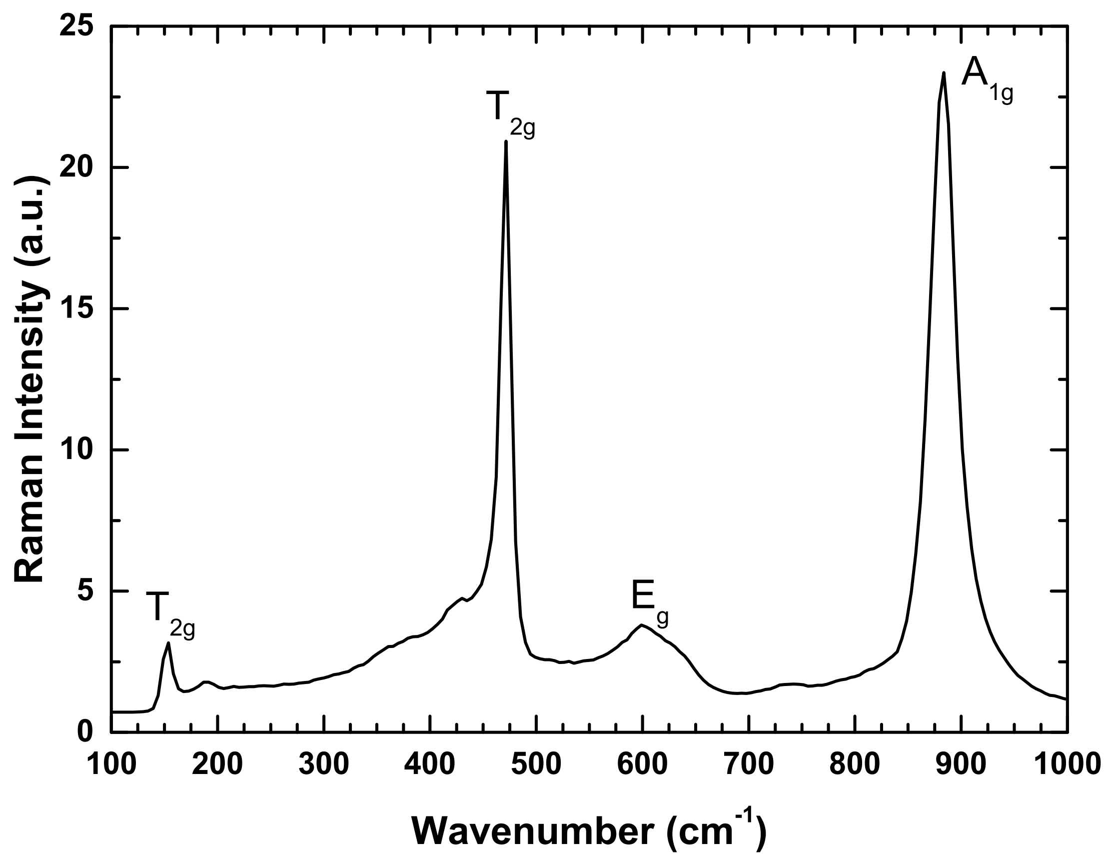

Figure 14: Raman spectra for LSAT (100) at 300 K show four strong peaks, similar to Sr_2AlTaO_6. Symmetry assignments for the vibrations were taken from the literature.[23, 37]

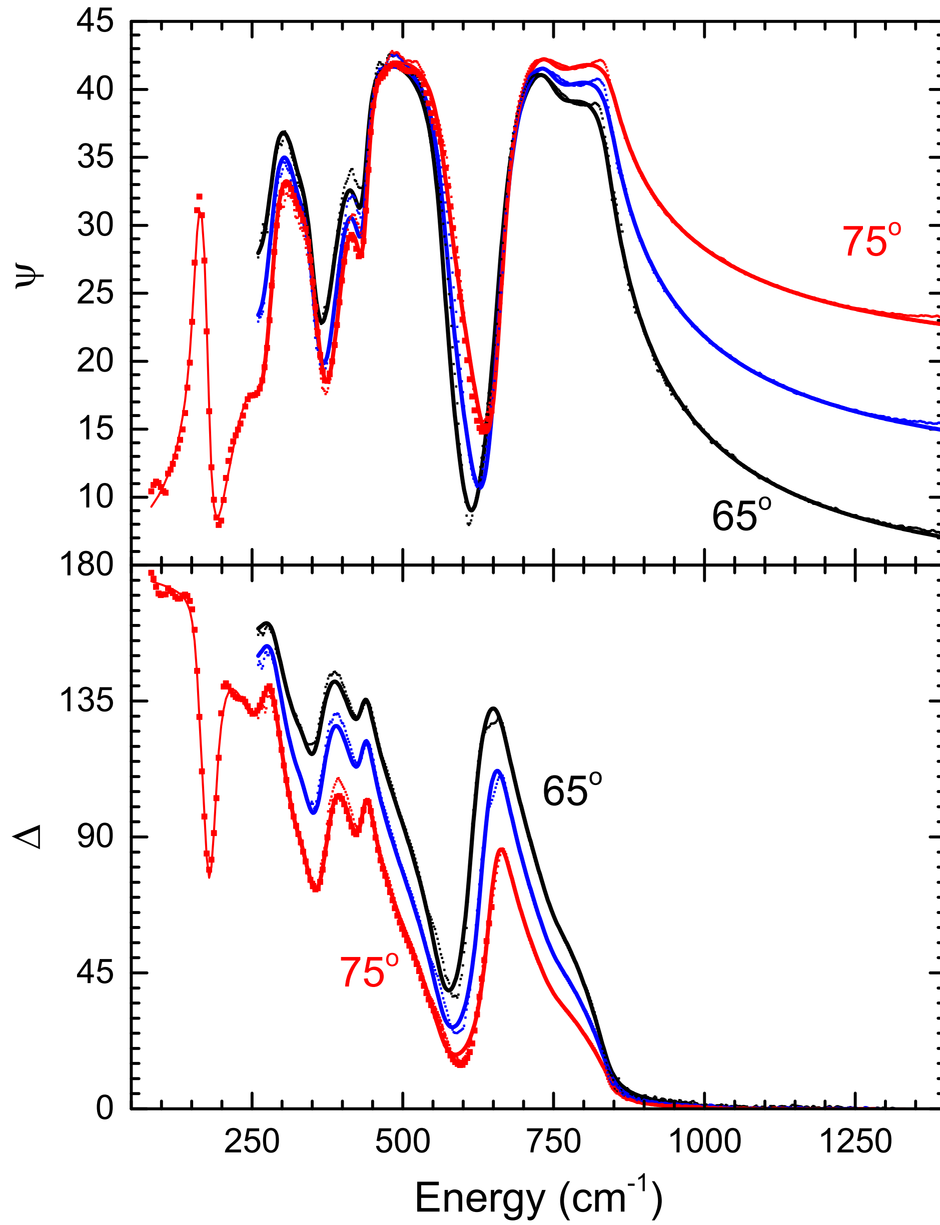

Figure 15: Ellipsometric angles ψ and Δ for LSAT at 300 K in the region of lattice absorption (symbols) for three angles of incidence (65° to 75°) in comparison with a fit to a factorized model with nine TO/LO phonon pairs (solid).

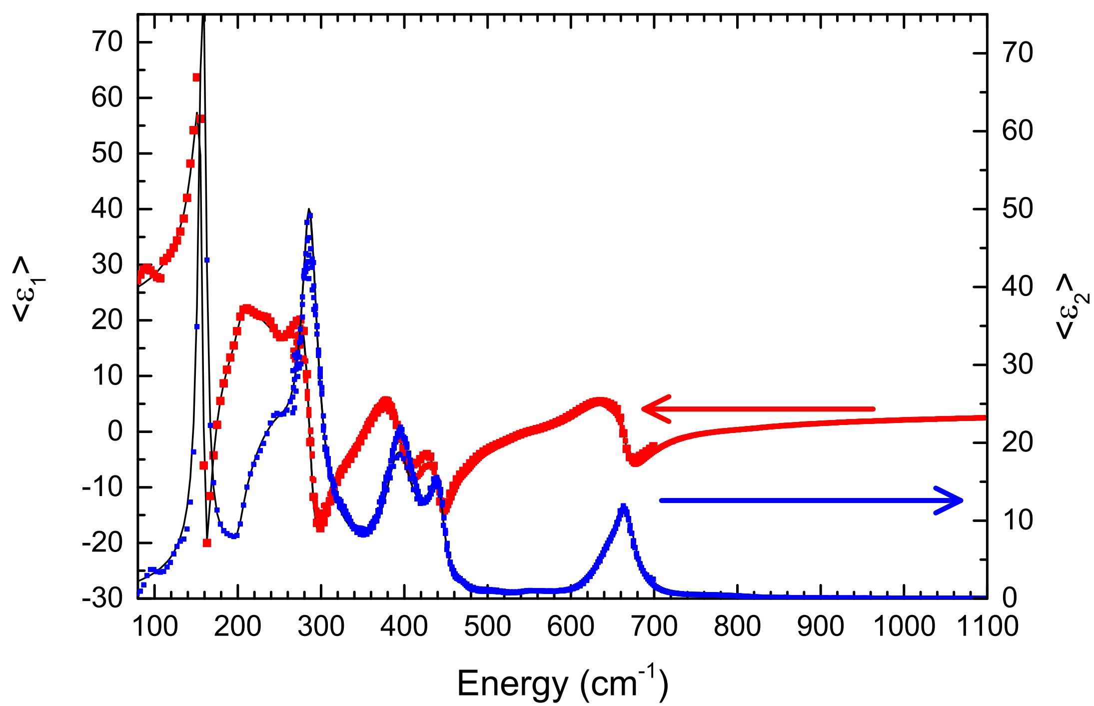

Figure 16: Same data as in Fig. 15, but shown as a pseudodielectric function.

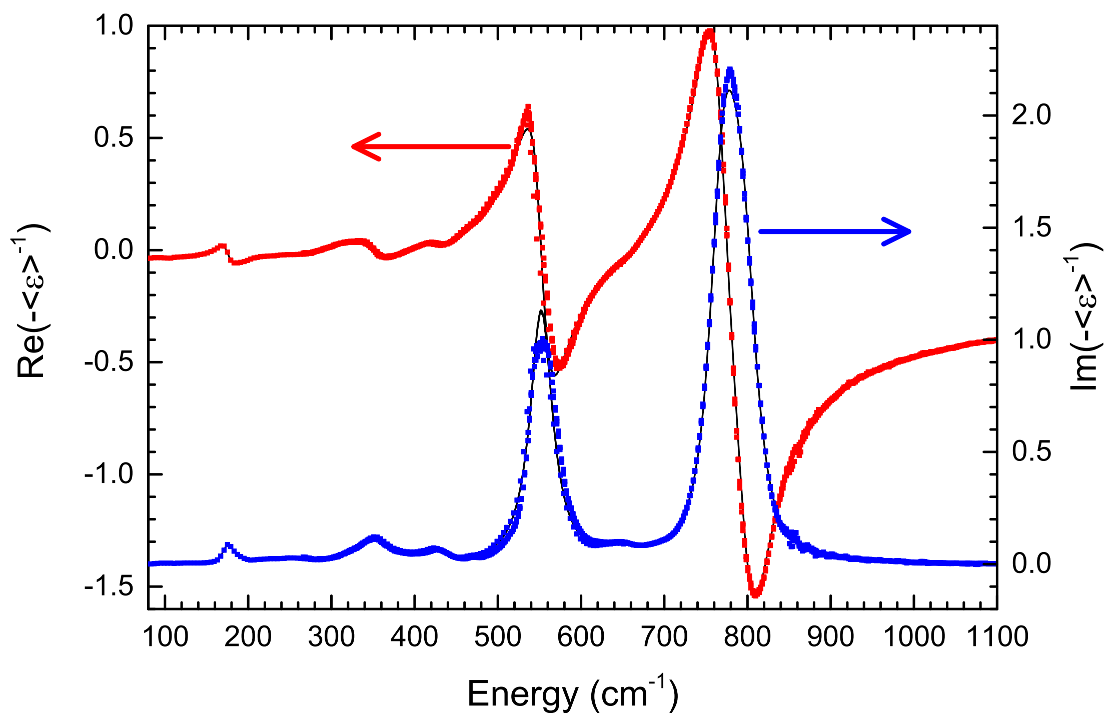

Figure 17: Same data as in Fig. 15, but shown as a pseudo-loss function $-1/\langle\epsilon\rangle$.

mode appears due to ordering at the Al/Ta sites, as in the double perovskite compound Sr_2AlTaO_3.[23] Additional modes are expected for random alloys, such as $Si_{1-x}Ge_x$,[38] or due to two-phonon absorption.[97]

Since $(La_{0.3}Sr_{0.7})(Al_{0.65}Ta_{0.35})O_3$ has random occupation at both the A and B sites, we might expect up to twelve phonon modes, because each combination of La/Al, Sr/Al, La/Ta, and Sr/Ta might be associated with three T_{1u} phonons in the disordered perovskite phase. We find experimentally that only the La/Sr disorder contributes an additional strong phonon, for a total of five strong IR-active phonons, which appear as ϵ_2 peaks in Fig. 16. They are located approximately at 158, 286, 392, 442, and 666 cm^{-1}. Two weaker peaks exist between 220 and 250 cm^{-1} and another one at 330 cm^{-1}. A ninth phonon is needed to describe the dip in the ψ reststrahlen band near 790 cm^{-1}. In analogy to LiF and NiO, we assign this peak to two-phonon absorption.[97]

Describing ϵ as a sum of Lorentzians[31] allows us to estimate the energies, amplitudes, and broadenings of all nine TO phonons. Adding all amplitudes to the high-frequency dielectric constant ϵ_∞=4.0 (see above), we find ϵ_s=22.2±0.7 for the static dielectric constant, in excellent agreement with the literature.[39, 40] Lorentz parameters for all phonons are shown in Table 2. While an expansion of the dielectric function into such a large number of Lorentzians may seem somewhat arbitrary, we confirmed with far-IR measurements of LSAT at 10 K, that all Lorentzians used in our expansion are associated with peaks in ϵ_2.

Describing infrared ellipsometry data with a sum of Lorentzians is expected to yield good agreement, if the individual TO phonons are well separated. For LSAT, the broadenings are larger than the phonon separations for some modes and therefore the agreement of the Lorentz model to the dielectric function is not perfect, just like for other materials such as $LaAlO_3$, LiF, or NiO.[31, 97] The rms deviation between data and model is about $5-10$ times larger than the experimental errors. Nevertheless, this model is instructive, because it quickly yields phonon energies and amplitudes.

To improve our model, we write ϵ as a product of Lyddane-Sachs-Teller (LST) factors.[31] As a starting point for our fit, we use the TO energies in Table 2 and the LO energies found from the peaks in loss function in Fig. 17, i.e., 180, 350, 430, 550, and 780 cm^{-1}. The highest energy phonon has an asymmetric ϵ_2 lineshape. We therefore add a sixth TO/LO phonon pair to our model. The need for this phonon is also obvious from the inspection of the ψ reststrahlen band, which has a minimum near 770 cm^{-1}, demonstrating the presence of another phonon. Another three weak or broad TO/LO phonon pairs (7-9) are added to improve the fit for asymmetric peaks. A model with nine LST factors and the parameters shown in Table 2 gives very good agreement with the experiment, with the average rms deviation only six times larger than the experimental errors. We find one non-physical LST factor with switched LO and TO energies, which is needed to describe the line shape around 200 cm^{-1}. Our results are in qualititative

agreement with FTIR transmission measurements on LSAT crystals,[23] where five TO phonons were found at energies similar to ours. We would like to note that there is sample to sample variations in phonon amplitudes that are dependant upon sample source and annealing treatment before measurement.

The phonon amplitudes can also be calculated from the factorized phonon model with[41]

$$A_j \;=\; \epsilon_\infty \frac{E^2_{j\mathrm{LO}} - E^2_{j\mathrm{TO}}}{E^2_{j\mathrm{TO}}} \prod_{k\neq j} \frac{E^2_{k\mathrm{LO}} - E^2_{j\mathrm{TO}}}{E^2_{k\mathrm{TO}} - E^2_{j\mathrm{TO}}}, \tag{19}$$

where the indices j and k label the TO/LO phonon pairs. Results listed in Table 2 shows good agreement between the Lorentz and LST amplitudes for some modes and significant differences for others. Most importantly, the amplitude for the inverted TO/LO pair[44] at 202/199 cm^{-1} is negative. The high frequency dielectric constant is found to be $\epsilon_\infty = 3.96$, using this and the calculated phonon amplitudes, the static dielectric constant as calculated by our LST model is found to be approximately 23.25, which is still in good agreement with the experimental value.

Since only three TO phonon modes are expected for a perfect cubic perovskite ABO_3 and four modes for the (ordered) double perovskite Sr_2AlTaO_6,[23] we conclude that several of the phonons found in our model must be due to alloy disorder. The broad phonon at 765 cm^{-1} might be due to two-phonon absorption.

We assign our observed LSAT frequencies based on vibrational modes[42, 43, 44] identified for cubic $LaAlO_3$: The lowest-energy modes (1-2) are vibrations of

Table 2: Parameters for TO and LO phonons from FTIR ellipsometry: Energy E, amplitude A, and broadening Γ. The top portion shows the parameters for nine Lorentz oscillators. The bottom portion describes ϵ with a product of nine LST factors for TO/LO phonon pairs. The LST amplitudes were calculated from Eq. (19).

No.	A (cm^{-1})	E_{TO}	Γ_{TO} (cm^{-1})	E_{LO} (cm^{-1})	Γ_{LO} (cm^{-1})	assignment
L1	6.30(4)	156.9(1)	12.8(3)			
L2	1.5(4)	222(2)	35(3)			
L3	2.6(5)	248(1)	42(6)			
L4	4.3(2)	285.9(3)	28(1)			
L5	0.46(8)	330(2)	46(6)			
L6	1.89(4)	395.0(2)	44(1)			
L7	0.51(2)	436.4(2)	18.6(7)			
L8	0.646(2)	659.8(1)	36.5(3)			
L9	0.0045(6)	787(1)	26(4)			
1	5.58	158.1(1)	10.7(2)	174.1(1)	14.7(2)	La-BO_6
2	2.35	286.3(2)	22.8(5)	355.5(3)	50.6(6)	Sr-BO_6
3	1.56	392.3(3)	40.5(5)	432.0(5)	43(1)	B-O bend
4	0.43	442.1(2)	22.4(4)	552.5(2)	33.1(4)	B-O bend
5	0.11	632(1)	46(2)	638(2)	58(3)	B-O stretch
6	0.49	666.2(3)	32.4(5)	766.8(8)	45.7(2)	B-O stretch
7	0.01	789(2)	74(5)	800(1)	48(2)	two-phonon
8	−0.74	201.7(5)	23(1)	199(1)	23(1)	
9	9.50	251(1)	115(3)	277(1)	57(2)	

the $(Al/Ta)O_6$ octahedra against the La/Sr sublattice. The La-AlO_6 vibration in $LaAlO_3$ has an energy of 190 cm^{-1}, which should be reduced by substituting Al with Ta. Also, the Sr-AlO_6 vibration should have a higher energy and therefore is identified with mode (2). Because of their large mass, it is not likely that the La/Sr sublattice participates in any of the modes at higher energies.[44] Similarly, the highest energy strong mode (5) at 666 cm^{-1} is an (Al/Ta)-O stretching mode, with the La/Sr sublattice immobile. The two intermediate modes (3-4) are (Al/Ta)-O bending modes. This mode is doubled because of ordering of the Al/Ta sublattice. The additional weak modes (7-9) are due to defects and disorder.

3.5 Summary

We have used spectroscopic ellipsometry, FTIR ellipsometry, and Raman spectroscopy to characterize the electronic and vibrational properties of LSAT from 0.01 to 6.5 eV. X-ray diffraction confirms the partially ordered cubic crystal stucture and the presence of ordered domains in the sample on the order of 15 nm in diameter. An oscillator model, with either one or two Tauc-Lorentz oscillators, was used to describe the interband transition in our spectra. Ellipsometry and transmission data see the direct band gap at 5.8 eV with an Urbach tail below giving an onset of absorption at approximately 4.9 eV. The vibrational spectra was modeled using a nine factor Lyddane-Sachs-Teller model where one factor shows a non-physical switch in LO and TO positions with a negative amplitude,

but was necessary to describe the line shape.

Acknowledgments

This work was supported by the National Science Foundation (DMR-1104934 and DMR-1505172) and by the Army Research Office (W911NF-14-1-0072). The infrared ellipsometry measurements were carried out at the Center for Integrated Nanotechnologies, an Office of Science User Facility operated for the U.S. Department of Energy (DOE) Office of Science by Los Alamos National Laboratory (Contract DE-AC52-06NA25396) and Sandia National Laboratories (Contract DE-AC04-94AL85000). The work at the University of Fribourg was supported by the Schweizerische Nationalfonds (SNF) through grant No. 200020-153660.

4 OPTICAL CONSTANTS OF GERMANIUM AND THERMALLY GROWN GERMANIUM DIOXIDE FROM 0.5 TO 6.6 eV VIA A MULTI-SAMPLE ELLIPSOMETRY INVESTIGATION

This chapter is the original submission to JVST B prior to editing after review. It will be possible to find the final paper under the same name.

T. Nathan Nunley, Nalin S. Fernando, Nuwanjula Samarasingha,

Jaime M. Moya, Cayla M. Nelson, Amber A. Medina, Stefan Zollner

Department of Physics, New Mexico State University, MSC 3D, P.O. Box 30001, Las Cruces, NM 88003-8001

Abstract

Thermal GeO_2 oxides up to 136 nm thickness were produced by annealing Ge wafers in pure oxygen at 550°C and 270 kPa pressure for up to ten hours. The oxidation kinetics followed the Deal-Grove Law. Using multi-sample spectroscopic ellipsometry of a series of five thermal oxides with different thicknesses, the complex dielectric functions of Ge and GeO_2 were determined from 0.5 to 6.6 eV, for thin-film metrology applications in Ge-based microelectronics and photonics. The dispersion of the GeO_2 layer was modeled with a simple Tauc-Lorentz oscillator, but a more complicated dispersion with eight parametric oscillators was required for Ge. A reasonable fit to the ellipsometric angles could be obtained by assuming that all thermal oxides can be described by the same dielectric function, regard-

less of thickness, but a slight improvement was achieved with a lower density near the surface. We compare our results with literature data for Ge and bulk and thin-film GeO_2.

4.1 Introduction

Optical constants (complex refractive index n, complex dielectric function ϵ, reflection and absorption coefficients R and α) of materials are of great importance for optical metrology in the semiconductor industry.[45, 46] A high-performance complementary-metal-oxide-semiconductor (CMOS) process flow with eleven layers of metal requires about 75 photolayers and may contain up to 100 thickness measurements, most of them performed using spectroscopic ellipsometry.[47] This technique has been described in various books with increasing levels of sophistication.[24, 9, 25, 26]

Since most microelectronic devices are built on a Si wafer, the optical constants of Si and SiO_2 are the most important ones and have been determined with greater accuracy than other materials.[48] They are often referred to as *Woollam silicon* and used almost universally for thickness measurements in factories around the world. For many materials, optical constants have been tabulated by Palik[107] and Adachi.[50] Optical constants of intrinsic materials are related to their vibrational and electronic properties.[3, 51, 52, 53, 54]

Optical constants are determined using different techniques: Below[55] or

near[56, 57] the band gap of a semiconductor, the absorption coefficient α and refractive index n are determined using transmission and minimum-deviation prism[58] measurements, respectively. These techniques (and data resulting from them) are still the most useful even today and have not been replaced by more modern methods, such as spectroscopic ellipsometry, which is not suitable for measuring small absorption coefficients below 10^3 cm^{-1}. Above the band gap, transmission measurements on thin films can be successful.[59] Since about 1960, the complex dielectric function above the band gap has been determined by reflectance followed by Kramers-Kronig transformation,[60] but such results are often plagued by systematic errors due to surface overlayers (including surface roughness) and the limited spectral range of the measurement.

More recently, the optical constants of semiconductors have been determined by spectroscopic ellipsometry. Early instrument designs suffered from the rotating-analyzer artifact[61, 62] and could not measure small absorption coefficients accurately. This accuracy was improved by instruments employing a polarization modulator[63] or a computer-controller Berek waveplate compensator.[48] Even the most precise spectroscopic ellipsometers are unable to compete with transmission or minimum-deviation prism measurements to determine the optical constants below the band gap. We note that transmission measurements must be performed using two-side polished wafers, while ellipsometry measurements are better taken on single-side polished wafers, because reflections from a polished

(or insufficiently roughened) back surface interact incoherently with the reflection from the front surface, thus causing depolarization of the reflected light beam.[9]

Ellipsometry measurements on bulk semiconductors are difficult to interpret, because semiconductor wafers are usually covered by native oxides and have a slightly rough surface. Modeling ellipsometry data from a real semiconductor surface requires precise knowledge of the optical constants of the substrate (for example, Ge), the surface layer (native oxide and roughness), and the thickness of the surface layer. There are too many unknowns in the model to determine all of them in measurements of a single sample.

Aspnes and Studna[61] addressed this problem for Ge by minimizing the surface layer thickness with wet chemical etching (using a bromine solution in methanol, buffered hydrofluoric acid, followed by a water rinse) and thus optimizing the height of the absorption near the E_2 critical point at 4.26 eV. They achieved an $\hat{\epsilon}_2$ peak value of 30.6 at 4.26 eV, which is still only a lower bound for the true value of ϵ_2 for Ge at this energy. Cleaving a bulk Ge crystal in UHV[64] or cleaning the surface through ion bombardment[65] followed by annealing to produce clean 2×8 or 2×1 reconstructed surfaces also introduces uncertainties because of the distortion of the polarization state by windows[9] and because of surface roughness, ion bombardment damage, and epioptical effects, which make the optical constants dependent on surface orientation[66] or surface passivation.

A different approach was taken by Jellison,[63] whose intent of wafer cleaning

was to remove carbon-based surface contamination (with acetone, methanol, and peroxide, followed by a water rinse), but not the surface oxide itself. The thickness of the remaining stable native oxide was then determined with an ellipsometric measurement below the direct band gap, where the absorption of Ge is small. This is known as the Jellison-Sales method for transparent glasses.[67] It works well, if the optical constants of the surface overlayer are known precisely, but fails otherwise. Jellison found an $\hat{\epsilon}_2$ peak value of 31.8 at 4.24 eV, slightly higher than the result from Aspnes and Studna[61] because of the native oxide layer correction.

Finally, Herzinger *et al.*[48] describe a method to determine the optical constants of semiconductors, if neither the optical constants of the substrate nor those of the oxide overlayer nor the layer thickness are known. This method requires a series of samples consisting of the same substrate and the same oxide, where only the oxide thickness is varied. Ellipsometry measurements of several such samples with oxide thicknesses ranging from very thin (only native oxide) to as thick as possible (limited by the rate of oxidation) yield the optical constants of the substrate, those of the oxide, and the thicknesses of all layers. The only assumption used by this method is that the optical constants of the oxide do not vary with thickness (or from one sample to another). The validity of this assumption can be checked by inspecting the goodness of fit for all samples.

This method has only been used for Si so far,[48] where uniform and repeatable thermal oxides with arbitrary thicknesses are easily produced with well established

silicon manufacturing techniques.[68] It has led to universally accepted values for the optical constants of Si (100) and its thermal oxide.[48] The purpose of this paper is to use the same method to determine the optical constants of bulk Ge with a (100) surface orientation and those of thermally grown GeO_2. Precise knowledge of Ge optical constants is important for the development of Ge-based p-type metal-oxide-semiconductor (PMOS) devices, which have attracted much attention recently.[69] The optical constants of thin Ge layers may, of course, be different from those of bulk Ge, but that is beyond the scope of this article.

This article is organized as follows: We first describe our experimental methods to clean the Ge substrate, prepare thermal GeO_2 oxides, and ellipsometry data acquisition and analysis. Next, we present our results for GeO_2 on Ge in a three-phase (ambient/oxide/substrate) model, followed by a discussion if this model can be improved by including a thin interfacial layer between the GeO_2 and the substrate or by allowing the GeO_2 refractive index to vary between samples. Finally, we discuss our overall results and compare our findings to previous data.

4.2 Thermal oxidation of Ge

As-received Ge bulk wafers were cleaved into 20×20 mm^2 pieces. These pieces were then subjected to an ozone clean in a Novascan PSD Pro series digital UV ozone system utilizing a Hg vapor lamp. This clean was performed in an oxygen-enriched environment, achieved by allowing ultrapure oxygen to flow through the

system for several minutes before sealing the chamber with the Hg lamp on and the sample on a heating stage held at 150°C, followed by a 30-minute period of incubation with the lamp off and the sample cooling to room temperature. After this ozone clean, samples were cleaned ultrasonically for 20 min in deionized water, followed by 20 min in isopropanol.

The intent of this hybrid dry/wet clean is to remove carbon-containing surface contaminants from the wafer and reduce the native oxide thickness, but leaving a thin stable oxide on the wafer[63] as a seed oxide for thermal oxidation. Unlike Ref. [70], we did not use harsh chemicals (bromine or hydrofluoric acid) before oxidation to avoid roughening or contaminating the surface. Some elements of our clean, especially the use of reactive oxygen species, are similar to those of Ref. [71].

After cleaning, the samples were placed in an ULVAC-RIKO MILA-5000 infrared lamp heating system for rapid thermal annealing. Samples were annealed in ultrapure oxygen with 170 kPa gauge pressure (270 kPa absolute), as measured by the gas regulator, at 1 L/min flow at 550°C for several hours, as needed to achieve the desired oxide thickness.[70] Table 3 lists the annealing times for several samples as well as their thicknesses and other parameters.

GeO_2 is hygroscopic and water soluble.[72] Therefore, ellipsometry measurements were performed within a few days after oxidation. Furthermore, thermal GeO_2 desorbs by reaction with the Ge substrate and diffusion of oxygen vacancies

generated at the Ge/GeO_2 interface.[73] Higher oxidation temperatures and lower oxygen pressures promote GeO_2 desorption. We selected an oxidation temperature of 550°C, because it allows a suitable thermal oxide growth rate with minimal oxide desorption and lowest interface trap density.[74] The oxidation pressure of 2.7 atm also enhances oxidation and suppresses thermal oxide desorption, compared to atmospheric pressure.[72]

The resulting GeO_2/Ge layers were brown in appearance, with reasonably uniform thickness and occasional spots. Optimizing the clean was crucial to the success of our annealing experiments. We found that thermal oxidation (see Table 3 and Fig. 18) follows the Deal-Grove model[68]

$$d^2 + Ad = B\,(t + \tau)\,, \tag{20}$$

where d is the oxide thickness (determined from ellipsometry as described below), t the oxidation time, and A, B, and τ are parameters that depend on the oxidation conditions, such as temperature, pressure, and gas composition. As shown by the dashed lines in Fig. 18, the oxide thickness depends nearly quadratically on oxidation time, i.e., $d^2 \approx B\,(t + \tau)$. Including the linear term Ad (solid line) becomes important for thinner oxides and higher pressures. The oxidation is much faster at higher pressure.

We characterized our layers using grazing-incidence x-ray reflectance (XRR) as shown in Fig. 19. These XRR spectra show a double critical angle for the

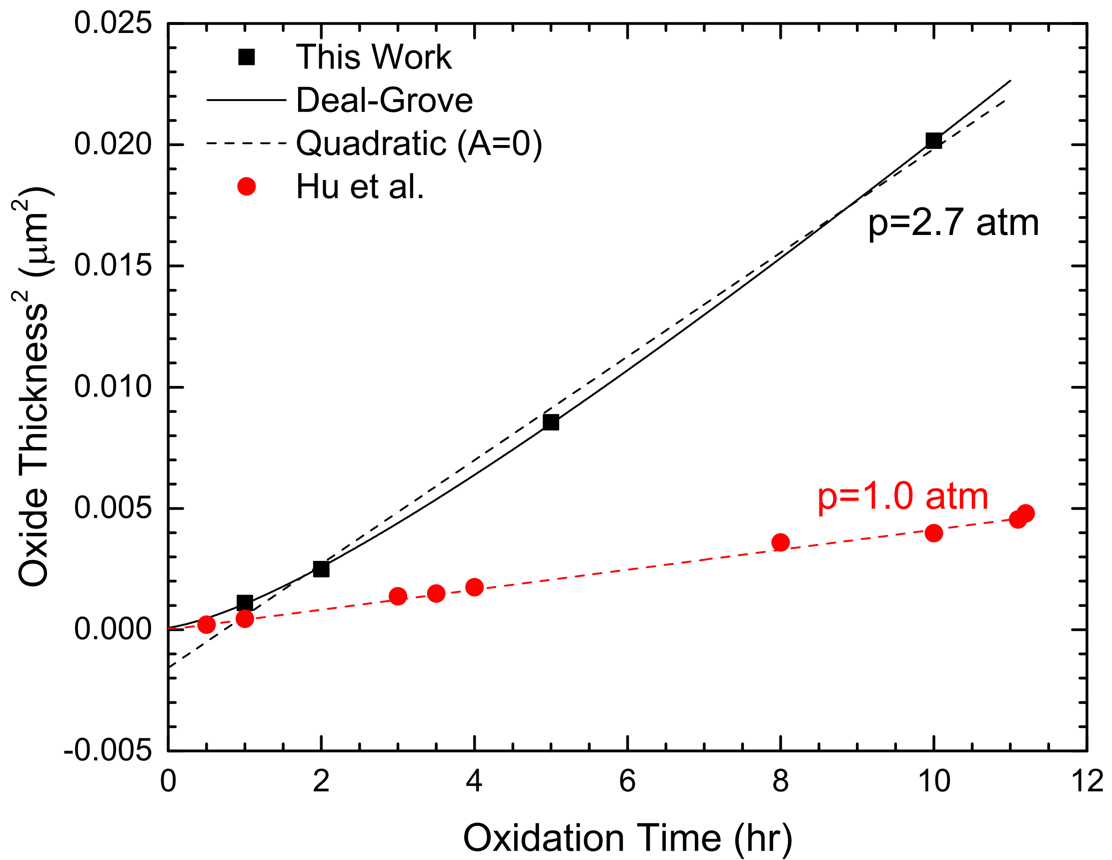

Figure 18: Thermal oxide thickness versus oxidation time at atmospheric pressure (Ref. [70]) and at 2.7 atm (this work). The solid line shows the best fit to Eq. (20), while the dashed lines assume a quadratic dependence of the thickness on oxidation time (A=0).

Ge substrate (1.35 e/Å^3 density) and the GeO_2 layer with a lower density (1.03 eV/Å^3). Clear interference fringes (if present) indicate uniform oxide layers with a well-defined electron density. As shown in Fig. 19, we could only find such fringes for the thinner oxide layers, where XRR thickness and ellipsometry thickness agree to within 1 nm (which could be explained with surface roughness). From fitting the XRR spectra for thinner oxides, we are able to determine the electron density as a function of depth, also shown in Fig. 19. Thicker oxide layers do not show interference fringes, perhaps due to thickness non-uniformity or a density gradient in the oxide.

Symmetric ω-2θ powder x-ray diffraction scans on a sealed-tube instrument with 1.8 kW power are similar for all samples and only show background and the $2\times$Ge(002) and Ge (004) substrate peaks. We did not find the amorphous GeO_2 diffraction peak at 2θ=25° seen on rf sputtered GeO_2 films,[75] which were up to 100 times thicker than our thermally grown oxides.

4.3 Ellipsometry measurements and data analysis

We acquired the ellipsometric angles ψ and Δ and the depolarization spectra from 0.5 to 6.6 eV with 0.01 eV steps on a J.A. Woollam vertical variable-angle-of-incidence rotating-analyzer ellipsometer with a computer-controlled Berek wave-plate compensator.[76] To reduce experimental errors, all data were obtained by averaging two-zone measurements with equal and opposite polarizer angles. Data

Table 3: List of GeO_2 oxides produced by thermal oxidation of Ge substrates at 2.7 atm oxygen pressure at 550°C. d is the oxide thickness from ellipsometry, t the oxidation time, Δd the relative thickness non-uniformity determined from the ellipsometry depolarization spectra, d_{XRR} the thickness as determined by x-ray reflectance (XRR) (samples 4 and 5 were fit with a fixed thickness), and $<\rho>_{\mathrm{XRR}}$ the electron density determined by XRR.

No.	t	d	Δd	d_{XRR}	$<\rho>_{\mathrm{XRR}}$
	(hr)	(nm)	(%)	(nm)	(e/Å^3)
1	0	2.3	NA	NA	NA
2	1	34.0	6%	33.3	1.03
3	2	52.2	6%	50.2	1.03
4	5	88.6	7%	92.5(f)	1.00
5	10	135.9	1%	142(f)	1.01

Table 4: Deal-Grove parameters A, B, and τ from Eq. (20) for thermal oxidation of Ge in pure O_2 at temperature T and pressure p.

T	p	A	B	τ	
(°C)	(kPa)	(nm)	(nm^2/hr)	(hr)	
550	100	0	432	0	From Ref. [70]
550	270	97	3300	0.28	this work

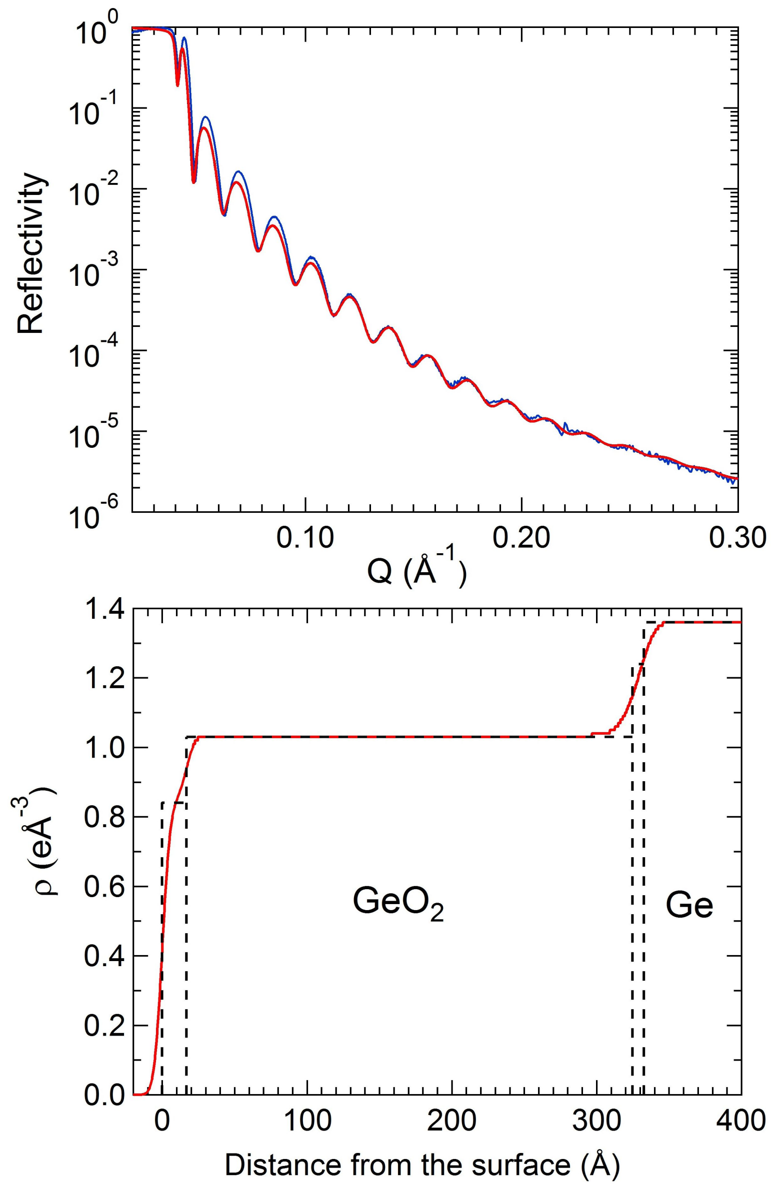

Figure 19: Grazing-incidence x-ray reflectance spectrum (red: model; blue: data) and electron density versus depth for sample 2 (33 nm thickness).

were acquired for four angles of incidence (ϕ_0=60°, 65°, 70°, and 75°). Larger incidence angles would be desirable to have data near the Brewster regime for bulk Ge, but such measurements are not practical because of the finite sample size and nonuniform oxide thickness. The magnitude of the polarizer angle was kept equal to ψ, but no less than 5°. The time needed to acquire data for one sample was several hours.

Monochromatic light was produced by an HS-190 double monochromator equipped with three sets of gratings for the near-infrared (NIR), visible (VIS), and quartz-ultraviolet (QUV) portion of the spectral range. The linear dispersion of the monochromator is 2.3 nm/mm in the VIS/QUV and 4.6 nm/mm in the NIR, leading to spectral bandwidths of no more than 4 and 8 nm, respectively, for a maximum slit width of 1.7 mm.

For the spectral range from 0.76 to 6.6 eV, we used a UV-enhanced optical fiber and a 75 W Xe short-arc lamp (Hamamatsu L10873) to produce the incident monochromatic beam. We also measured from 0.5 to 3.0 eV using an IR-enhanced optical fiber and a 100 W quartz-tungsten-halogen lamp (Ushio, with a TDK-Lambda ZUP20-20 power supply), also mounted on the HS-190 monochromator using a slightly modified reflector insert capable of holding and powering the tungsten lamp. This IR setup slightly extends the spectral range downward to 0.5 eV and avoids the strong peaks of the Xe lamp and the opaque region of the UV fiber from 0.88 to 0.92 eV. Data obtained with both setups were merged and

showed good agreement in the region of spectral overlap. As one might expect, only the Ge wafer with the thinnest (native) oxide layer showed a slightly unstable oxide due to ongoing oxidation.

The ellipsometric angles (ψ and Δ) and the Fresnel reflectance ratio $\rho = e^{i\Delta} \tan\psi$ are related to the pseudo-refractive index $\hat{n}$ and the pseudo-dielectric function $\hat{\epsilon} = \hat{n}^2$ of the sample through[24, 9]

$$\rho = \frac{(\hat{n}\cos\phi_0 - \cos\phi_1)(\cos\phi_0 + \hat{n}\cos\phi_1)}{(\hat{n}\cos\phi_0 + \cos\phi_1)(\cos\phi_0 - \hat{n}\cos\phi_1)}, \quad (21)$$

where ϕ_0 is the angle of incidence and ϕ_1 the angle of refraction. For an ideal sample without surface overlayers, $\hat{n}$ and $\hat{\epsilon}$ are equal to the refractive index n and the dielectric function $\epsilon = n^2$. The ellipsometric angles for a sample consisting of one or more layers on a substrate can be calculated if the optical constants for all materials are known (or assumed to follow a model).[24, 9, 26]

The complex dielectric function ϵ for an amorphous oxide like thermally grown GeO_2 is usually described by the Tauc-Lorentz model, where the imaginary part of ϵ as a function of photon energy E is given by[9, 25, 77]

$$\epsilon_2(E) = \frac{AE_0\Gamma(E - E_g)^2}{E\left[\left(E^2 - E_0^2\right)^2 + \Gamma^2 E^2\right]} \quad (22)$$

for $E > E_g$ and vanishes below E_g. The real part is obtained by Kramers-Kronig transform. This model contains the following parameters: E_g is the Tauc gap, the onset of absorption. The Lorentz oscillator[78] resonance energy is E_0, its amplitude A, and its broadening Γ.

In addition, we use two poles[24] (unbroadened Lorentz oscillators)

$$\epsilon(E) = \frac{A}{E_0^2 - E^2} \tag{23}$$

(where the resonance energies are often chosen arbitrarily as 0.01 and 11 eV) to describe the influence of absorption peaks below or above our spectral range on the dispersion. For crystalline, tetragonal (rutile) GeO_2, the dominant transverse optical phonon modes for the ordinary (E_u) and extraordinary (A_{2u}) beams have energies of 41 and 65 meV, respectively.[79] Glassy germania[80, 81] also has a significantly higher IR absorption band located at 111 meV. Therefore, placing an IR pole at 0.05 eV is reasonable.

Finding a parametric model for semiconductors like Ge with a finite number of adjustable parameters requires some thought. In principle, the analytical properties of the complex dielectric function imply that it can be written as a product defined by its poles and zeroes in the complex plane, which can be approximated as a sum of Lorentzians. Seven Lorentzians[82] are sufficient to fit ϵ for GaAs between 1.5 and 5.0 eV, but more terms are needed outside of this range. More flexibility can be introduced by allowing Lorentzians with a complex amplitude.[78]

A different approach was taken by Aspnes,[83] who calculated the absorption of semiconductors assuming parabolic bands and constant dipole matrix elements. This critical-point parabolic-band model gives a good description of the derivatives

of the dielectric function, but fails to describe ϵ away from the critical point singularities, where the nonparabolicity and the $\vec{k}$-dependence of the dipole matrix element have to be taken into account.[84]

More general models for ϵ can be constructed from the superposition of critical point structures, which are composed of continuous polynomial sections with Gaussian broadening.[84, 48, 85] The details of such models are complicated and not relevant for our work, but they describe the dispersion of the dielectric function and its derivatives in a Kramers-Kronig-consistent fashion with a reasonable number of parameters (about 40, compared to 1200 values for ϵ). To be specific, we describe ϵ for Ge with the Herzinger-Johs parametric oscillator model[85] as implemented in the WVASE32 software package.[76] We also included a UV pole at 11 eV, but no IR pole because infrared lattice absorption is weak for a non-polar material like Ge.[55] The number of free parameters can be reduced by keeping some of the shape parameters for Ge the same as those chosen previously[85] for GaAs.

Quoting from Ref. [78], no attempts are made to give a physical meaning to the models. We use them primarily to achieve a flexible Kramers-Kronig-consistent description of the dispersion of real materials with a managable number of parameters. In some cases, fit parameters such as energies or broadenings are related to actual materials properties (such as band gaps), but such agreement is often accidental and should not be over-interpreted. Only the dispersion of the complex

dielectric function and the layer thicknesses are actual outcomes of the fit, but none of the oscillator parameters.

Using oscillators with negative amplitudes is normally frowned upon, because negative absorption has no physical meaning. On the other hand, a combination of oscillators with positive and negative amplitudes can always be replaced with a different combination of oscillators with positive amplitudes. Considering the statement in the previous paragraph that the oscillator parameters should not be taken literally (only the overall dispersion), we find it convenient in some of our models to allow oscillators with negative amplitudes, especially to model the minimum in the absorption coefficient[75] of GeO_2 near 5.4 eV.

Once the model has been built, one varies the parameters using the Levenberg-Marquardt algorithm to minimize the mean-squared error

$$\mathrm{MSE} = \sqrt{\frac{1}{3N-M}\sum_{i=1}^{3N}\left|\frac{\rho_i^{\mathrm{mod}}-\rho_i^{\mathrm{exp}}}{\Delta\rho_i^{\mathrm{exp}}}\right|^2}, \tag{24}$$

where N is the number of data points (all photon energies, incidence angles, and samples), M the number of parameters, ρ_i^{exp} the three experimental quantities (ellipsometric angles ψ and Δ and depolarization) at each data point, ρ_i^{mod} the quantities calculated from the model, and $\Delta\rho_i^{\mathrm{exp}}$ the experimental errors.

4.4 Results for uniform GeO_2 on Ge

The ellipsometric angles and the depolarization for all five Ge/GeO_2 samples were acquired from 0.5 to 6.6 eV as described earlier. This results in ten data sets in the NIR/VIS and VIS/QUV spectral range. All data were loaded into our software and fitted simultaneously.

Figures 20 and 21 show the ellipsometric angles and the pseudodielectric function $\hat{\epsilon}$ for the sample with the thinnest oxide layer (about 2 nm native oxide). Two data sets from 0.5 to 3.0 eV and from 0.76 to 6.6 eV taken on the same day, but under slightly different conditions, were merged in these figures. The differences between the two data sets are no more than 2% of $\hat{\epsilon}$. Most likely, these differences are due to slight non-uniformity across the wafer surface or due to changes in surface conditions between the measurements. The depolarization for this sample is below 0.4% (except at the extreme ends of the spectral range due to noise) and peaks near 3.5 eV. There is no sign of depolarization due to backside reflections below the indirect band gap[57] (E_i=0.66 eV).

The ellipsometric angle ψ is largest for ϕ_0=60° and decreases towards larger incidence angles, see Fig. 20. ψ becomes zero at the Brewster angle (76° for Ge at 2.5 μm). ψ increases gradually towards larger photon energies. The E_1, $E_1+\Delta_1$, E_0, E_2, and E_1 critical points[62] are clearly visible. Δ is near 180° in the infrared and drops towards larger photon energies, as the absorption increases. There is a

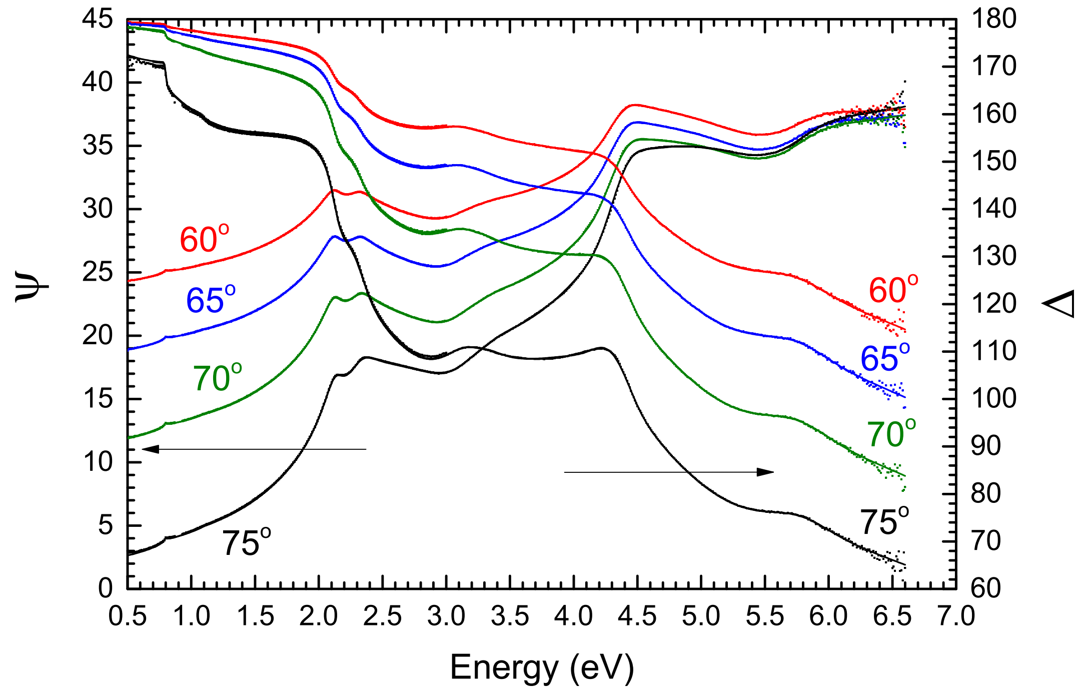

Figure 20: Ellipsometric angles ψ and Δ (symbols) at four angles of incidence (60°, 65°, 70°, 75°) for a Ge wafer with native oxide, after the standard clean described in Sec. 4.2. Two data sets from 0.5 to 3.0 eV and from 0.76 to 6.6 eV were merged. Lines: Data calculated from our model.

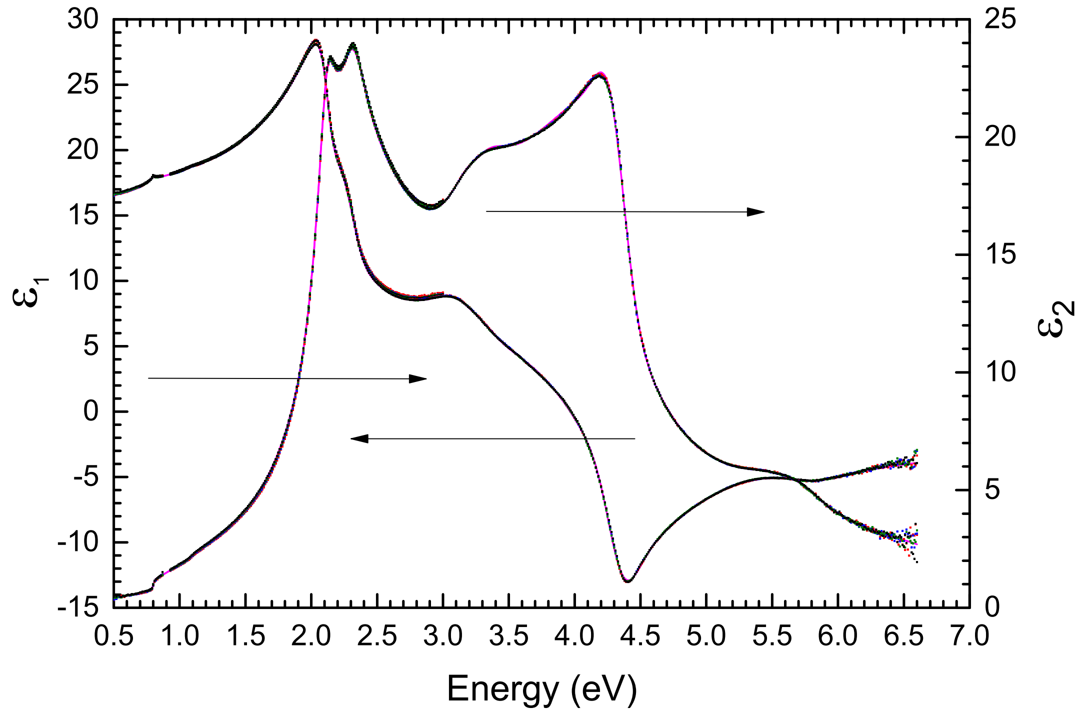

Figure 21: Same data as in Fig. 20, but displayed as a complex pseudodielectric function with real part $\hat{\epsilon}_1$ (green) and imaginary part $\hat{\epsilon}_2$ (blue). Data from our model are shown in red.

sharp drop near the direct gap E_0=0.8 eV and additional drops at critical points with higher energies. Δ also decreases with increasing ϕ_0.

Below the direct gap, Δ should be 180° in the absence of a surface layer, because the absorption nearly vanishes. Instead, $\Delta \approx 170°$ for ϕ_0=75° below 0.8 eV. For both Ge and GeO_2, the refractive index at 2.5 μm (in the transparent region) is fairly well established as 4.07 (Ge) and 1.57 (GeO_2), respectively.[58, 107, 86, 87] Therefore, we are able to calculate that the native oxide thickness for this sample must about 23 Å. This native oxide thickness is consistent with our peak

value of $\hat{\epsilon}_2$=22.6 near 4.2 eV, see Fig. 21, considerably below the literature peak values[61, 63] of 31−32 for bare Ge. We therefore fix the native oxide thickness at 23 Å for our initial fits of sample 1.

Figures 22, 23, and 24 show the ellipsometric angles and depolarization spectra for Ge wafers with thermally grown oxides of 34, 89, and 136 nm thickness. For the 34 nm sample, ψ shows a strong interference fringe near 4.8 eV, while the 89 nm sample shows two interferences fringes at 2.5 and 6.0 eV. The thickest (136 nm) sample shows three interference fringes. At the same energies as the ψ fringes, we also see maxima in the depolarization, which can become quite strong (up to 40%). We model the depolarization with a constant monochromator bandwidth of 4 nm and by selecting a thickness nonuniformity (see Table 3) to match the magnitude of the largest depolarization peak in the UV.[88] Small lateral variations of the refractive index have the same effect as thickness nonuniformity.

Even at 6.1 eV, the ψ interference fringes are still quite strong, indicating that the absorption coefficient of GeO_2 is still small at this energy. The magnitude of the ψ fringes is significantly influenced by depolarization. For example, for the same absorption coefficient (3×10^4 cm^{-1} at 6.1 eV), the peak value of ψ would be 76° for an ideal situation (without depolarization), but this peak is reduced to 63−65° under non-ideal (depolarizing) conditions for our films and experimental setup. Depolarizing effects therefore make it difficult to place an exact value on the absorption coefficient of GeO_2.

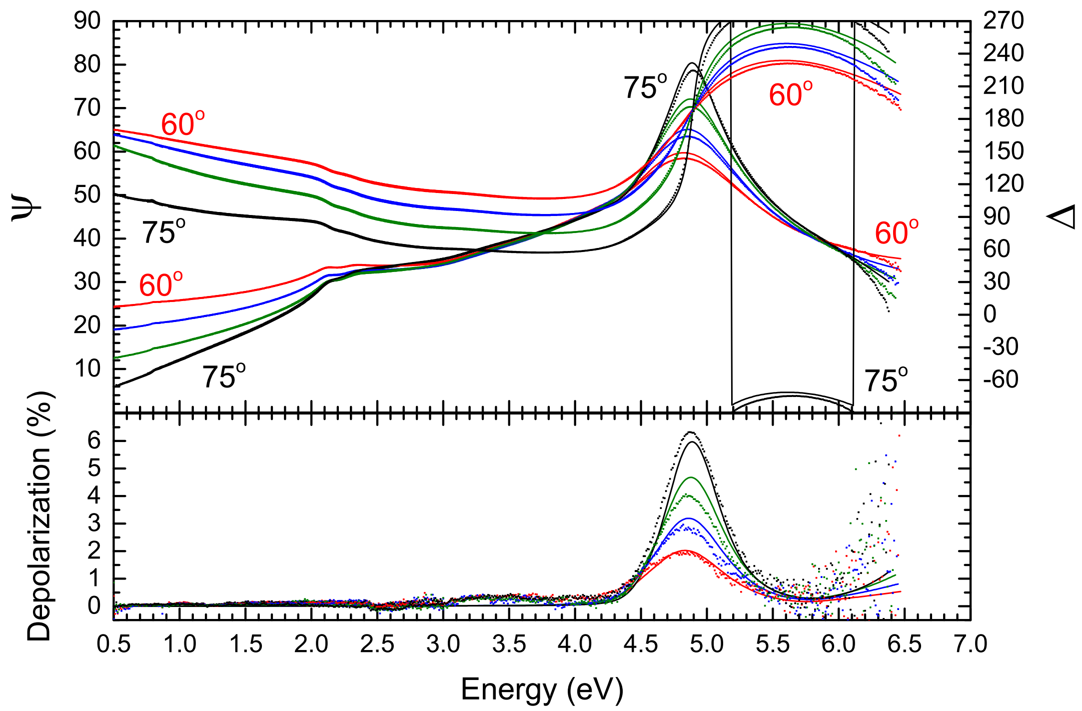

Figure 22: Ellipsometric angles (ψ, Δ) and depolarization (symbols) for 34 nm GeO_2 on Ge. Data from our model (lines).

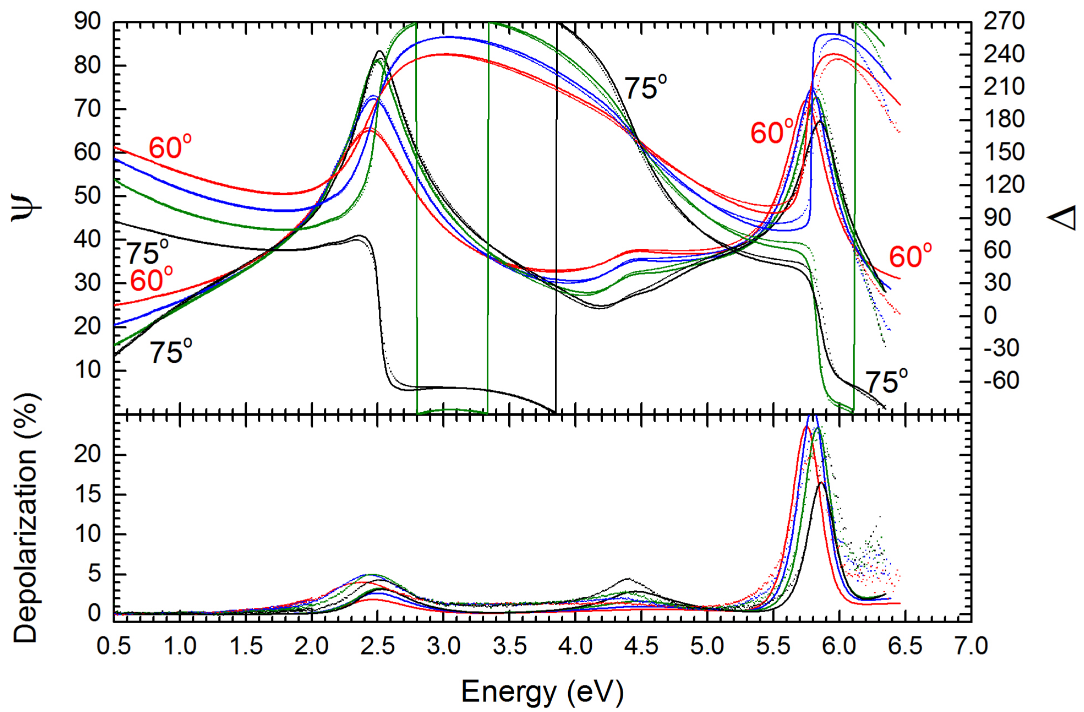

Figure 23: As Fig. 22, but for a Ge wafer with 89 nm GeO_2.

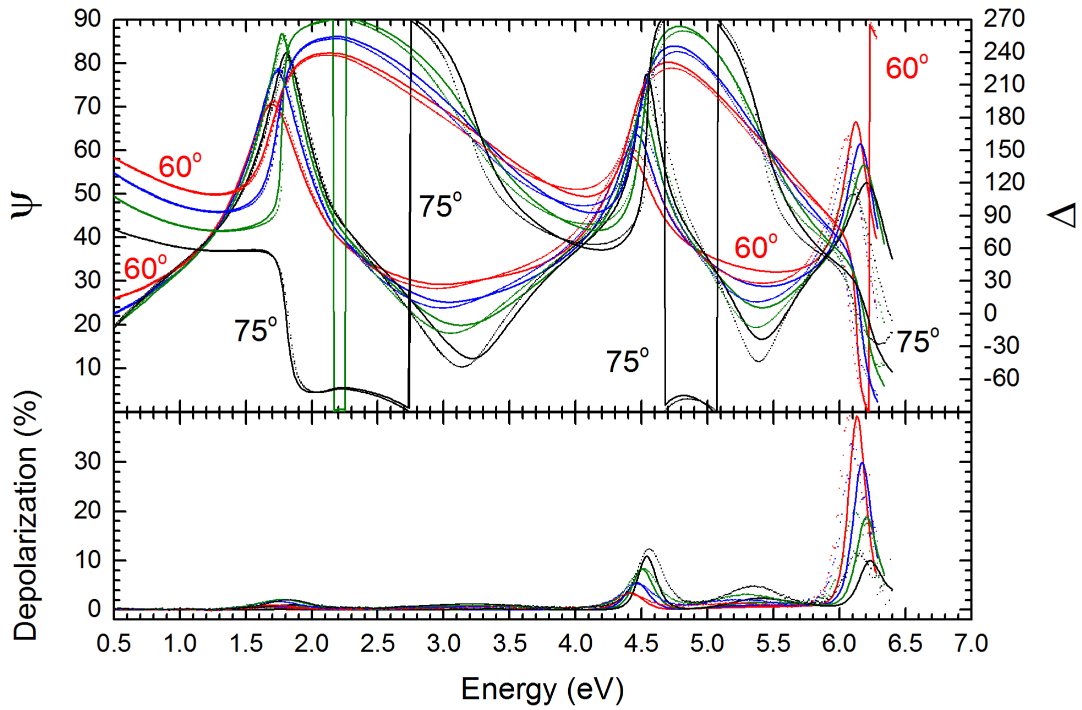

Figure 24: As Fig. 22, but for a Ge wafer with 136 nm GeO_2. The model matches the maxima of ψ, but not the minima. This is a clear indication for a gradient in the refractive index of the film.

We are finally ready to start the fit, using the Tauc-Lorentz parameters fitted to the GeO_2 optical constants[70, 86] and parametric oscillator parameters from the WVASE32 software as starting values. The shape parameters for the E_0, $E_0 + \Delta_0$, E_1, and $E_1 + \Delta_1$ critical points were fixed at the same values as for GaAs. We also fixed Δ_0=0.297 eV and the broadenings for E_0 (10 meV) and $E_0 + \Delta_0$ (20 meV) based on historical transmission measurements.[89]

The material parameters obtained from our best model are given in Tables S-1 and S-2 as supplemental information.[90] The dielectric functions for Ge and GeO_2 are shown in Figs. 25 and 26 and also tabulated[90] in Tables S-3 and S-4. The mean-squared error (MSE) including all five samples in Table 3 was found to be 14. This means that the average deviation between data and model is about 14 times the experimental errors. Half of the MSE is from the thickest oxide layer. Our model gives a near-perfect fit (MSE=0.9) for the Ge substrate with native oxide, but deviations are larger for the thicker oxides. The MSE is just slightly larger (MSE=18) for a non-absorbing model for GeO_2 using two UV poles. We suspect that the largest sources of deviation for the thicker oxide samples are the depolarization and errors in the ellipsometric angles (especially in the UV) due to thickness variations across the samples.

To estimate the accuracy of the GeO_2 optical constants shown in Fig. 26, we proceed as follows: The lines in Fig. 27 show the best fit to all samples with a Tauc-Lorentz layer for the GeO_2 oxide. This fit also determines the thicknesses of

all oxides, see Table 3. Next, we only fit the 89 nm oxide with an uncorrelated all-wavelength inversion of the ellipsometric angles at fixed thickness, where Kramers-Kronig consistence is not enforced. (This is also known as a point-by-point fit.) The results of this fit are shown by symbols in Fig. 27. We then perform the same fit for another sample with 136 nm thickness and also show the results by symbols. We can see that the differences between the Tauc-Lorentz fit to all samples (assuming uniform identical oxide layers) and the single-sample point-by-point fits are quite large (up to 10% for ϵ_1). Furthermore, we see oscillations in the data, which are probably artifacts due to incomplete removal of interference fringes. Values of ϵ_2<0.1 are probably not reliable, but it appears that there is some absorption in the oxide above 6 eV. It has been reported[91] that the absorption coefficient of GeO_2 depends on the details of preparation. Therefore, it is possible that poor agreement between data and model in the deep UV are due to sample-to-sample variatons, which we have ignored in our model.

4.5 Results for GeO_2 on Ge with non-uniform layer fits

Since the quality of our fit with a three-phase (ambient-film-substrate) model is only moderate (MSE=14), we discuss how the fit might be improved by adding more complexity to our model. We focus on the UV spectral region, where the discepancy between data and model is largest. (For sample 1, the native oxide, the differences between the measured ellipsometric angles and the model are much

less than 1°. The differences reach several degrees or even more for thicker oxides, especially in the UV.) First, we note that adding additional oscillators in the UV spectral region (beyond the Tauc-Lorentz oscillator and poles at 11 and 0.05 eV) does not reduce the overall MSE.

Next, we allow the density of the thickest oxides to vary between the bottom and top by adding a variable-density layer on top (effective medium layer with variable thickness and variable void fraction). This reduces the MSE to 8.3 and somewhat improves the fit in the UV for the thicker oxides. The void fraction in this layer is quite low (near 20% and the thickness large, several tens of nm). This model would also account for surface roughness as a special case (with a 50% void fraction), which does not appear to be a major factor due to the low void fraction resulting from the fit. Similar results can be obtained by describing the oxide as an effective medium, where the void fraction follows a power law with a large exponent (about 5) and reaches about 30% near the surface. Finally, our best model (MSE=6.9) adds an additional Gaussian absorption in the UV, which leads to a kink in the absorption as shown in Fig. 27.

As a generalization of this effective-medium-approximation (EMA) model, we can also describe the oxides with a graded-layer model, where the complex refractive index depends on thickness through a power law with a variable exponent. The refractive index in such models is typically about 20% lower at the surface than at the substrate/oxide interface and the exponent quite high (indicating that

the low-density region is confined to the top 20% of the film).

We also added an interfacial layer with variable thickness (kept the same for all samples), which consists of a 50/50 mixture of the bulk and film optical constants described within the Bruggeman effective medium approximation. The rationale for this model is that some electrons in the bulk Ge might leak out into the oxide (have a finite probability to be located in the GeO_2 barrier). It has also been shown theoretically[92] for the Si/SiO_2 interface that the first 7-10 Å of the oxide have a different structure and density than thick oxides. Using this intermix model, which assumes a higher electron density near the interface than in a thick oxide, did not improve our fits and therefore we discarded this possibility.

4.6 Discussion

Since a three-layer (ambient-oxide-substrate) model with uniform GeO_2 layers gives good agreement with our ellipsometry data and cannot be improved much by introducing more complexity, we consider the results from our uniform three-layer fit the final results from this work. Results for the complex dielectric function, complex reftractive index, absorption coefficient, and normal-incidence reflectance for Ge and GeO_2 as a function of photon energy and wavelength are given in Tables S-3 and S-4 of the supplemental materials.[90]

The complex dielectric function of Ge from our fit together with literature results[61, 63] and an unpublished data set[76] are shown in Fig. 25. Our ϵ_2

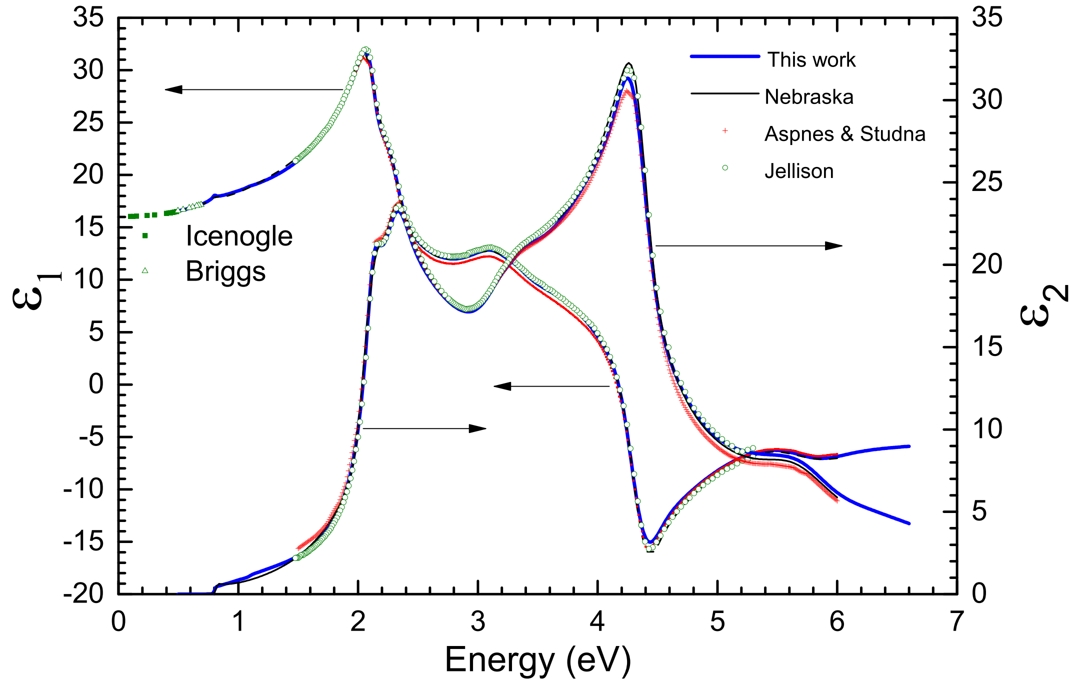

Figure 25: Complex dielectric function for Ge from a fit to our ellipsometry results in comparison with literature data.[63, 61, 76, 58, 107]

maximum of 31.3 at 4.25 eV is between the results of Ref. [61] and Ref. [63] and slightly lower than the unpublished Nebraska result[76]of ϵ_2=32.3. Since we determined the oxide thickness for our thinnest sample (native oxide) using the Jellison-Sales method[67] with measurements below the Ge band gap, we believe that our results are highly accurate. At 0.5 eV, below the band gap, our refractive index n=4.07 is identical to minimum-deviation prism results.[58, 107] The maxima and minima of our spectra related to critical points and interband transitions[62] will be discussed elsewhere.

Figure 26 shows the dielectric function for GeO_2 from our fit in comparison

with prior data.[70, 86] The results for thermal oxides produced by Hu *et al.*[70] cover the energy range from 1.5 to 5.5 eV, while Devyatykh *et al.*[86] measured bulk crystals from 0.5 to 2.5 eV using the minimum-deviation prism method.

Our value of ϵ_1 at 0.5 eV equals 2.4 (corresponding to n=1.55), which is about 4% lower than prior results.[70, 86] Our values do not depend much on the details of our Tauc-Lorentz model (such as the strength of the IR pole, the Tauc gap, or including a density gradient). Therefore, it is possible that our GeO_2 oxides indeed have a lower density (resulting in a lower refractive index) than films and crystals produced by others, perhaps related to our fast high-pressure oxidation conditions (see Fig. 18). For the Si/SiO_2 system, it is known that oxides with lower density have a lower refractive index.[93, 94, 95, 96] Variations of the index of a silicate glass by 5-10% are common (even without adding heavy metals to increase the index). On the other hand, Fig. 27 also demonstrates that the accuracy of our GeO_2 refractive index measurement is only about 5%, because an oscillator fit may yield a different result than a direct point-by-point inversion. Pajasova[87] provided accurate measurements of the refractive index n for bulk glassy GeO_2 in the transparent region from 0.4 to 2.5 μm using the minimum-deviation prism measurements. She found that n decreases from 1.57 at 1 μm to 1.56 at 2.5 μm (ϵ_1=2.43), quite similar to our values.

Pajasovas[87] results for ϵ_2 of GeO_2 are less accurate, because they were obtained from Kramers-Kronig transformation of reflectance data, but they clearly

indicate strong absorption peaks at 6.6 and 10.7 eV, outside of our spectral range. From measurements on RF-sputtered GeO_2 films with 0.77 to 6 μm thickness,[75] the onset of strong absorption was found to be about 5.95 eV. Below the main band gap, there is an absorption peak with a magnitude of about 200 cm^{-1} centered at 5.06 eV, which was found in bulk crystals[91] as well as in thin films.[75] This peak depends on preparation conditions and disappears after annealing at high temperatures of bulk specimens or films on fused silica.[75] This below-gap absorption has been attributed to oxygen vacancies,[91] which are also expected in our thermal oxides due to oxide decomposition.[72] In our absorption coefficient data derived from ϵ for GeO_2, we determine α=2$\times$10^4 cm^{-1} (the threshold of our sensitivity, compare Fig. 27) at 6 eV, considerably larger than α=0.5$\times$10^4 cm^{-1} found by transmission measurements on sputtered films.[75] It is common for spectroscopic ellipsometry measurements to overestimate small absorption coefficients.[97]

4.7 Summary

We developed a hybrid dry-wet preclean for thermal oxidation of Ge and produced thermal oxides on Ge at 550°C and 270 kPa O_2 pressure, with oxide thicknesses ranging from 34 to 136 nm and oxidation times up to 10 hours. Multi-sample ellipsometry analysis of these oxides determined the dielectric functions of Ge and GeO_2 from 0.5 to 6.6 eV. We carefully discuss the accuracy of our results and compare with prior data.

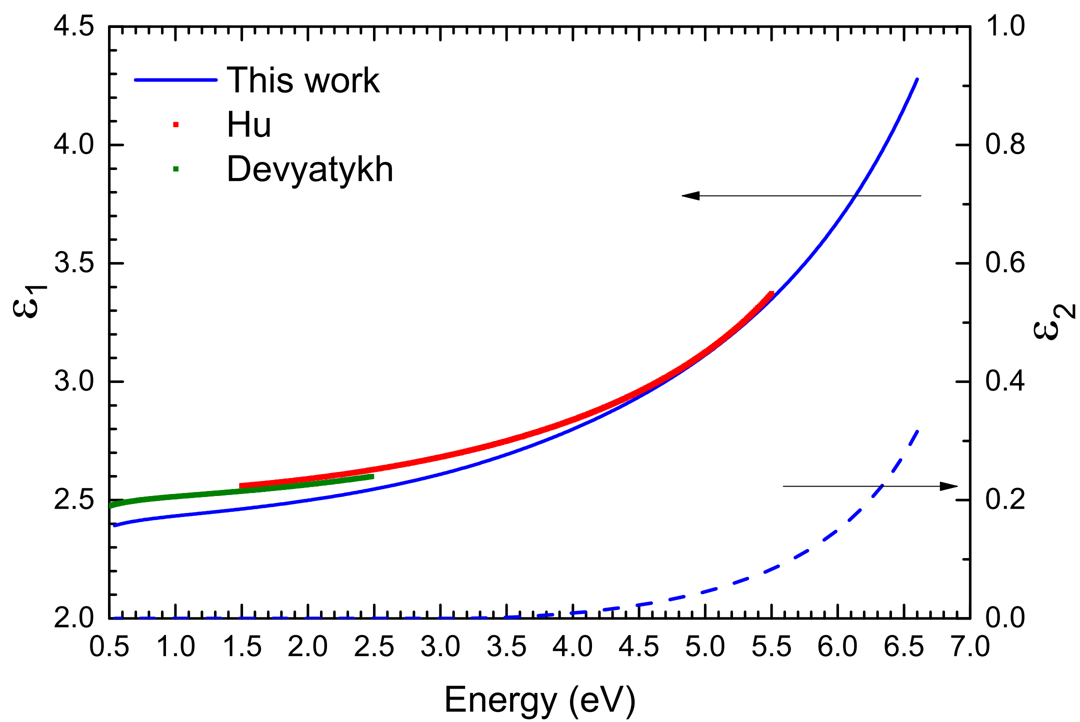

Figure 26: Complex dielectric function for GeO_2 from fit to our ellipsometry results in comparison with literature data.[70, 86]

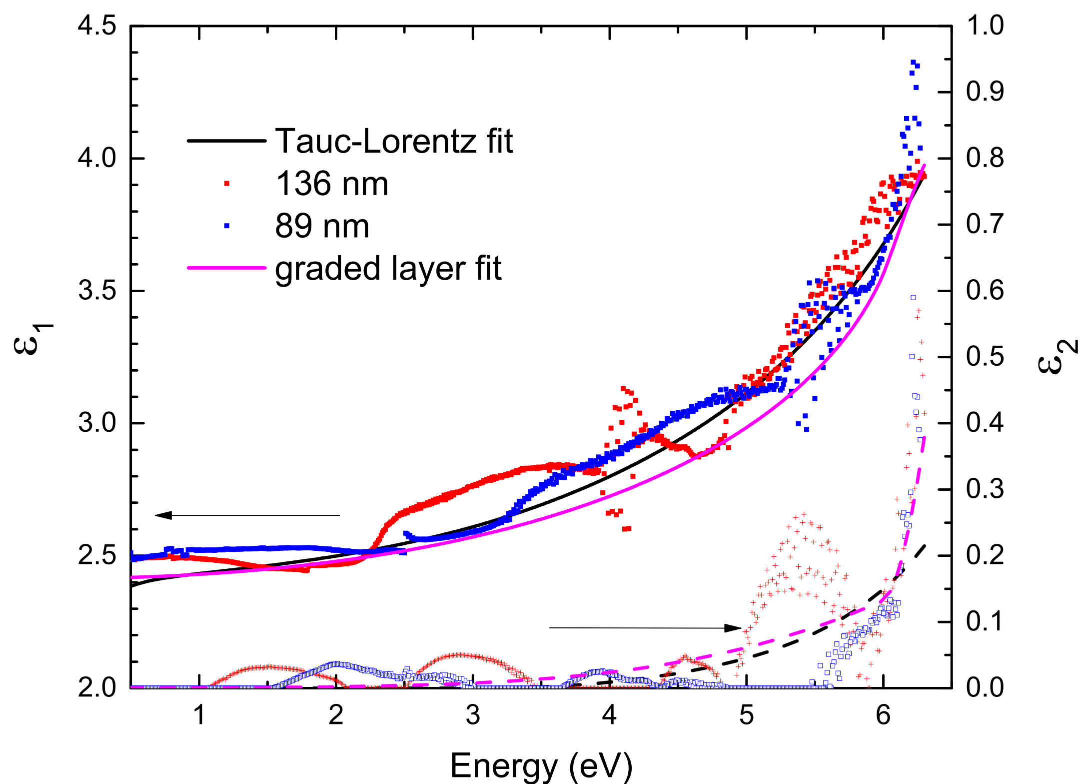

Figure 27: To estimate the accuracy of the optical constants for GeO_2, we plot the dielectric function obtained from various methods: From a Tauc-Lorentz fit to all data assuming uniform oxide density, from fits of single samples (89 nm and 136 nm thickness) with uniform density, and a two-oscillator fit (Tauc-Lorentz and Gaussian) to all data allowing a density gradient for the thicker oxides.

Acknowledgments

This work was supported by the Air Force Office of Scientific Research (FA9550-13-1-0022) and by the Army Research Office (W911NF-14-1-0072). Support during 2016 was provided by the National Science Foundation (DMR-1505172). J.M.M. and A.A.M. acknowledge support from the New Mexico Alliance for Minority Participation (NM-AMP).

5 TEMPERATURE-DEPENDENT DIELECTRIC FUNCTION OF NICKEL

This chapter is a paper presented as it was submitted before review to the Applied Surface Science 7th International Spectrosopic Ellipsometry special issue.

Stefan Zollner, T. Nathan Nunley, Dennis P. Trujillo, Laura G. Pineda, Lina S. Abdallah

Department of Physics, New Mexico State University, MSC 3D, P.O. Box 30001, Las Cruces, NM 88003-8001

Abstract

Confirming historical results [L.S. Ornstein and O. Koefoed, Physica **5**, 175 (1938)], the authors found an anomaly in the optical constants at 1.96 eV for bulk nickel near the Curie temperature through careful high-precision spectroscopic ellipsometry measurements from 80 to 800 K. The anomaly is only seen in sweeps with increasing temperature if the sample carries a net magnetization. In decreasing temperature sweeps or for unmagnetized samples, the anomaly is absent. The sign of the anomaly in the optical conductivity at 1.96 eV is in contrast to the sign of the anomaly in the electrical DC conductivity. The anomaly is rather large and therefore explained with changes in the on-diagonal Drude-Lorentz portion of the dielectric tensor. No sign of anisotropy (polar magneto-optical Kerr effect) is found in the data.

Spectroscopic Ellipsometry, Nickel, Curie temperature, Ferromagnetic, Dielectric function, Temperature dependence

5.1 Introduction

About 80 years ago, the group of Professor Leonard S. Ornstein in Utrecht (Netherlands), a student of Hendrik Lorentz, measured the temperature dependence of the near-normal incidence (15°) reflectance of ferromagnetic metals near the Curie temperature [98, 99]. Recent interest in these important studies has been weak. The most prominent recent citation to this work is a book by Sokolov [100] on the optical properties of metals published in 1967.

For a free-standing thin film of Fe [98] with 40 μm thickness, they found that the reflectance R at 650 nm (1.91 eV) increased gradually from 62% at 1000 K to 66% at 1100 K, near its Curie temperature (T_C=1043 K). A similar increase from 64% to 68% was found between 1100 and 1300 K for Fe-Co alloys [99]. For a Ni thin film [99], on the other hand, they found a decrease by about 0.5% between 500 and 700 K, near T_C=627 K, see Fig. 28. They explained these observations with changes of the magnetic properties of free carriers near T_C.

In this manuscript, we describe high-precision measurements of the pseudo-dielectric function ϵ of Ni at 1.96 eV (632 nm) as a function of temperature from 100 to 800 K. We observe a strong anomaly in the pseudo-dielectric function near T_C, but it has the opposite sign compared to [99].

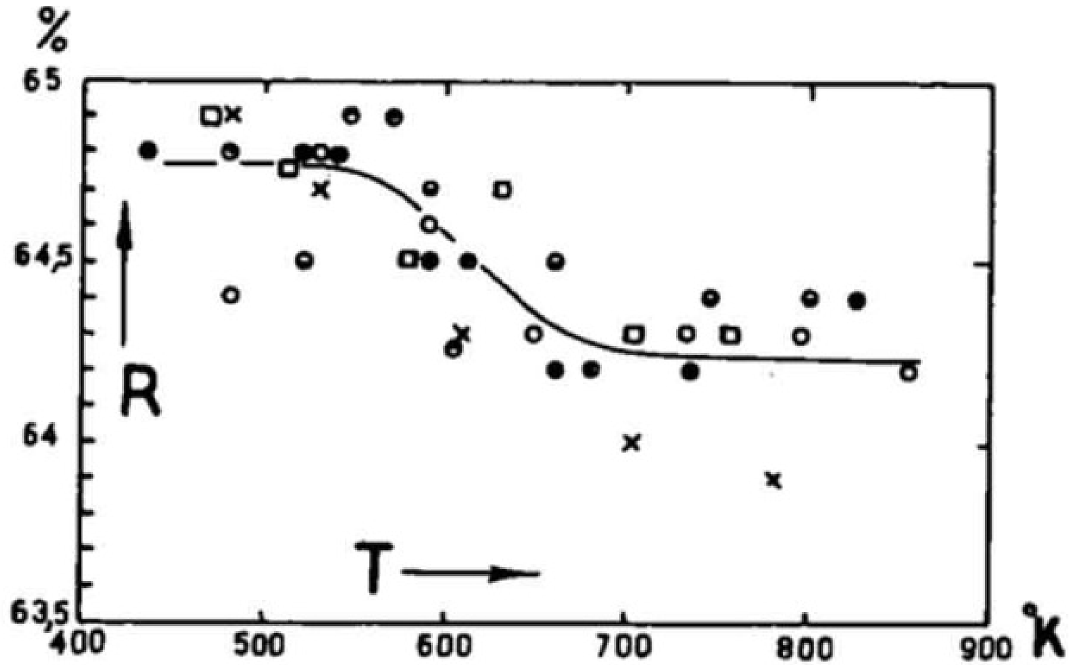

Figure 28: Reflectance of Ni at 1.91 eV as a function of temperature [99].

5.2 Experiment

Our ellipsometry measurements were performed at a 70° incidence angle and a photon energy of 1.96 eV on a vertical variable angle of incidence spectroscopic ellipsometer (J.A. Woollam Co.) equipped with a computer-controlled Berek wave plate compensator, as described elsewhere [101]. To increase accuracy, measurements were performed with both positive and negative polarizer angles. Most measurements assumed an isotropic sample. We did not find significant off-diagonal elements of the Jones matrix (or Müller matrix elements associated with anisotropy) [102, 103]. The detection electronics were slightly modified to avoid saturation of the detector due to high-intensity black-body radiation at the highest sample

temperatures.

The sample was attached to a coldfinger with metal strips, inside a commercial UHV cryostat (J.A. Woollam Co., model CRV-717V, manufactured by Janis Research Co. as model ST-400) evacuated by a turbo pump to a base pressure below 10^{-8} Torr. The cryostat has low-stress quartz windows with a polarization response calibrated at room temperature, with automatic corrections to the ellipsometric angles performed by the data acquisition software. Using liquid nitrogen, the crystat allows measurements with sample temperatures from 80 to 800 K. Throughout most of this temperature range, the cryostat windows remain near room temperature. At sample temperatures above 600 K, however, the windows get slightly warm, which may influence their polarization correction. A gold-coated heat shield around the coldfinger containing the sample reduced radiation losses. To avoid temperature gradients between heater and sample, it was important to keep the radiation shield in place throughout the entire temperature range.

For measurements below 300 K, liquid nitrogen was transferred into the coolant reservoir with a transfer arm designed for liquid helium. For measurements above room temperature, the transfer arm was removed and the cryogen reservoir was instead evacuated by a rotary pump to reduce corrosion at high temperature. The sample stage was heated with a 50 Ω resistor. The temperature was controlled by a type E thermocouple located near the cryogen reservoir and by applying power

to the resistive heater. To ensure accurate temperature measurements, a second type E thermocouple inside a stainless steel sheeth was fed into the UHV space and clamped directly on top of the front surface of the sample. This step was crucial for accurate temperature measurements, since differences of up to 50 K between the two thermocouples were found. Throughout this study, we report the sample temperature, not the control temperature. The entire temperature series was acquired without breaking the vacuum.

We purchased bulk polycrystalline single-side polished Ni substrates with 1 mm thickness from MTI Corporation (Richmond, CA). These pieces had a grain size of 10-50 μm and an rms surface roughness of 3 nm. We also obtained a 100 nm thick Ni film with (111) texture and much lower roughness sputtered on a SiO_2 coated Si wafer from R.J. Davis (Nanotech West Lab, The Ohio State University). Both types of samples produced similar results. We therefore describe only the bulk Ni experiments.

Ellipsometry results on Ni are affected not only by surface roughness (which we are unable to influence), but also by adsorbed overlayers, especially water and organic contaminants [104]. While surface roughness is independent of temperature (until grain growth or melting occurs at sufficiently high temperatures, much larger than T_C) and therefore should not lead to discontinuities in the temperature dependence of the dielectric function, surface layers can evaporate or condense on the sample as the temperature is varied. Therefore, careful preparation of the

sample is required to achieve clean results unaffected by surface effects.

As-received Ni samples were magnetized by placing them between two axially magnetized N52 NdFeB permanent magnets with a magnetic field of 1.4 T. Alternatively, for some experiments the Ni samples were placed between the pole shoes of a large electromagnet in a magnetic field of 1 T. Both fields should be sufficient to saturate the magnetization of the bulk and thin-film Ni samples and orient the magnetic moments perpendicular to the surface.

After magnetization, the samples were subjected to an ozone clean in a Novascan PSD Pro Series digital UV ozone cleaning system utilizing a Hg vapor lamp. This clean was performed in an oxygen-enriched environment, achieved by allowing ultrapure oxygen to flow through the system for several minutes. Then, we sealed the chamber, turned on the Hg lamp, and held the sample on a heating stage at 150°C for 60 minutes, followed by a 30 minute period of incubation with the lamp off and the sample cooling to room temperature.

After this clean, the sample was mounted on the cold finger, the heat shield was attached, and the cryostat was sealed, then pumped down for 24-48 hours. The sample was then heated to 450 K for 12 hours to remove surface contamination (degas), then cooled down to room temperature and pumped until a base pressure of about 10^{-8} Torr was reached. Next, we filled the cryogen space with liquid nitrogen using the liquid helium transfer arm and allowed the sample to cool to about 80 K and reach thermal equilibruium. The transfer arm was removed

and a second roughing pump was connected to the cryogen exhaust port of the cyogen reservoir (but not yet turned on). We finally started the measurement by taking ellipsometry data every 30 s with a nominal heating rate of 2 K/min. In the beginning, the sample warmed up very slowly (because the liquid nitrogen needed to evaporate). When the sample temperature reached 90 K, all of the liquid nitrogen had evaporated and we could seal the opening for the transfer arm with a rubber stopper. We also turned on the second roughing pump to evacuate the cryogen space to avoid corrosion. The temperature ramp rate also slowed down considerably at the highest temperatures, when the whole cryostat enclosure warmed up.

From this point (90 K) on, the measurement ran for several hours without intervention, touching the setup, or making alignment adjustments. This ensured the ultimate precision of the temperature-dependent ellipsometric angles achievable using our setup. After, the maximum temperature was reached (800 K control temperature, 760 K sample temperature), we turned off the heater and allowed the sample to cool down to room temperature, while continuing to take data. When the sample temperature had reached 350 K, this concluded Run 1. We then performed Run 2 and Run 3 in an identical manner.

5.3 Results

The pseudo-dielectric function $<\epsilon>$ at 1.96 eV for bulk polycrystalline Ni versus temperature for all three runs is shown in Fig. 29. The arrows indicate the direction of the temperature ramp (rising or lowering temperature with increasing time).

During Run 1, for magnetized Ni, $<\epsilon_1>$ increases nearly linearly from -10.8 at 80 K to -10.2 at 580 K, then drops sharply to -10.7 at 640 K, and then continues its linear increase towards higher temperatures. At this point, the Ni sample has been heated above T_C and is in its paramagnetic state. Cooling the sample below T_C will result in an unmagnetized sample, where the magnetic moments of the magnetic domains in the sample are randomly oriented. As the sample temperature is lowered during Run 1, $<\epsilon_1>$ takes a different trajectory than during the increasing temperature scan for the magnetized sample. For the unmagnetized sample, $<\epsilon_1>$ decreases nearly linearly with decreasing temperature to -12 at 80 K. Runs 2 and 3 (in both directions) show identical results as the decreasing temperature ramp for the demagnetized sample during Run 1. If we remove the sample from the cryostat and magnetize it again using the permanent magnet as described earlier, we can repeat the results of the increasing temperature ramp in Run 1.

The imaginary part $<\epsilon_2>$ shows similar results: It is nearly constant (12.5)

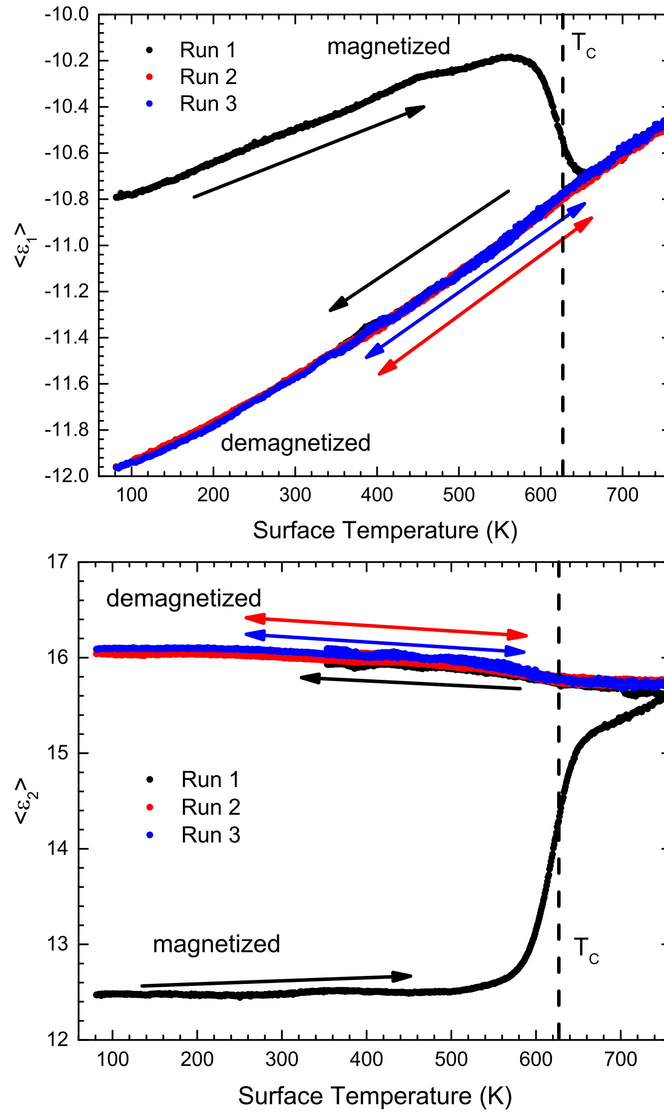

Figure 29: Real and imaginary parts of the pseudodielectric function of bulk polycrystalline Ni at 1.96 eV as a function of temperature. The arrows indicate the direction of the temperature ramp with increasing (right) or decreasing (left) temperature versus time. The dashed lines show the Curie temperature of Ni at 627 K.

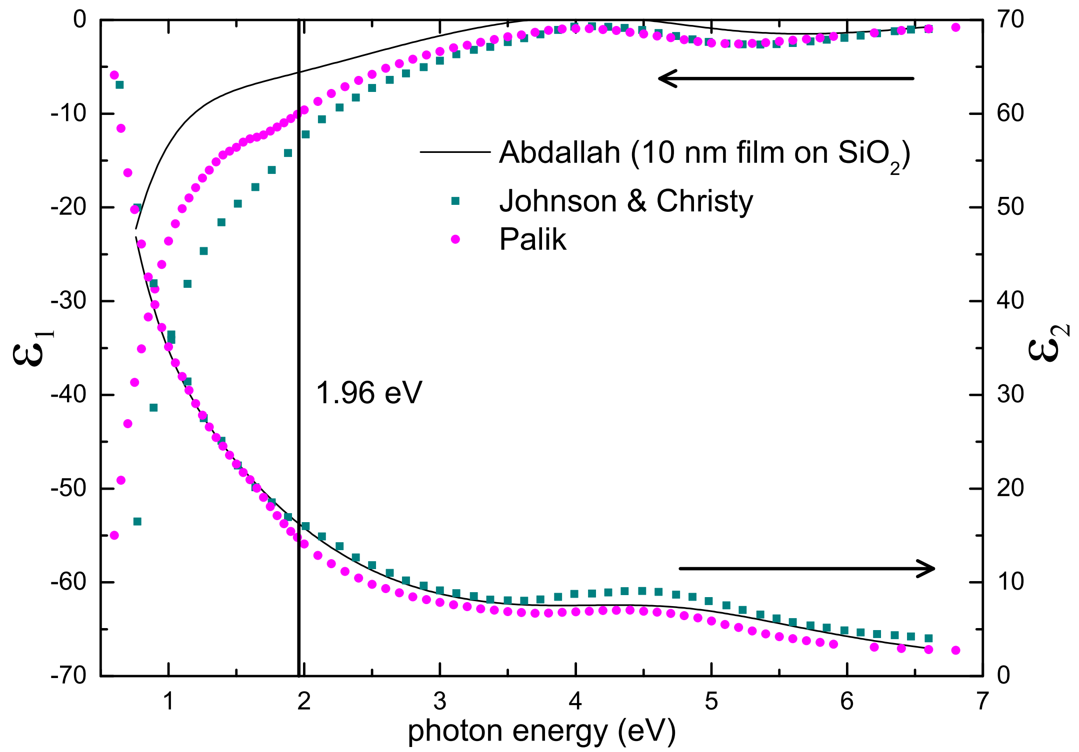

Figure 30: Real and imaginary parts of the dielectric function of Ni at 300 K versus photon energy, taken from three different literature sources [104, 106, 107]. A vertical line was drawn at 1.96 eV, were our temperature dependent measurements were performed.

between 80 and 560 K, then rises sharply to 15 at 650 K, then rises more slowly to 15.6 at 760 K. The decreasing temperature ramp for Run 1 (which is identical to Runs 2 and 3) has very different results, where $<\epsilon_2>$ only varies slowly and remains nearly constant around 15.6-16.2.

In this case, the ellipsometric angle ψ (not shown) is mostly responsible for the response of $<\epsilon_1>$, while Δ is responsible for the response of $<\epsilon_2>$. Since a similar response is seen in both ψ and Δ, this is not likely an artifact from the windows (where Δ should be affected much more than ψ). At T_C, ψ decreases by 0.5° and Δ increases by 5°. These are large changes in the ellipsometric angles. Typical precision for this ellipsometer is quoted as 0.01° for ψ and 0.1° for Δ.

5.4 Discussion

The geometry of our experiment corresponds to the magneto-optical polar Kerr effect [105], since the magnetization of the bulk samples is normal to the surface. The dielectric tensor for the Ni sample in the laboratory coordinate system (where the z-axis is the surface normal) is [108, 103]

$$\epsilon = \epsilon_{\mathrm{DL}} \begin{pmatrix} 1 & -iQ & 0 \\ iQ & 1 & 0 \\ 0 & 0 & 1 \end{pmatrix}, \tag{25}$$

where ϵ_{DL} is the diagonal part of the dieletric tensor in the absence of magnetization, usually written as a sum of Drude and Lorentz oscillators [109, 104], and Q is the complex Voigt parameter, proportional to the magnetization of the

sample [105, 110]. For Ni, $\epsilon_{\rm DL}Q$ at 633 nm is small, about 0.3 [110, 109]. This explains why no anisotropy (off-diagonal Jones matrix elements) was observed in our measurements.

The observed changes in $<\epsilon>$, see Fig. 29, are much larger and therefore must be related to the on-diagonal component $\epsilon_{\rm DL}$ of the dielectric tensor. As mentioned, $\epsilon_{\rm DL}$ has two components, due to the Drude response of free carriers and due to interband transitions which are modeled as a sum of Lorentz oscillators [104]. Studying the temperature dependence of $<\epsilon>$ at many photon energies might provide experimental evidence if the Drude part or the Lorentz part of ϵ is responsible for the discontinuity at T_C. An inspection of ϵ versus photon energy (see Fig. 30) shows that both terms contribute to ϵ at 1.96 eV.

The key to understanding the origin of the discontinuity of $<\epsilon>$ near T_C can perhaps be found by studying the temperature depencence of the electrical (DC) conductivity of Ni [111, 112, 113, 114], which shows a similar discontinuity near T_C. This anomaly was explained by Mott [115, 116, 114] as follows: Ferromagnetic transition metals contain both s- and d-electrons. Almost the entire electrical current is carried by the s-electrons, because they have a much smaller effective mass than d-electrons. On the other hand, the electrical conductivity is determined by electron-phonon scattering from the s- to the d-band, because the d-band has a very large density of states, thus lowering the conductivity. Above T_C, s-electrons can scatter into both spin states in the d-band. However, below T_C one d-band is

full and scattering can only occur to the d-band with the other spin state, thus increasing the conductivity. Other theories [116, 117, 113, 118] explain the decrease of the conductivity above T_C by the exchange interaction coupling between conduction electrons and disordered atomic spins, especially in the vicinity of T_C.

We find the opposite behavior in the temperature depencence of $<\epsilon_2>$, which is related to the optical (frequency-dependent) conductivity σ_1 through $\sigma = -i\omega\epsilon_0\epsilon$. Below T_C, $<\epsilon_2>$ is relatively low (around 12.5), but it rises anomalously to 15 above T_C. In conductivity units, the optical conductivity σ_1 at 1.96 eV rises from 3300 to 4000 $1/\Omega$cm near T_C. Compare Fig. 4 in [104].

While it is tempting to assign s- to d-band electron-phonon scattering above and below T_C to the anomalies in the electrical and optical conductivity, it is puzzling that the two anomalies have the opposite sign. Our optical conductivity versus temperature curve (similar to $<\epsilon_2>$ in Fig. 29) has the same S-shape as the DC resistivity versus temperature curve in Bittel and Gerlach [111].

Finally, for comparison of our data with the historical results of Ornstein and Koefoed [99] shown in Fig. 28 we calculate the normal-incidence pseudo-reflectivity from our peudo-dielectric function (Fig. 29). The results are shown in Fig. 31. While the reflectance is of the same magnitude (near 65% in both cases), our results show a decreasing trend with increasing temperature whereas the baseline in Fig. 28 is flat. There is a small ($\sim$0.1%) anomalous increase in our pseudo-reflectance near T_C, in contrast to the 0.5% decrease seen in Fig. 28. As

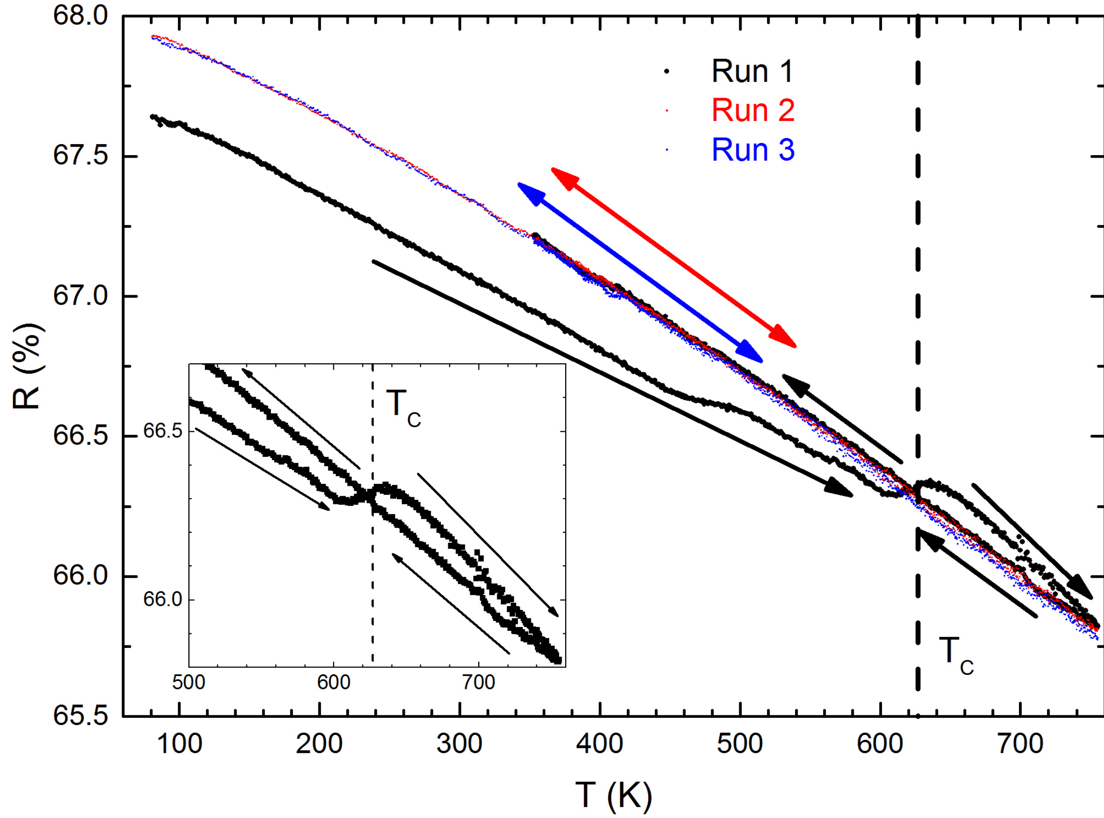

Figure 31: Normal-incidence pseudo-reflectance at 1.96 eV for bulk Ni as a function of temperature, calculated from the pseudo-dielectric function shown in Fig. 29. The dashed vertical line indicates the Curie temperature T_C for the first run. The inset shows the range near T_C. The arrows show the direction of the temperature ramp with increasing (right) or decreasing (left) temperature versus time.

mentioned earlier, an increase in the reflectance near T_C was also found for iron and other metals [98] and only Ni showed a decrease in the historical results [99]. The calculated changes in the peudo-reflectance are very small compared to the large anomalies observed in the pseudo-dielectric function (Fig. 29).

We also must mention that the optical conductivity anomaly observed in this work depends on the macroscopic net magnetization of the sample. Therefore, we only observe this anomaly in the increasing temperature portion of Run 1. Once the sample has been heated above T_C, the net magnetization disappears and optical anomaly can no longer be observed. On the other hand, the electrical DC conductivity anomaly depends on the microscopic magnetization of each magnetic domain and therefore is observed during increasing and decreasing temperature scans.

5.5 Summary and Outlook

Through high-precision temperature dependent ellipsometry at 1.96 eV, we provide new experimental evidence regarding the nearly hundred year-old investigation of the anomaly of the conductivity near the Curie temperature of ferromagnetic metals. We confirm that there is an anomaly in the optical constants of Ni at 1.96 eV near T_C=627 K. However, there are significant discrepancies regarding the sign of this anomaly. While our results correspond an increase in reflectance for Ni (similar to iron [98]), Ornstein and Koefoed [99] found a decrease. Also, we

find an increase in the optical conductivity at 1.96 near T_C, while the DC electrical conductivity is known to decrease at T_C because of the increased probability for electron-phonon scattering of s-band conduction electrons into the unfilled d-band states in the spin-disordered paramagnetic state above T_C.

We argue that the large changes in optical constants near T_C found in this study are due to the on-diagonal portion of the dielectric tensor. They are not compatible with the small off-diagonal elements related to the Voigt parameter and the polar magneto-optical Kerr effect. The absence of measurable off-diagonal elements in the Jones matrix also confirms that our results are from the on-diagonal (Drude) part of the dielectric tensor.

Acknowledgments

This work was supported by the National Science Foundation (DMR-1104934 and DMR-1505172). LGP acknowledges support from the New Mexico Alliance for Minority participation (NM-AMP).

6 OUTLOOK AND SUMMARY

The work presented in this thesis consisted of the acquisition of optical constants of various solid-state systems under different conditions and energy ranges. While the work presented was comprehensive in many ways, the systems in question still pose some questions to be answered or possible improvements to be made.

The electronic and vibrational properties of bulk LSAT were studied extensively through optical and X-ray techniques. The issue with a complex system such as this is that it doesn't lend itself to computational methods due to the large possibility of variation in composition on the nano scale as seen through the FCC ordered sites as measured by X-ray diffraction. Sample to sample variation was also seen between the infrared data taken from our sample and the data received from Switzerland taken from another substrate in the form of differing phonon amplitude. Possible future studies on the system may include acquiring samples from several sources and measuring the size of the FCC ordered sites along with studying the range of phonon amplitudes. If there is a correlation between the amplitudes of certain phonons and the size of the FCC sites it would be possible to use XRD to calculate the corresponding dispersion in the IR spectra. Without the ability to know what the correct dispersion of an LSAT substrate is, it may be difficult to study the lattice vibrations of deposited thin films.

The biggest problem that was faced in the analysis of the thermal Ge oxide

on Ge was that the samples had non-uniform oxide thicknesses (optical path lengths). This led to large depolarization in the spectra. The reason for this is possibly because of the relatively small sample size and the configuration of the annealer used. If the study were to be done with large wafers, which were oxidized in a way which allowed for uniform pressures across the wafer, the amount of non-uniformity of the film could be minimized. This would allow for easier analysis and possibly an even greater increase in optical constant precision for Ge.

The Ni was studied using only one wavelength. While this provided confirmation of previous results, it has prompted us to study the result over the full spectral range. This could lead to a greater understanding of the mechanism of the transition and also the full range of optical constants as a function of magnetization. It would also be very useful if the study were done with sample magnetizations other than the maximum magnetization, which could show whether or not the effect is linear as a function of magnetization.

This thesis has succeeded in both contributing to our current knowledge of solid-state physics and showing which subjects should continue to be studied in each system so that a comprehensive understanding may be achieved.

REFERENCES

[1] S. Richard, F. Aniel, F. Fishman, Phys. Rev. B 70, 235204 (2004)

[2] C. Kittel, *Introduction to Solid State Physics, 8th ed.* (John Wiley & Sons, New Jersey, 2005).

[3] M. Fox, *Optical Properties of Solids, 2nd ed.* (Oxford University Press, New York, 2013).

[4] W.A. Harrison, *Solid State Theory* (Dover Publications, New York, 1980).

[5] W.A. Harrison, *Electronic Structure and the Properties of Solids* (Dover Publications, New York, 1989).

[6] G.E. Jellison Jr. F.A. Modine, Appl. Phys. Lett. **69**, (3), (1996).

[7] J. Tauc, R. Grigorovici, A. Vancu, Phys. Stat. Sol. **15**, 627 (1966).

[8] H. Mehrer, *Diffusion is Solids: Fundamentals, Methods, Materials, Diffusion-Controlled Processes (Springer Series in Solid State Science 155)* (Springer, New York, 2007).

[9] H. Fujiwara, *Spectroscopic Ellipsometry, Principles and Applications* (John Wiley & Sons, West Sussex, 2009).

[10] R.H. Lyddane, R.G. Sachs, E. Teller, Phys. Rev. **59**, 673 (1941).

[11] R.P. Lowndes, Phys. Rev. B **1**, 2754 (1970).

[12] P. Granger, V.I. Parvulescu, S. Kaliaguine, and W. Prellier, *Perovskites and related mixed oxides: Concepts and Applications* (Wiley, Chichester, 2016).

[13] C.J. Fennie and K.M. Rabe, Phys. Rev. Lett. **97**, 267602 (2006).

[14] B.J. Gibbons and S. Trolier-McKinstry, IEEE Trans. Appl. Supercond. **7**, 2177 (1997).

[15] A. Kumar, N.J. Podraza, S. Deney, J. Li, L.W. Martin, Y.-H. Chu, R. Ramesh, R.W. Collins, and V. Gopalan, Appl. Phys. Lett. **92**, 231915 (2008).

[16] S. Kambda, V. Goian, M. Orlita, D. Nuzhnyy, J.H. Lee, D.G. Schlom, K.H. Rushchanskii, M. Ležaic, T. Birol, C.J. Fennie, P. Gemeiner, B. Dkhil, V. Bovtun, M. Kempa, J. Hlinka, and J. Petzelt, Phys. Rev. B **85**, 094435 (2012).

[17] A. O'Hara, T.N. Nunley, A.B. Posadas, S. Zollner, and A.A. Demkov, J. Appl. Phys. **116**, 213705 (2014).

[18] T. Kocourek, S. Inkinen, O. Pacherova, E. Chernova, Z. Potucek, L.D. Yao, M. Jelinek, A. Dejneka, S. van Dijken, and M. Tyunina, Appl. Phys. Lett. **107**, 172906 (2015).

[19] C.M. Nelson, M. Spies, L.S. Abdallah, S. Zollner, Y. Xu, and H. Luo, J. Vac. Sci. Technol. A **30**, 061404 (2012).

[20] B.C. Chakoumakos, D.G. Schlom, M. Urbanik, and J. Luine, J. Appl. Phys. **83**, 1979 (1998).

[21] H. Li, L. Salamanca-Riba, R. Ramesh, and J.H. Scott, J. Mater. Res. **18**, 1698 (2003).

[22] M.M.C. Chou, C. Chen, S.Y. Yang, C.H. Huang, and H.L. Huang, J. Phys. Chem. Solids **69**, 425 (2008).

[23] T. Runka, K. Lapsa, A. Lapinski, R. Aleksiyko, M. Berkowski, and M. Drozdowski, J. Mol. Struct. **704**, 281 (2004).

[24] H.G. Tompkins and W.A. McGahan, *Spectroscopic Ellipsometry and Reflectometry: A Users Guide* (Wiley, New York, 1999).

[25] H.G. Tompkins and E.A. Irene, *Handbook of Ellipsometry* (Springer, Heidelberg, 2005).

[26] H.G. Tompkins and J.N. Hilfiker, *Spectroscopic Ellipsometry: Practical Application to Thin Film Characterization* (Momentum Press, New York, 2015).

[27] K. Shimamura, H. Tabata, H. Takeda, V.V. Kochurikhin, and T. Fukuda, J. Cryst. Growth **194**, 209 (1998).

[28] B.-Q. Hu, X.-M. Wang, T. Zhou, Z.-Y. Zhao, X. Wu, and X.-L. Chen, Chin. Phys. Lett. **18**, 278 (2001).

[29] D. Nuzhnyy, J. Petzelt, S. Kamba, T. Yamada, M. Tyunina, A.K. Tagantsev, J. Levoska, and N. Setter, J. Electroceram. **22**, 297 (2009).

[30] P. Marsik, K. Sen, J. Khmaladze, M. Yazdi-Rizi, B.P.P. Mallett, and C. Bernhard, Appl. Phys. Lett. **108**, 052901 (2016).

[31] T. Willett-Gies, E. DeLong, and S. Zollner, Thin Solid Films **571**, 620 (2014).

[32] T.I. Willett-Gies, C.M. Nelson, L.S. Abdallah, and S. Zollner, J. Vac. Sci. Technol. A **33**, 061202 (2015).

[33] C. Bernhard, J. Humlíček, and B. Keimer, Thin Solid Films **455−456**, 143 (2004).

[34] A. Ghosh, C.M. Nelson, L.S. Abdallah, and S. Zollner, J. Vac. Sci. Technol. A **33**, 061203 (2015).

[35] S. Zollner, J.G. Chen, E. Duda, T. Wetteroth, S.R. Wilson, and J.N. Hilfiker, J. Appl. Phys. **85**, 8533 (1999).

[36] R. Tao, A.R. Guo, C.-S. Tu, I. Siny, R.S. Katiyar, R. Guo, and A.S. Bhalla, Ferroelectr. Lett. **21**, 79 (1996).

[37] R.L. Andrews, M.S. thesis, The Ohio State University, 2012.

[38] M.I. Alonso and K. Winer, Phys. Rev. B **39** 10056 (1989).

[39] S.C. Tidrow, A. Tauber, W.D. Wilber, R.T. Lareau, C.D. Brandle, G.W. Berkstresser, A.J. Ven Graitis, D.M. Potrepka, J.I. Budnick, and J.Z. Wu, IEEE Trans. Appl. Supercond. **7**, 1766 (1997).

[40] D.J. Tao, H.X. Wu, X.D. Xu, R.S. Yan, F.Y. Liu, A.P.B. Sinha, X.P. Jiang, and H.L. Hu, Opt. Mater. **23**, 425 (2003).

[41] J.L. Servoin, Y. Luspin, and F. Gervais, Phys. Rev. B **22**, 5501 (1980).

[42] M.V. Abrashev, A.P. Litvinchuk, M.N. Iliev, R.L. Meng, V.N. Popov, V.G. Ivanov, R.A. Chakalov, and C. Thomsen, Phys. Rev. B **59**, 4146 (1999).

[43] P. Delugas, V. Fiorentini, and A. Filipetti, Phys. Rev. B **71**, 134302 (2005).

[44] K.D. Fredrickson, C. Lin, S. Zollner, and A.A. Demkov, Phys. Rev. B **93**, 134301 (2016).

[45] A. Diebold, *Handbook of Silicon Semiconductor Metrology* (Marcel Dekker, New York, 2001).

[46] T. Yoshizawa, *Handbook of Optical Metrology: Principles and Applications* (CRC Press, Boca Raton, FL, 2009).

[47] S. Zollner, in *Ellipsometry at the Nanoscale*, edited by M. Losurdo and K. Hingerl (Springer, Berlin, 2013), pp. 607-627.

[48] C.M. Herzinger, B. Johs, W.A. McGahan, J.A. Woollam, and W. Paulson, J. Appl. Phys. **83**, 3323 (1998).

[49] R.F. Potter in *Handbook of Optical Constants of Solids*, edited by E.D. Palik (Academic Press, San Diego, 1998), pp. 462-475.

[50] S. Adachi, *The Handbook on Optical Constants of Semiconductors* (World Scientific, Singapore, 2012).

[51] M.L. Cohen and J.R. Chelikowsky, *Electronic Structure and Optical Properties of Semiconductors* (Springer, Berlin, 1988).

[52] P.Y. Yu and M. Cardona, *Fundamentals of Semiconductors: Physics and Materials Properties*, 4th ed. (Springer, Berlin, 2010).

[53] D.G. Seiler, S. Zollner, A.C. Diebold, and P.M. Amirtharaj, in *Handbook of Optics*, 3rd ed., edited by M. Bass (McGraw-Hill, New York, 2010), Vol. IV, Chap. 5, pp. 5.1-96.

[54] W.G. Spitzer, Semiconductors and Semimetals **3**, 17 (1967).

[55] R.J. Collins and H.Y. Fan, Phys. Rev. **93**, 674 (1954).

[56] W.C. Dash and R. Newman, Phys. Rev. **99**, 1151 (1955).

[57] G.G. Macfarlane, T.P. McLean, J.E. Quarrington, and V. Roberts, Phys. Rev. **108**, 1377 (1957); J. Phys. Chem. Solids **8**, 388 (1959).

[58] H.W. Icenogle, B.C. Platt, and W.L. Wolfe, Appl. Opt. **15**, 2348 (1976).

[59] M. Cardona and G. Harbeke, J. Appl. Phys. **34**, 813 (1963).

[60] H.R. Philipp and E.A. Taft, Phys. Rev. **113**, 1002 (1959).

[61] D.E. Aspnes and A.A. Studna, Phys. Rev. B **27**, 985 (1983).

[62] L. Viña, S. Logothetidis, and M. Cardona, Phys. Rev. B **30**, 1979 (1984).

[63] G.E. Jellison, Opt. Mater. **1**, 151 (1992).

[64] M.K. Kelly, S. Zollner, and M. Cardona, Surf. Sci. **285**, 282 (1993).

[65] D.E. Aspnes and A.A. Studna, Surf. Sci. **96**, 294 (1980).

[66] K.A. Bell, L. Mantese, U. Rossow, and D.E. Aspnes, Thin Solid Films **313-314**, 161 (1998).

[67] G.E. Jellison and B.C. Sales, Appl. Opt. **30**, 4310 (1991).

[68] B.E. Deal and A.S. Grove, J. Appl. Phys. **36**, 3770 (1965).

[69] G. Hellings, J. Mitard, G. Eneman, B. De Jaeger, D.P. Brunco, D. Shamiryan, T. Vandeweyer, M. Meuris, M.M. Heyns, and K. De Meyer, IEEE Electron Dev. Lett. **30**, 88 (2009).

[70] Y.Z. Hu, J.-Th. Zettler, S. Chongsawangvirod, Y.Q. Wang, and E.A. Irene, Appl. Phys. Lett. **61**, 1098 (1992).

[71] P. Ponath, A.B. Posadas, R.C. Hatch, and A.A. Demkov, J. Vac. Sci. Technol. B **31**, 031201 (2013).

[72] S.R.M. da Silva, G.K. Rolim, G.V. Soares, I.J.R. Baumvol, C. Krug, L. Miotti, F.L. Freire, M.E.H.M. da Costa, and C. Radtke, Appl. Phys. Lett. **100**, 191907 (2012).

[73] K. Kita, S. Suzuki, H. Nomura, T. Takahashi, T. Nishimura, and A. Toriumi, Jpn. J. Appl. Phys. **47**, 2349 (2008).

[74] H. Matsubara, T. Sasada, M. Takenaka, and S. Takagi, Appl. Phys. Lett. **93**, 032104 (2008).

[75] P. Bohač, L. Jastrabik, D. Chvostova, and V. Železny, Vacuum **41**, 1466 (1990).

[76] J.A. Woollam Co., Inc., Lincoln, NE.

[77] G.E. Jellison and F.A. Modine, Appl. Phys. Lett. **69**, 371 (1996); **69**, 2137 (1996).

[78] J. Leng, J. Opsal, H. Chu, M. Senko, and D.E. Aspnes, J. Vac. Sci. Technol. A **16**, 1654 (1998).

[79] A. Kahan, J.W. Goodrum, R.S. Singh, and S.S. Mitra, J. Appl. Phys. **42**, 4444 (1971).

[80] E.R. Lippincott, A. Van Valkenburg, C.E. Weir, and E.N. Bunting, J. Res. Natl. Bur. Stand. **61**, 61 (1958).

[81] M. Hass, J. Phys. Chem. Solids **31** 415 (1970).

[82] M. Erman, J.B. Theeten, N. Vodjdani, and Y. Demay, J. Vac. Sci. Technol. B **1**, 328 (1983).

[83] D.E. Aspnes, in *Handbook on Semiconductors: Optical Properties of Solids*, edited by M. Balkanski (North-Holland, Amsterdam, 1980), vol. 2, p. 109.

[84] C.C. Kim, J.W. Garland, H. Abad, and P.M. Raccah, Phys. Rev. B **45**, 11749 (1992).

[85] C.M. Herzinger and B.D. Johs, U.S. Patent No. 5,796,983 (18 August 1998).

[86] G.G. Devyatykh, E.M. Dianov, N.S. Karpychev, S.M. Mazavin, V.M. Mashinskiĭ, V.B. Neustruev, A.V. Nokolaĭchik, A.M. Prokhorov, A.I. Ritus, N.I. Sokolov, and A.S. Yushin, Sov. J. Quantum Electron. **10**, 900 (1980).

[87] L. Pajasova, Czech. J. Phys. B **19**, 1265 (1969).

[88] G.E. Jellison and J.W. McCamy, Appl. Phys. Lett. **61**, 512 (1992).

[89] T.P. McLean and E.G.S. Paige, in *Report of the International Conference on the Physics of Semiconductors*, edited by A.C. Stickland (Institute of Physics, London, 1962), p. 450.

[90] See supplementary material at [URL will be inserted by AIP Publishing] for a listing of the oscillator parameters for Ge and GeO_2 and for tables of the optical constants of these materials.

[91] J.M. Jackson, M.E. Wells, G. Kordas, D.L. Kinser, R.A. Weeks, and R.H. Magruder, J. Appl. Phys. **58**, 2308 (1985).

[92] A.A. Demkov and O.F. Sankey, Phys. Rev. Lett. **83**, 2038 (1999).

[93] W.A. Pliskin, J. Vac. Sci. Technol. **14**, 1064 (1977).

[94] K. Taniguchi, M. Tanaka, C. Hamaguchi, and K. Imai, J. Appl. Phys. **67**, 2195 (1990).

[95] N. Kitamura, K. Fukumi, J. Nishii, and N. Ohno, J. Appl. Phys. **101**, 123533 (2007).

[96] W. Rzodkiewicz and A. Panas, Acta Physica Polonica A **116**, S-92 (2009).

[97] T.I. Willett-Gies, C.M. Nelson, L.S. Abdallah, and S. Zollner, J. Vac. Sci. Technol. A **33**, 061202 (2015).

[98] L.S. Ornstein and J.H. van der Veen, Physica **3**, 289 (1936).

[99] L.S. Ornstein and O. Koefoed, Physica **5**, 175 (1938).

[100] A.V. Sokolov, *Optical Properties of Metals* (Blackie and Son, London, 1967).

[101] L.S. Abdallah, S. Zollner, C. Lavoie, A. Ozcan, and M. Raymond, Thin Solid Films **571**, 484 (2014).

[102] G. Metzger, P. Pluvinage, and R. Torguet, Ann. Phys. (Paris) **10**, 5 (1965).

[103] G. Neuber, R. Rauer, J. Kunze, T. Korn, C. Pels, G. Meier, U. Merkt, J. Bäckström, and M. Rübhausen, Appl. Phys. Lett. **83**, 4509 (2003).

[104] L.S. Abdallah, T.M. Tawalbeh, I.V. Vasiliev, S. Zollner, C. Lavoie, S. Ozcan, and M. Raymond, AIP Adv. **4**, 017102 (2014).

[105] P.N. Argyres, Phys. Rev. **97**, 334 (1955).

[106] P.B. Johnson and R.W. Christy, Phys. Rev. B **9**, 5056 (1974).

[107] D.W. Lynch and W.R. Hunter, in *Handbook of Optical Constants of Solids*, edited by E.D. Palik (Academic, San Diego, 1998), p. 275.

[108] K.W. Wierman, J.N. Hilfiker, R.F. Sabiryanov, S.S. Jaswal, R.D. Kirby, and J.A. Woollam, Phys. Rev. B **55**, 3093 (1997).

[109] C. Wolff, R. Rodríguez-Oliveros, and Kurt Busch, Optics Express **21**, 12022 (2013).

[110] K. Mok, C. Scarlat, G.J. Kovács, L. Li, V. Zviagin, J. McCord, M. Helm, and H. Schmidt, J. Appl. Phys. **110**, 123110 (2011).

[111] H. Bittel and W. Gerlach, Ann. Physik **33**, 661 (1938).

[112] H.H. Potter, Proc. Phys.. Soc. **49**, 671 (1937).

[113] R.J. Weiss and A.S. Marotta, J. Phys. Chem. Solids **9**, 302 (1959).

[114] F.C. Zumsteg and R.D. Parks, Phys. Rev. Lett. **24**, 520 (1970).

[115] N.F. Mott, Proc. Roy. Soc. (London) **153**, 699 (1936).

[116] T. Kasyua, Prog. Theor. Phys. **16**, 58 (1956).

[117] P.G. de Gennes and J. Friedel, J. Phys. Chem. Solids **4**, 71 (1958).

[118] B.R. Coles, Adv. Phys. **7**, 40 (1958).